University of Alberta

Library Release Form

Name of Author: Raluca A. Eftimie

Title of Thesis: Modeling group formation and activity patterns in self-organizing communities of organisms

Degree: Doctor of Philosophy

Year this Degree Granted: 2008

Raluca A. Eftimie
Department of Mathematical and Statistical Sciences
Central Academic Building 632, University of Alberta
Edmonton, Alberta, T6G 2G1
Canada

Date: _____

University of Alberta

Modeling group formation and activity patterns in self-organizing communities of organisms

by

Raluca A. Eftimie

A thesis submitted to the Faculty of Graduate Studies and Research in partial fulfillment of the requirements for the degree of **Doctor of Philosophy**.

in

Applied mathematics

Department of Mathematical and Statistical Sciences

Edmonton, Alberta
Fall 2008

University of Alberta

Faculty of Graduate Studies and Research

The undersigned certify that they have read, and recommend to the Faculty of Graduate Studies and Research for acceptance, a thesis entitled **Modeling group formation and activity patterns in self-organizing communities of organisms** submitted by Raluca A. Eftimie in partial fulfillment of the requirements for the degree of **Doctor of Philosophy** in *Applied mathematics*.

Professor Mark A. Lewis (Supervisor)
Professor Gerda de Vries (Supervisor)

Examiner 1

Examiner 2

Examiner 3 (External)

Date: _____

To my parents' memory.

Abstract

In this thesis, we propose a general framework to model animal group formation and movement based on how individuals receive information from neighbors, and the amount of information received. In particular, we construct and analyze a new one-dimensional nonlocal hyperbolic model for group formation, with application to self-organizing collectives of animals in homogeneous environments. The model investigates the effects of nonlocal social interactions (that is, attraction towards neighbors that are far away, repulsion from those that are near by, and alignment with neighbors at intermediate distances) on the emergence of group patterns. These nonlocal interactions can influence individuals' speed and turning behavior.

We demonstrate that this one-dimensional model can generate a wide range of spatial and spatiotemporal patterns. In particular, depending on the assumptions regarding how individuals receive information, the model displays at least 21 different patterns. Some of these patterns are classical, such as stationary pulses, traveling pulses, or traveling trains. However, the majority of these patterns are novel, such as the patterns we call zigzag pulses and feathers. To investigate these patterns, we use numerical and analytical techniques such as bifurcation theory, linear and nonlinear analysis.

This modeling framework presents a unitary approach for animal group formation and movement. *All the patterns* obtained with other parabolic and hyperbolic models existent in the literature can also be obtained with the model we propose in this thesis. In addition to this, we obtain a variety of new and interesting patterns.

Acknowledgements

I would like to thank Professors Mark A. Lewis and Gerda de Vries, my supervisors, for their many suggestions and constant support during this research. For me, they were the perfect supervisors by allowing me to pursue any research ideas I would have, and providing guidance when I needed. I am also thankful to Professor Frithjof Lutscher for his guidance through the early stages of this thesis.

The F.S. Chia Scholarship (2002-2006), Queen Elisabeth II Scholarship (2007–2008), and Josephine Mitschell Research Scholarships (2005 and 2007) were crucial to the successful completion of this project. I am also very thankful for the traveling grants offered by University of Alberta (J. Gordin Kaplan Graduate Student Award, and Graduate Student Association Professional Development Grant), Society for Mathematical Biology (SMB Travel Grant, 2007), and Society for Industrial and Applied Mathematics (SIAM Travel Grant, 2007).

I am very grateful to my sister, for her continuous support and love. Without her, this work would have never come into existence.

Finally, I am thankful to the entire Lewis' lab (and in particular to Alex Potapov, Jung Min Lee, and Frank Hilker) for fruitful discussions and suggestions regarding my research.

Table of Contents

List of Tables

List of Figures

Chapter 1

Introduction

1.1 Problem description

Pattern formation is one of the most studied aspects of animal communities (see for example [1, 4, 24, 35, 58, 71, 79, 89, 94, 96, 108, 121, 126] and the references therein). Some of the most remarkable examples of patterns observed in animal groups are related to the behavior displayed by these groups [94]. Stationary aggregations formed by resting animals, migrating herds of ungulates, zigzagging flocks of birds, and milling schools of fish are only a few of the patterns.

There are two types of factors that influence group formation: (a) external factors that, for example, give rise to chemotaxis, phototaxis or thermotaxis [54], and (b) internal factors, which are social interactions that act among individuals [7, 13, 58, 114, 133]. These second factors lead to self-organized animal aggregations. In this research, we will focus only on this type of aggregations since it represents the main interest of complexity theory [94].

There are different possible reasons for which animals self-organize into aggregations. For example, being in a group might increase chances of survival [45, 130]. Also, it increases the possibility of finding a mate, as well as the foraging efficiency [94, 102]. However, there are still some fundamental issues regarding these aggregations that have to be addressed. For example, it is still unknown what factors decide the shape of an aggregation, and how is this shape maintained over a certain period of time [21]. Also, what triggers the transitions between different patterns? Another important aspect that has to

be considered when trying to understand these aggregations is animal communication. Empirical results suggest that there might be a relation between how individuals receive information from conspecifics, the quantity of information, and the social interactions between group members [34]. However, this aspect has not been investigated yet. It should be mentioned that understanding these aggregations has not only theoretical significance, but also more practical applications. For example, understanding schooling behavior can be useful in establishing fishing strategies [93, 105], while understanding desert locust aggregations can be useful in managing and controlling this species' outbreaks [114, 125].

The main question that scientists are trying to answer in regard to these animal aggregations is how do we integrate what we know at individual level to understand the group level behaviors [94, 96, 120, 132]. Mathematical models can shed a light on this aspect, by identifying which individual-level mechanisms lead to the spatial and spatiotemporal group patterns observed in animal communities. These models fall into two frameworks: Lagrangian models (individual-based models), and Eulerian models (continuum models). A summary of some of these models is shown in Tables 1.1 and 1.2. In the following two sections, we will give an overview of some of the Lagrangian and Eulerian models that had a great impact on the direction of the research in this area. In Section 1.2, we will review some of the Lagrangian models that have been most successful at obtaining patterns similar to those observed in nature. In Section 1.3, we will focus on the Eulerian models and discuss the parabolic versus hyperbolic modeling approaches, and the resulting spatial and spatiotemporal patterns. In Section 1.4, we will discuss an important aspect of animal ecology that is only indirectly considered by both Lagrangian and Eulerian models, namely animal communication, and its relation to group behavior. In Section 1.5, we give an outline of this thesis.

Author	**Lagrangian models**			**Dimension**
	attr., rep.	align.	attr., rep., align.	
[1]Adioui, et. al.,2003		$\sqrt{(L)}$		2D
[5]Aoki,1982			$\sqrt{}$	2D
[7]Beecham,Farnsworth,1999	$\sqrt{}$			2D
[11]Borner et. al.,2006		$\sqrt{}$		1D
[17]Buhl et. al.,2006		$\sqrt{}$		1D
[24]Couzin,2002			$\sqrt{}$	3D
[37]Gazi,Passino,2002	$\sqrt{}$			3D;nD,$n \geq 1$
[42]Gueron et. al.,1996	$\sqrt{}$			2D
[46]Helbing,Molnar,1995	$\sqrt{}$			2D
[50]Hemelrijk,Kunz,2004			$\sqrt{}$	2D
[49]Hemelrijk,Hildenbrandt,2008			$\sqrt{}$	3D
[51]Hensor et. al.,2008			$\sqrt{}$	2D
[58]Huth,Wissel,1994			$\sqrt{}$	2D
[61]Inada,2001			$\sqrt{}$	2D
[64]Kunz,Hemelrijk,2003			$\sqrt{}$	2D
[81]Mogilner et. al.,2003	$\sqrt{}$			1D;2D
[89]Niwa,1994	$\sqrt{}$			3D
[107]Reuter,Breckling,1994			$\sqrt{}$	2D
[108]Reynolds,1987			$\sqrt{}$	3D
[128]Vicsek et. al.,1995		$\sqrt{}$		2D
[132]Viscido et. al.,2005	$\sqrt{}$			2D

Table 1.1: A summary of some of the Lagrangian mathematical models existent in the literature.

Author	**Eulerian models**			**Dimension**	
	rep.	attr., rep.	align.	attr., rep., align.	dependent
[1]Adioui, et. al.,2003		$\surd(L)$			2D
[15]Bressloff,2004				$\surd(N)$	2D
[20]Burger et. al.,2007		$\surd(N)$			nD, $n \geq 1$
[30]Eftimie et. al.,2007				$\surd(N)$	1D
[29]Eftimie et. al.,2007				$\surd(N)$	1D
[35]Flierl et. al.,1999		$\surd(L)$			2D
[41]Grunbaum, Okubo,1994		$\surd(L)$			1D,2D
[39]Grunbaum,1994	$\surd(L)$		$\surd(L)$		2D
[40]Grunbaum,1998			$\surd(L)$		2D
[59]Igoshin et. al.,2001			$\surd(L)$		1D,2D
[60]Igoshin et. al.,2004			$\surd(L)$		2D
[28]Edelstein-Keshet, et. al.,1998		$\surd(L)$			1D
[69]Lutscher,2002			$\surd(L)$		1D
[70]Lutscher,2003			$\surd(L)$		1D
[71]Lutscher,Stevens,2002			$\surd(L)$		1D
[76]Mogilner, Edelstein-Keshet,1995				$\surd(N)$	2D
[77]Mogilner, Edelstein-Keshet,1996				$\surd(N)$	1D
[80]Mogilner, Edelstein-Keshet,1999		$\surd(N)$			1D
[83]Morale et. al.,2004		$\surd(N)$			nD,$n \geq 1$
[101]Pfistner,Alt,1990			$\surd(N)$		2D
[99]Pfistner,1990			$\surd(N)$		1D
[100]Pfistner,1995			$\surd(N)$		1D
[122]Topaz, Bertozzi,2004		$\surd(N)$			2D
[123]Topaz et. al.,2006	$\surd(N)$				1D,2D

Table 1.2: A summary of the Eulerian mathematical models existent in the literature. L represents *local model*, while N represents *nonlocal model*.

1.2 Lagrangian models for group formation and movement

In the Lagrangian approach, a set of decision rules that govern the movements of individuals is given (see for example [5, 24, 42, 50, 58, 81, 95, 107, 108, 126] and the references therein). Most of these models are in two or three spatial dimensions, and include three types of social interactions that can alter the position of an individual: attraction towards individuals that are far away, repulsion from those that are in close vicinity, and a tendency to align with those neighbors that are at intermediate distances [5, 24, 50, 58, 107, 108]. In two spatial dimension, the ranges over which the interactions have effect are concentric (as in [50, 58, 95]), while in three dimensions they are spherical [24]. Note that the social interactions are introduced in an additive manner (see the reviews in [41] and [95]). We should stress here that the majority of the Lagrangian models assume that individuals' behavior is influenced by all three social interactions (see for example [5, 24, 49, 50, 58, 107]). These interactions can affect the direction of movement of an individual, as well as its speed. However, most of the Lagrangian models existent in the literature concentrate only on the direction changes, and assume that the speed is constant or random (as in [24, 50, 58, 126, 129, 133] and the review in [96]).

To understand the effect of the social interactions, the models investigate the structure of the groups (e.g., geometry of the group, degree of polarization, etc.) through numerical simulations. In this context, Aoki [5] and Niwa [89] showed that the group structure and movement depend on the attractive and alignment interactions. In particular, both the attraction and alignment are necessary for polarized groups to form and maintain their cohesion.

In general, the simulations with constant (or random) speed and density-dependent directional changes show very close agreement between the group structures obtained numerically and those observed in nature [24, 58, 108, 126]. Couzin et. al.[24], for example, described four types of groups: swarm, torus, dynamic parallel groups and highly parallel groups. This particular paper changed the direction of the research in the Lagrangian approach, by

investigating the transition between these types of group structures as the size of the interaction zones is varied. Moreover, this model shows that depending on the values of the parameters, there is a hysteresis phenomenon between different group structures.

A very few models assume that also the speed is influenced by the interactions with neighbors [17, 42, 49, 108]. For example, Gueron et. al. [42] considered that individuals have an intrinsic speed which is complemented by a second component determined by the social interactions with neighbors. Thus, individuals accelerate or decelerate in response to neighbors that are within the repulsion or attraction ranges. The results show that this variable speed can account for the splitting and merging behavior observed in different animal groups (e.g., herds and fish schools). Moreover, group splitting can also occur if the size of the attraction range is too small.

Buhl et. al [17] derived a one-dimensional model which assumes that individuals turn to align with their neighbors, and adapt their velocity to the average velocity of these neighbors. The model shows a phase transition between disordered movement and highly aligned collective movement. This transition, which is caused by an increase in the total group density, was also confirmed empirically through experiments using locust nymphs.

Similar phase transitions are obtained with traffic models [112], and models for pedestrian-movement [46], where cars/pedestrians accelerate and decelerate due to interactions with other cars/pedestrians. The models exhibits phase transitions between free flow and traffic jams, and again, these phase transitions are determined by the density of vehicles/pedestrians.

Due to analytical difficulties in studying Lagrangian models, as well as some computational limitations, this approach is applied mostly to small groups of organisms. The formation and movement of large, dense groups of organisms is described by Eulerian models. We will discuss some of these models in the next section. Before this, we should mention that there are models that try to bridge the gap between Lagrangian and Eulerian approach (see for example [35, 39, 92, 83]). These models start with a Lagrangian formulation of the interactions between individuals, and in the limit, under reasonable approximations, an

Eulerian model is obtained. Note that the resulting continuum models are usually described by parabolic equations [1, 10, 20, 35, 39, 83, 92]

1.3 Eulerian models for group formation and movement

Eulerian models are used to study the dynamics of the density of individuals, which is typically described by partial differential equations. Usually, these models are applied to large populations of insects, fish, bacteria, and so forth. Eulerian models for animal aggregations can be divided into two categories: parabolic and hyperbolic equations. These models also incorporate social interactions, namely attraction towards neighbors, repulsion from them, and alignment with others. However, compared to the Lagrangian models which usually incorporate all three interactions, the Eulerian models generally focus on attractive and repulsive interactions alone [77, 80, 123], or on alignment interactions alone [71, 99]. There are very few models that incorporate all three social interactions [15, 60, 79], and these models are usually two dimensional.For both parabolic and hyperbolic models, the social interactions between group members can be local, when immediate neighbors or local effects of the environment are important [27, 69, 71], or nonlocal, when distant individuals or nonlocal effects of the environment play an important role [15, 77, 80, 122, 123].

In the following, we will overview some of these models and the spatial and spatiotemporal patterns that they generate.

1.3.1 Parabolic models

The great majority of the Eulerian models for animal group formation and movement are described by parabolic equations (advection-diffusion equations, or advection-diffusion-reaction equation) [3, 15, 35, 59, 60, 75, 76, 77, 78, 80, 82, 91, 122, 123]. These models can be derived using a correlated random walk approach [67, 124], or using Fick's law [41, 59]. They usually take the form

$$f_t = \nabla(D\nabla f) - \nabla(Vf) + G(f), \tag{1.1}$$

where $f(x,t)$ is the population density, D is the diffusion coefficient, and V is the advection coefficient. Some models also include a reaction term $G(f)$, which describes the contributions of population dynamics to the changes in density [75]. In the following, we will assume that organisms' growth happens on a much larger time scale compared to the formation of groups and their movement, and therefore we will ignore the reaction term.

One of the most intriguing questions that scientists have tried to answer in regard to some moving animal groups (such as swarms of locusts), is the long-time existence of these groups. Note that these groups also have well defined boundaries, with the population density dropping to zero at the edges. Mathematically, this can be described by traveling pulses. To solve this traveling pulse problem, researchers focused first on local mathematical models that incorporated biologically realistic assumptions [28]. When these models failed to exhibit traveling pulses, scientists directed their attention to nonlocal models [80, 122, 123]. In one dimension, these models are described by the following equations

$$f_t = \left(Df_x - V(f)f\right)_x, \tag{1.2}$$

where f denotes the swarm density, D is the diffusion coefficient, and $V(f)$ is the nonlocal, density-dependent velocity. The earliest integral formulations of the density flux define

$$V(f) = K * f = \int_D K(x-x')f(x',t)dx', \tag{1.3}$$

where K is an antisymmetric convolution kernel [41]. Mogilner and Edelstein-Keshet [80] extended this model to include also a local and a nonlocal group drift. Also, the convolution kernel is considered to have two components: an attractive and a repulsive component. The velocity is therefore described by the following equation

$$V(f) = a_e f + A_a(K_a * f) - A_r f(K_r * f), \tag{1.4}$$

with the odd kernels

$$K_r(x) = -\frac{x}{2r^3}e^{-x^2/2r^2}, \quad K_a(x) = -\frac{x}{2a^3}e^{-x^2/2a^2}. \tag{1.5}$$

Here a and r are the spatial ranges for the attractive and repulsive interactions, A_r and A_a are the coefficients of these interactions, while K_r and K_a are the kernels modeling the interactions. The term a_e gives the effect of local interactions on the velocity. Both analytical and numerical results have shown that when diffusion is density-independent, it is not possible to obtain a true traveling pulse solution, even if the groups can persist for a long time. The authors then introduced an even, nonlocal drift term:

$$V(f) = a_e f + (A_a - A_r f)(K_0 * f) + A_e(K_e * f), \tag{1.6}$$

where K_0 is an odd nonlocal kernel, while K_e is an even nonlocal drift kernel. The numerical results show that in this case very few individuals get lost, and thus the swarm is preserving quite well its initial shape. It should be mentioned here that their results with different types of kernels suggest that the symmetry of the kernel, rather than the particular form of the kernel, is important for the final pattern.

Mogilner and Edelstein-Keshet [80] also studied analytically the effect of density-dependent diffusion. In this case, the results show that it is possible to obtain a true traveling pulse solution.

Considering these models as a starting point, different authors have investigated other types of spatial and spatiotemporal patterns that arise in nonlocal models with attractive and repulsive fluxes. For example, Topaz and Bertozzi [122] derived a two-dimensional model that shows vortices and stationary clumps, depending on the type of interaction kernels used (i.e., kernels for rotational motion, and kernels for motion towards and away from concentration density). Topaz et. al. [123] derived a one-dimensional model that incorporates density-dependent diffusion, and only nonlocal attraction (i.e., the repulsion is considered to arise as an anti-crowding mechanism). The model shows stationary pulses that have well defined boundaries. Moreover, the authors extended the model to higher dimensions, and the results were similar.

A different type of social aggregation that captivated scientists is observed in Myxobacteria colonies. Under starvation conditions, these organisms ag-

gregate and form stationary aggregations called "fruiting bodies". However, during the initial phase of aggregation, they display what is called a rippling behavior: right-moving and left-moving waves that appear to pass through each other. In an attempt to understand this behavior, researchers focused on local mathematical models that can describe the interaction between cells moving in opposite directions, and that meet head-on [59, 60]. Note that the interaction depends only on the contact between cells, with no signals that diffuse. The resulting parabolic equations show remarkable agreement with the experiments: waves that pass through each other, giving rise to the rippling behavior. Note that the models proposed in [59, 60] are described in terms of diffusion, convection, and also an alignment component due to reversals caused by interactions with cells moving in opposite direction.

There are a very few other parabolic models that also incorporate alignment, two such examples being proposed by [77] and [15]. Both models are two dimensional and show three types of spatial patterns: alignment without aggregation, aggregation without alignment, and patches of aligned objects.

1.3.2 Hyperbolic models

Since the parabolic models show the unrealistic effect of infinite propagation speed, a few authors focused on hyperbolic models to study animal movement (e.g.,[44, 69, 70, 71, 99, 100, 101]). In all these cases, the basic equations are derived using the classical Goldstein-Kac theory for correlated random walks (see [38, 62]). To exemplify this theory, let us divide the domain into intervals of length Δx, and consider the time step Δt. Define $p^+(x,t)$ ($p^-(x,t)$) to be the probability that a right-moving (left-moving) individual is at (x,t), and λ^+ (λ^-) be the probability of turning if the individual is moving right (left). Then, the probability that a right-moving individual is positioned at x at the next time step $t+\Delta t$ is given by

$$p^+(x,t+\Delta t) = p^+(x-\Delta x,t)(1-\lambda^+\Delta t) + p^-(x+\Delta x,t)\lambda^-\Delta t. \qquad (1.7)$$

Similarly, the probability that a left-moving individual is positioned at x at the next time step $t + \Delta t$ is given by

$$p^-(x, t + \Delta t) = p^-(x + \Delta x, t)(1 - \lambda^- \Delta t) + p^+(x - \Delta x, t)\lambda^+ \Delta t. \qquad (1.8)$$

Expanding these two equations in Taylor series about (x, t) leads to

$$\begin{aligned} p_t^+(x,t) + \frac{\Delta x}{\Delta t} p_x^+(x,t) &= -\lambda^+ p^+(x,t) + \lambda^- p^-(x,t) + \Delta x \lambda^+ p_x^+ + \Delta x \lambda^- p_x^-, \\ p_t^-(x,t) - \frac{\Delta x}{\Delta t} p_x^-(x,t) &= \lambda^+ p^+(x,t) - \lambda^- p^-(x,t) - \Delta x \lambda^+ p_x^+ - \Delta x \lambda^- p_x^- \end{aligned} \qquad (1.9)$$

For $\Delta x \to 0$, $\Delta t \to 0$, such that $\frac{\Delta x}{\Delta t} \to \gamma$, we obtain

$$\begin{aligned} p_t^+(x,t) + (\gamma p^+(x,t))_x &= -\lambda^+ p^+(x,t) + \lambda^- p^-(x,t), \\ p_t^-(x,t) - (\gamma p^-(x,t))_x &= \lambda^+ p^+(x,t) - \lambda^- p^-(x,t). \end{aligned} \qquad (1.10)$$

Note that now $p^+(x, t)$ and $p^-(x, t)$ are interpreted as probability density functions for the right-moving and left-moving individuals [135]. These individuals move at a constant speed γ, and change direction randomly according to Poisson processes with rates $\lambda^\pm$ (i.e., the probability not to change direction within the time interval [0, t) decreases as $e^{-\lambda^\pm t}$).

Almost all the hyperbolic models for animal group formation assume that individuals turn in response to interactions with other neighbors, that is, the turning rates $\lambda^\pm$ are density-dependent. The majority of these models consider local interactions with neighbors [69, 70, 71]. Only a few hyperbolic models assume that the turning rates are influenced by distant neighbors [99, 100].

For example, Lutscher and Stevens [71] investigated the rippling behavior in Myxobacteria colonies using turning rates that have a random (μ) and a directed component ($\mu^\pm$): $\lambda^\pm = \mu + \mu^\pm(u^+, u^-)$. The authors discuss analytical and numerical results obtained with different types of turning functions $\mu^\pm$. When the turning rates are equal and depend only on the left-moving neighbors (i.e., $\mu^\pm(u^+, u^-) = f(u^-)$), the results show ripples and stationary aggregations.

Modeling the behavior of the same Myxobacteria swarms, Pfistner [99] started with equations (1.10) and assumed that cells turn only as a result of the

interactions with distant cells. More precisely, cells turn to align themselves with other neighbors within a perception interval $[-R, R]$. The turning rates are defined by the following nonlocal terms:

$$\begin{aligned} \lambda^+ &= \Lambda\left(\int_{-R}^{R}(\alpha(s)u^+(x+s,t)+\beta(s)u^-(x+s,t))ds\right) \\ \lambda^- &= \Lambda\left(\int_{-R}^{R}(\alpha(s)u^-(x-s,t)+\beta(s)u^+(x-s,t))ds\right), \end{aligned} \tag{1.11}$$

where α and β are weight functions for the surrounding densities, and the functional Λ is monotone increasing and positive. The results show stationary swarms. Later, Pfistner modified this model to incorporate moving boundaries for the swarm edges [100]. The dynamics of the swarm is thus analyzed numerically through the retraction and expansion of the boundaries. An extension of this model in two spatial dimensions can be found in [101].

The models we mentioned above assume that the speed is constant, while the turning rates are determined by the alignment interactions with local or nonlocal neighbors. However, it is known that some organisms also adapt their speed to their neighbors' speed [57]. Such a model, which assumes that individuals adapt both their speed and direction to that of their neighbors, was introduced in [70]. The equations for the movement of individuals are similar to (1.10), where $\lambda^+ = \lambda^- = \lambda(u^+, u^-)$, and the speeds for the right-moving and the left-moving individuals are described by γ^+ and γ^-, respectively. These speeds are assumed to depend not only on the local density of individuals, but also on the gradient of this density. In particular, the speeds satisfy the following elliptic equations

$$\begin{aligned} \beta\gamma^+_{xx} &= \gamma^+ - E(u^+, u^+_x), \\ \beta\gamma^-_{xx} &= \gamma^- - E(u^-, -u^-_x). \end{aligned} \tag{1.12}$$

Numerical simulations were performed only for right-moving individuals, with the speed satisfying a parabolic equation of the form $\tau\gamma^+_t = \beta\gamma^+_{xx} - \gamma + E(u^+, u^+_x)$. The results show traveling pulses.

To summarize the results of this section, the one-dimensional continuum models that investigate animal aggregations fail to account for the multitude

of complex patterns that one can observe in nature. Generally, the patterns exhibited by these models are simple: local parabolic models do not support traveling waves [27], but can give rise to ripples [60], while nonlocal parabolic models can give rise to stationary pulses [123], or to traveling pulses, provided that diffusion is density-dependent [80]. Hyperbolic models give rise to ripples [71], aggregations [71],[100], and traveling pulses [70]. Considering that one-dimensional models have not explained the complexity of the patterns observed in biological systems, scientists have directed their attention towards two-dimensional models. The results are more complex (e.g., ripples [60], stationary aggregations [123], vortex-like groups [122], patches of aligned individuals [15, 77]), but they still cannot account for the multitude of observed patterns.

One possible reason for this failure is that the assumptions considered by these models do not fully describe the social interactions between individuals governing group formation. More precisely, these models consider that the social interactions depend only on the distances between individuals. However, this assumption might not be sufficient since different species use different signals and communication mechanisms. It is very likely that these mechanisms influence the social interactions between individuals. We will discuss this aspect in more detail in the next section.

1.4 Animal communication

The movement decisions made by small or large groups are based on the local and global communication used by these animal groups [22]. In the literature, there is a lot of information regarding the communication mechanisms involved at individual level (e.g., [32, 33, 113]). For example, Endler and Basolo [33] discuss 9 different stages in the communication between a sender and a receiver :

(1) the generation and the emission of the signal;

(2) signal transmission which is influenced by environmental properties;

(3) signal reception which is determined by the structure of the sense organs;

(4) signal transduction;

(5) signal design and content;

(6) signal perception;

(7) classification of the perceived signals;

(8) extraction of critical information from the signal;

(9) the decision in response to the signal;

While there is much information regarding the individual-level communication, the group-level communication is less understood [22]. As mentioned in [23], understanding the behavior of an individual in isolation, does not necessarily mean that we understand the behavior of that individual within a group, because of the nonlinear interactions with neighbors. However, the only way to probe animal communication is to focus on the changes in the behavior of an individual upon the reception of signals from conspecifics [73]. In particular, the reception of a signal can cause movement towards or away from the signaler's position [73]. For this reason, in this thesis we will focus only on the signal perception (i.e., stage (6) in the classification by Endler and Basolo), and the movement decisions made in response to these signals (stage (9)).

Animal communication uses different signals, such as visual, acoustic, chemical or tactile signals, and combinations of these signals [32, 73, 97]. Both emission and reception of signals can be unidirectional or omnidirectional, depending on the signal. Moreover, the reception of signals is affected by environmental conditions and the receiver's physiological limitations, and therefore different species make use of different signals and reception mechanisms [31, 32]. However, since we focus not only on signal reception but also on the decisions made in response to these signals, which in turn, will generate signals received by other neighbors, we prefer to use the term "communication mechanisms" instead of "reception mechanisms". Moreover, throughout this thesis we assume that through communication, individuals gain knowledge about the number, position, and direction of movement of their neighbors.

In regard to these communication signals, we should also mention that different signals act on different ranges. For example, depending on the species, visual signals can be used for close-range communication, while chemical and

sound signals can be used for medium or long-range communication [73]. Moreover, same type of signals (such as sound signals, for example), can sometimes be used on short ranges to increase animal spacing, while other times they can be used on long ranges to decrease spacing and promote aggregation [111]. Therefore, there is a very close relation between animal behavior, and the signals and the communication mechanisms these animals use.

We should stress here that different species use different communication mechanisms. As an example, it is known that some species of birds use directional sound signals (which require the emitter to face the receiver) to coordinate the flock movements, and omnidirectional signals (with emitters moving in any direction) to attract mates or to repel intruders [134]. For Mormon crickets, the movement seems to be influenced by the signals received from conspecifics approaching from behind, and from those positioned ahead and moving away [115]. The movement direction of some fish is more frequently influenced by the movement direction of the neighbors positioned ahead of them than those at their side [127]. Therefore, one can expect to see different species displaying different behaviors and group patterns, corresponding to these different communication mechanisms. Unfortunately, the literature (either mathematical or biological) is lacking a framework to characterize the relationship between animal communication and the resulting group patterns. A few individual-based models (e.g., [24, 49, 58, 61]) take into account that individuals may not receive information from behind because of a so-called "blind spot". However, as we mentioned, there are many other ways individuals can receive information from conspecifics.

The purpose of this thesis is therefore to find a way to incorporate into a mathematical model how individuals receive information from conspecifics and the amount of information received. In particular, we use the directionality of the signals, as well as the ranges on which signals have effect, to define the social interactions. Then, we can use this model to investigate the resulting group patterns. Moreover, analytical analysis of the patterns can help us understand the effect of the communication mechanisms on the group-level patterns. We will discuss these aspects in more detail in the next section,

when we give an outline of the thesis.

1.5 Thesis outline

As shown in the previous sections, different mathematical models use different assumptions and in consequence, display different spatial and spatiotemporal patterns. In particular, the patterns obtained with Eulerian models are quite simple, the models failing to account for the multitude of patterns observed in nature. Some of the questions that arise in regard to these results are: Can we find a unitary framework to explain all these different patterns? Moreover, can animal communication provide such a framework? Can this framework be tailored to specific animal species that use different signal reception mechanisms? Can an Eulerian model display patterns similar to those obtained with Lagrangian models (such as the splitting-merging behavior observed in some animal groups)? Can we obtain different, more interesting group patterns? What analytical tools can we use to better understand the effect of the social interactions on the resulting group patterns?

To answer these questions, we will derive a mathematical model for group formation and movement that takes into account how individuals receive information from conspecifics, and how this information influences the social interactions among them. In particular, we will start with the hyperbolic model proposed by Pfistner [99], and modify it to incorporate some of the ideas found in Lagrangian models (such as directional changes as a result of all three social interactions), as well as different communication mechanisms.

The outline of this thesis is as follows. In Chapter 2, we carefully describe the new nonlocal hyperbolic model we will use to investigate the formation and movement of animal groups. The model assumes density-dependent turning rates and constant speed. Also in this chapter we give a derivation of this model using correlated random walk. This provides the link between the behavior of an individual as determined by its interactions with its neighbors, and the behavior of the entire group. In Chapter 3, we investigate some theoretical aspects regarding this hyperbolic system. In particular, we discuss

the existence of mild solutions, and the reduction of this hyperbolic models to some well known nonlocal parabolic models for group formation. In Chapter 4, we perform a linear analysis of the model, to investigate the stability of the homogeneous steady states and the possibility of having heterogeneous patterns. In Chapter 5, we use these linear results to investigate numerically the spatial and spatiotemporal patterns displayed by this hyperbolic model. Then, in Chapter 6, we use weakly nonlinear theory to analyze the mechanisms that give rise to some of these patterns. Also, we study the effect of the social interactions on the structure of these patterns. In Chapter 7, we extend the model introduced in Chapter 2 to account for attractive and repulsive speeds. In Chapter 8, we conclude with a discussion of the results. In particular, we draw a parallel between our analytical and numerical results, and some empirical results obtained different animal groups. Also, we discuss some open problems and future work.

Chapter 2

Model derivation in one dimension

2.1 Introduction

In this chapter[1], we derive a new nonlocal, one-dimensional hyperbolic model used to describe the formation and movement of animal groups. As seen in Chapter 1, the one-dimensional continuum models for animal aggregations that exist in the literature, fail to account for the multitude of complex patterns one can observe in nature. These models consider that the social interactions depend only on the distances between individuals. However, this assumption might not be sufficient. In support of this statement, we propose a nonlocal mathematical model that focuses on distance-dependent and direction-dependent social interactions, facilitated by animal communication.

The basic equations for this model are derived using the classical Goldstein-Kac theory for correlated random walks (see equations (1.10)) [62],[99]. These equations describe the evolution of right-moving and left-moving individuals

[1] A version of this chapter has been published.

R. Eftimie, G. de Vries, M. A. Lewis, F. Lutscher, (2007) *Modeling group formation and activity patterns in self-organizing collectives of individuals*, Bull. Math. Biol., 69, 1537-1566.

R. Eftimie, G. de Vries, M. A. Lewis, (2007) *Complex spatial group patterns result from different communication mechanisms*, Proc. Natl. Acad. Sci., 104, 6974-6979.

who change direction randomly according to a Poisson process. As seen in the Introduction, some previous nonlocal hyperbolic models [99] assumed biased turning, that is, individuals turn only to align with their neighbors. However, not all animal movements are in response to their conspecifics. It is very likely that there is a balance between random and directed motion, depending on the group behavior. In this thesis we will combine these two modeling approaches, and assume that individuals not only turn randomly, but also they turn in response to other neighbors. Moreover, based on biological observations, we propose to incorporate two other social interactions that affect these turning rates: repulsion and attraction. We therefore assume that individuals turn to approach other neighbors that are far away, turn to avoid collision with those neighbors that are nearby, or turn to align with others. To incorporate these social interactions, we focus on communication. We use the directionality of the communication signals, as well as the ranges on which signals have effect, to define the social interactions. In particular, we formulate simple rules by which the perceived signals are translated into movement behavior. Moreover, as mentioned in the Introduction, throughout this thesis we assume that through communication, individuals gain knowledge about the number, position, and direction of movement of their neighbors.

In section 2.2, we carefully construct the model for a specific case of animal communication. We focused on this particular case to show how can we incorporate both omnidirectional and directional signals. More precisely, we assume that both attraction and repulsion involve omnidirectional signals, while alignment involves only unidirectional signals. For this particular case, we describe the nonlocal attractive, repulsive and alignment interactions, and show how can we incorporate them into the turning rates. To complete the derivation of the model, we discuss different possible boundary conditions required if the model is defined on a bounded domain.

In Section 2.3, we expand our study to focus on different animal communication signals. In this context, we discuss five hypothetical sub-models for signal reception. These sub-models are examples that illustrate how environmental and physiological constraints can be represented with this modeling

paradigm.

In Section 2.4, we show how this nonlocal model can be derived using the correlated random walk framework. We will propose a new way to incorporate different communication mechanisms into a Lagrangian model. As the space step and the time step used to discretize the domain approach zero, this Lagrangian model converges to the Eulerian model previously discussed.

2.2 Model derivation

We start with the following system of conservation laws that describes the evolution of densities of right-moving ($u^+(x,t)$) and left-moving ($u^-(x,t)$) individuals (see [99],[100]):

$$\begin{aligned} u_t^+(x,t) + (\gamma u^+(x,t))_x &= -\lambda^+[u^+,u^-]u^+(x,t) + \lambda^-[u^+,u^-]u^-(x,t), \\ u_t^-(x,t) - (\gamma u^-(x,t))_x &= \lambda^+[u^+,u^-]u^+(x,t) - \lambda^-[u^+,u^-]u^-(x,t), \\ u^\pm(x,0) &= u_0^\pm(x), x \in \mathbf{R}. \end{aligned} \tag{2.1}$$

Here, γ is their constant speed, and λ^+ (λ^-) is the turning rate for the individuals that were initially moving to the right (left) and then turn to the left (right). We assume that these turning rates depend on the density of left-moving and right-moving neighbors.

A similar model has been proposed in [99] to describe the alignment behavior in Myxobacteria colonies. There, the authors assumed that the turning rates depend only on the alignment interaction. We will modify their assumption to include also the dependence on the attractive and repulsive interactions. In the following, we will carefully describe this dependence. In Subsection 2.2.1 we will discuss the random and directed components of the turning rates. Then, in Subsection 2.2.2, we will show how to incorporate signal reception into the turning rates. To complete the definition of the model, in Subsection 2.2.3 we discuss possible boundary conditions.

2.2.1 Turning rates

To define the turning rates, we start with the hypothesis made by many Lagrangian models, namely that each individual interacts with its neighbors via three social forces, attraction, repulsion, and alignment [24, 58, 95, 108]. We further assume that each of these forces has a different interaction range (Figure 2.1(a)). More specifically, we assume that an individual changes direction to approach other individuals if they are within its attraction range, or to avoid collision if they are within its repulsion range. Moreover, an individual turns to match its orientation to its neighbors' direction of movement (i.e., to align) if they are within its alignment range. Since we derive a 1D model,

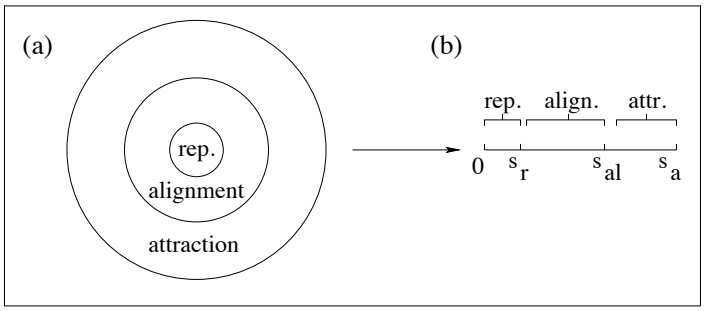

Figure 2.1: Illustration of the repulsion (s_r), alignment (s_{al}), and attraction (s_a) zones: (a) 2D case; (b) 1D case. It is biologically realistic to have $s_r < s_{al} < s_a$.

the concentric circles that usually describe the interaction ranges in 2D Lagrangian models (Figure 2.1(a)) are replaced by intervals on the real number line (Figure 2.1(b)).

While model (2.1) is formally identical with the model introduced in [99],[100], the biological processes considered in the turning functions differ considerably. Pfistner [100] only modeled alignment and used turning functions that were positive, unbounded and increasing functions of the signals perceived from neighbors within a certain perception distance. We, on the other hand, assume that all three social interactions influence the turning rates, so that $\lambda^{\pm}$ models attraction, repulsion, and alignment as a response of an individual to the signals perceived from its neighbors. We assume that stronger interaction

forces lead to higher turning rates (to avoid collision, for example, in case of high repulsion), and consider the turning rates to be bounded, positive, monotone functions of the perceived signals $y^{\pm}$, which are emitted by individuals moving to the right (u^+) and to the left (u^-) :

$$\begin{aligned} \lambda^{\pm}(y^{\pm}[u^+,u^-]) &= \lambda_1 + \lambda_2 f\left(y^{\pm}[u^+,u^-]\right) \\ &= (\lambda_1 + \lambda_2 f(0)) + \lambda_2\left(f(y^{\pm}[u^+,u^-]) - f(0)\right), \end{aligned} \quad (2.2)$$

where $\lambda_1 + \lambda_2 f(0)$ is a base-line random turning rate, and $\lambda_2\left(f(y^{\pm}) - f(0)\right)$ is a bias turning rate. We choose f to be a dimensionless, bounded and increasing function of the dimensionless functionals $y^{\pm}[u^+,u^-]$ which incorporate nonlocal interaction terms:

$$y^{\pm}[u^+,u^-] = y_r^{\pm}[u^+,u^-] - y_a^{\pm}[u^+,u^-] + y_{al}^{\pm}[u^+,u^-]. \quad (2.3)$$

Here, $y_r^{\pm}$, $y_{al}^{\pm}$ and $y_a^{\pm}$ denote the repulsion, alignment, and attraction terms that influence the likelihood of turning to the left (+) or to the right (−). We will specify the dependence of these terms on u^+ and u^- in Section 2.2.2. The three interactions are introduced in an additive manner, with repulsive and attractive terms having opposite effects. Throughout this chapter, as well as Chapters 4, 5, and 6, we use the following turning function (Figure 2.2):

$$f\left(y^{\pm}[u^+,u^-]\right) = 0.5 + 0.5\tanh\left(y^{\pm}[u^+,u^-] - y_0\right), \quad (2.4)$$

where the constant y_0 is chosen such that $f(0) \ll 1$ and the random turning dominates the movement. In this case, the base-line turning can be approximated by λ_1, and the change in turning rate due to interactions by $\lambda_2 f(y^{\pm})$.

2.2.2 Modeling repulsive, attractive, and alignment interactions

In order to describe the dependence of the social interactions, $y_r^{\pm}$, $y_{al}^{\pm}$ and $y_a^{\pm}$, on u^+ and u^-, we look at the way organisms perceive and integrate information. We assume that both the direction and the spatial range of the signals

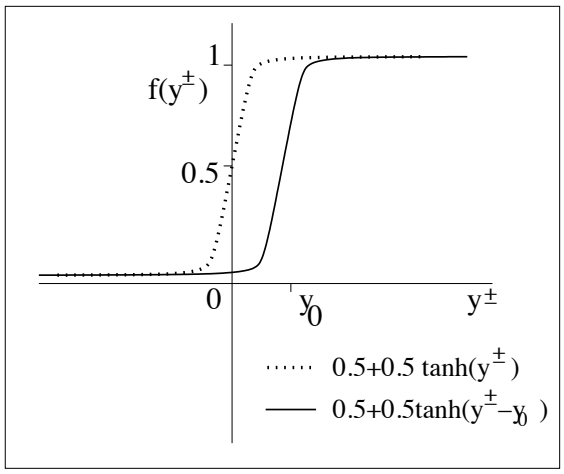

Figure 2.2: A turning function that satisfies our assumptions: increasing, positive and bounded. The constant y_0 shifts the graph to the right such that for $y^{\pm} = 0$, there is only a small random turning.

define the social interactions. We introduce four parameters that measure the information received from the right or left, $p_r^{\pm}$ and $p_l^{\pm}$, respectively. The superscript $(\pm)$ refers to the direction in which the sender of the information moves, and the subscript (r, l) refers to the direction from which the signal is received (right, left) (Figure 2.3). Later, for the sake of simplicity, the analysis will concentrate on special cases.

By way of example, suppose that the individual positioned at (x, t) moves to the right $(+)$ (Figure 2.3(a)), and that it receives information from other individuals located to its right, at $x + s$, and located to its left, at $x - s$. Also, suppose that this individual perceives a stronger signal from the right than from the left, that is, $(p_r^+ u^+ + p_r^- u^-)(x + s) > (p_l^- u^- + p_l^+ u^+)(x - s)$. If the signal comes from within the repulsion zone, then it will turn to avoid those neighbors that are to its right, regardless of their orientation. If the signal comes from within the attraction zone, it will continue moving in the same direction.

For simplicity, we choose $p_r^+ = p_r^- = p_r$ and $p_l^+ = p_l^- = p_l$. If we sum the information from all neighbors ($s \in (0, \infty)$), we can translate the diagrams from Figure 2.3 into the following nonlocal terms that describe the social

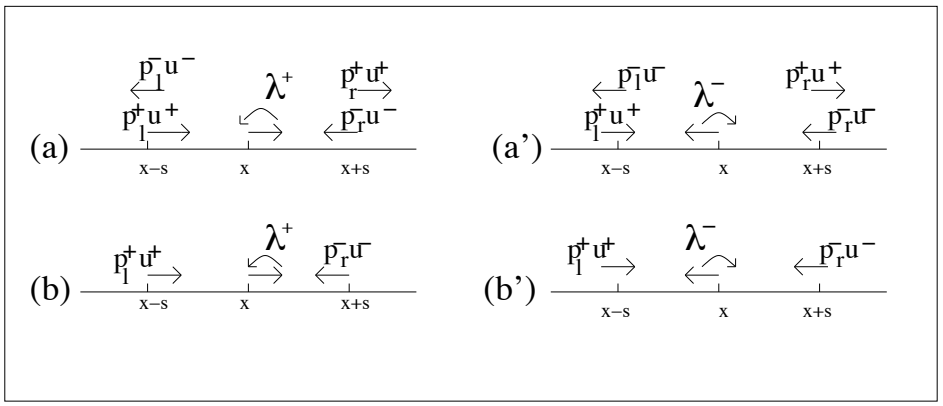

Figure 2.3: Description of possible turning functions. Cases (a)-(b) depict a switch in movement direction from right to left, while cases (a')-(b') depict the switch in movement direction from left to right. Cases (a), (a') describe attraction and repulsion, while (b) and (b') describe alignment. Here u^+ (u^-) represents the density of individuals moving right (left), and λ^+ (λ^-) is the probability of turning to the left (right), when initially the individual at x was moving to the right (left). The other parameters, $p_l^{\pm}$ and $p_r^{\pm}$, represent signals received from the left (subscript l) and the right (subscript r), from other neighbors that are moving to the left (superscript "–") or to the right (superscript "+").

interactions:

$$y_{r,a}^{+}[u^+,u^-] = q_{r,a}\int_0^\infty K_{r,a}(s)\left(p_r u(x+s) - p_l u(x-s)\right)ds, \tag{2.5}$$

$$y_{r,a}^{-}[u^+,u^-] = q_{r,a}\int_0^\infty K_{r,a}(s)\left(p_l u(x-s) - p_r u(x+s)\right)ds, \tag{2.6}$$

$$y_{al}^{+}[u^+,u^-] = q_{al}\int_0^\infty K_{al}(s)\left(p_r u^-(x+s) - p_l u^+(x-s)\right)ds, \tag{2.7}$$

$$y_{al}^{-}[u^+,u^-] = q_{al}\int_0^\infty K_{al}(s)\left(p_l u^+(x-s) - p_r u^-(x+s)\right)ds, \tag{2.8}$$

where $K_j(s), j \in \{a, r, al\}$ are interaction kernels, with support inside the interval $[0,\infty)$, that describe how signals from different distances are weighed. The parameters q_a, q_r, and q_{al} represent the magnitudes of the attraction, repulsion, and alignment forces, respectively. For attraction and repulsion, the total density of organisms at a specific position in space is important: $u(x \pm s, t) = u^+(x \pm s, t) + u^-(x \pm s, t)$, $s > 0$. We assume here that as long as

the individual located at x moves towards neighbors that are in the repulsion zone, it will turn to avoid collision, no matter what the movement direction of those neighbors is. Similarly, the individual is attracted by neighbors within its attraction zone, regardless of their orientation. For alignment, on the other hand, we assume that an individual responds *only to neighbors moving towards it.* For example, for y_{al}^{+} (equation (2.7)), we assume that a right-moving individual at point x will turn around only if $p_r u^{-}(x+s)$ is large relative to $p_l u^{+}(x-s)$.

In summary, the right-hand sides of equations (2.5) – (2.8) describe how the individual at (x,t) weighs information received from its right and left neighbors. The only difference between the repulsion term ($y_r^{\pm}[u^+,u^-]$) and the attraction term ($y_a^{\pm}[u^+,u^-]$) is in the range over which the two kernels $K_r(s)$ and $K_a(s)$ have influence (Figure 2.4). Recall that since repulsion and attraction have opposite effects, these two terms enter the turning function (equation (2.3)) with different signs.

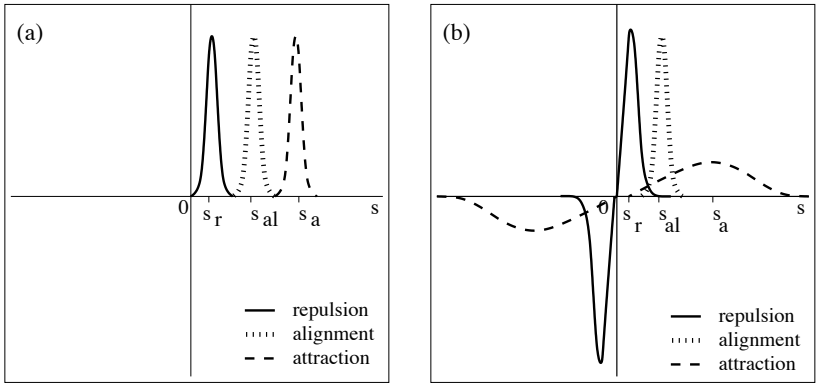

Figure 2.4: Examples of kernels used for social interactions. These kernels describe how signals from different distances are weighed. (a) translated Gaussian kernels for attraction, repulsion and alignment, described by equations (2.9); (b) odd kernels for attraction and repulsion, and a translated Gaussian kernel for alignment (equations (2.11) and (2.9)). Both types of kernels are defined on $(-\infty,\infty)$. The interaction ranges on which these kernels have an effect, satisfy $s_r < s_{al} < s_a$. The s_r, s_{al} and s_a represent half the length of the interaction ranges depicted in Figure 2.1.

A possible choice for the interaction kernels is translated Gaussian kernels

(Figure 2.4(a)):

$$K_j(s) = \frac{1}{\sqrt{2\pi m_j^2}} \exp\left(-(s-s_j)^2/(2m_j^2)\right),\ j = r, a, al,\ s \in [0, \infty), \quad (2.9)$$

with $m_j = s_j/8$ $(j = r, al, a)$ representing the width of the interaction kernels, and s_i $(j = r, al, a)$ representing half the length of the interaction ranges, for the repulsion, alignment, and attraction terms, respectively. For a biologically realistic case, we consider $s_r < s_{al} < s_a$. The constants m_j are chosen such that the support of more than 98% of the mass of the kernels is inside the interval $[0, \infty)$: $m_j = s_j/8$, $j \in \{r, al, a\}$. In this case, the integrals defined on $[0, \infty)$ can be approximated by integrals on $(-\infty, \infty)$.

To simplify the model equations for the purpose of analysis, we choose $p_l = p_r$ (the case $p_l \neq p_r$ will be discussed in Chapters 3 and 5). Moreover, these parameters will be incorporated into the magnitudes of repulsion q_r, alignment q_{al}, and attraction q_a. Then, if we extend K_r and K_a to odd kernels on the whole real line, equations (2.5) and (2.6) can be rewritten as

$$y_{r,a}^{\pm}[u^+, u^-] = q_{r,a} \int_{-\infty}^{\infty} K_{r,a}(s) u(x \pm s) ds. \quad (2.10)$$

A second possible choice, similar to [80], is to define the attraction and repulsion kernels by (Figure 2.4(b))

$$K_j(s) = \frac{s}{2s_j^2} \exp\left(-s^2/(2s_j^2)\right),\ j = a, r,\ s \in (-\infty, \infty). \quad (2.11)$$

The two model formulations (kernels on the half-line, and odd extensions on the full line) are equivalent. Equation (2.10) together with Figure 2.4(b) show that if a right- or left-moving individual perceives many neighbors ahead of it, the likelihood of turning will increase in case of repulsion, or decrease in case of attraction. Conversely, the perception of many neighbors behind that individual will lead to a decrease in the turning rates in case of repulsion, or to an increase in these rates in case of attraction. Since an individual needs to distinguish movement directions and not just densities of its neighbors (i.e., u^+, u^- vs. u) in order to align, we do not use odd alignment kernels.

Altogether, equations (2.3)-(2.11) describe aspects of how an organism at (x, t) makes the decision to turn: it turns to avoid collision if the majority of the stimuli received originate within the repulsion zone, or to approach other individuals if the majority of the stimuli received originate within the attraction zone. If the majority of the stimuli originate within the alignment zone, the individual will turn to align itself according to the prevailing movement direction of the neighbors moving towards it.

The full model has 14 parameters, summarized in Table 2.1. While nondimensionalizing allows us to reduce the number of parameters to 10, the analysis is no more difficult when dealing with the dimensional form, which we will do in the following. Moreover, the original parameters are biologically motivated. It is easier to interpret the results of the model (Chapters 4, 5, and 8) by talking about the model using these parameters in their original biological context.

2.2.3 Boundary conditions

Throughout most of the chapters, we study system (2.1) on a finite domain of length L, that is $x \in [0, L]$. To complete the model, we therefore have to define the boundary conditions. Note that since the system is hyperbolic, we have to follow the characteristics of the system when imposing these boundary conditions. For this reason, u^+ is prescribed only at $x = 0$, while u^- is prescribed only at $x = L$ [44]. In the following, we discuss five types of possible boundary conditions.

- **Periodic boundary conditions**

  These boundary conditions model the movement on a circular domain. Individuals leave the domain at one end, and enter it again at the other end. The conditions are described by the following equations:

  $$u^+(0, t) = u^+(L, t), \quad u^-(L, t) = u^-(0, t). \tag{2.12}$$

  Throughout this thesis, we use only periodic boundary conditions to allow for comparison with other models. For example, Igoshin et. al. [60]

Parameter	**Description**	**Units**	**Fixed value**
γ	Speed	S/T	no: $\gamma \in (0.015, 0.1)$
λ_1	Turning rate. It approximates the baseline turning rate: $\lambda_1 + \lambda_2 f(0)$	1/T	no: $\lambda_1 \in (0.2, 1.33)$
λ_2	Turning rate. It approximates the bias turning rate: $\lambda_2 \left(f(y^{\pm}) - f(0)\right)$	1/T	no: $\lambda_2 \in (0.9, 6)$
y_0	Shift of the turning function	1 (nondim.)	yes: $y_0 = 2$
q_a	Magnitude of attraction	S/N	no: $q_a \in (0, 15)$
q_{al}	Magnitude of alignment	S/N	no: $q_{al} \in (0, 2)$
q_r	Magnitude of repulsion	S/N	no: $q_r \in (0, 2)$
s_a	Attraction range	S	yes: $s_a = 1$
s_{al}	Alignment range	S	yes: $s_{al} = 0.5$
s_r	Repulsion range	S	yes: $s_r = 0.25$
m_a	Width of attraction kernel	S	yes: $m_a = 1/8$
m_{al}	Width of alignment kernel	S	yes: $m_{al} = 0.5/8$
m_r	Width of repulsion kernel	S	yes: $m_r = 0.25/8$
A	Total population size	N	yes: $A = 2$

Table 2.1: A summary of the model parameters. The two parameters for the strength of information received from left/right, namely p_l/p_r, are already incorporated into the magnitudes of attraction q_a, alignment q_{al}, and repulsion q_r. The last column specifies if the parameter will be kept fixed during the analysis of the model (Chapters 4 and 6), and the numerical simulations (Chapter 5). *Note: T represents unit time, S is unit space, and N is number of individuals.*

obtained rippling behavior on a periodic domain, and compared their results with the experimentally observed patterns. Further, Buhl et. al. [17] used a one-dimensional individual-based model with periodic boundary conditions to study the transition from disordered to ordered movement. Their results show remarkable agreement between the theoretical results and the biological observations. Also, as we will see in Chapter 5, the periodic boundary conditions allow us to observe traveling pulses, a pattern which could not be observed with a nonlocal parabolic model with constant diffusion [80]. Note that a bounded domain with periodic boundary conditions can be treated as an infinite domain.

- **Neumannn boundary conditions**

  The Neumann boundary conditions are used to model the reflection of the boundaries. Individuals that arrive at the boundary will turn around immediately and move in the opposite direction:

$$u^-(L,t) = u^+(L,t), \quad u^+(0,t) = u^-(0,t). \tag{2.13}$$

  These boundary conditions can be used when the animal group is trapped inside a closed domain (e.g., a swarm of insects inside a closed room).

- **Dirichlet boundary conditions**

  This type of boundary conditions assumes that the individuals that arrive at the boundaries are absorbed, and no other individuals emerge here:

$$u^+(0,t) = 0, \quad u^-(L,t) = 0. \tag{2.14}$$

  These conditions can be used if the habitat outside the domain of interest is so hostile that animals reaching the boundaries perish immediately [124].

- **Open boundary conditions**

  This type of boundary conditions are used in traffic equations because they are more realistic than the periodic boundary conditions [47]. The conditions assume that there is a fixed rate at which particles enter the

system through one boundary. The particles leave the system as soon as they reach the other boundary.

$$u^+(0,t) = c_1, \quad u^-(L,t) = c_2. \tag{2.15}$$

Note that, to keep the total density conserved, the rate of entering the domain has to be equal to the rate of leaving it, that is, $c_1 = c_2$.

These boundary conditions work for local interactions, but may pose a problem for the nonlocal terms. If we inject individuals at one end of the boundary, we implicitly assume that there are other individuals outside the domain. The movement directions of an individual inside the domain but close to the boundary will therefore be influenced by the moving directions of those neighbors that have left the domain, but are still within its repulsion/alignment/attraction range. Hence, to describe the behavior of those individuals inside the domain, we have to know the behavior of their neighbors that are outside the domain.

On the other hand, if we assume that there are no other individuals outside the domain, we can follow the evolution of the groups inside the domain only for a short period of time, until these groups reach the boundary. An alternative to open boundary conditions is to apply periodic boundary conditions on a domain that is much larger than the domain of interest [47].

- **Moving boundary conditions**

  The previous four types of boundary conditions are commonly employed by most of the mathematical models for traffic, and group formation and movement [29], [30], [47], [60], [71], [123]. There are, however, some one-dimensional hyperbolic models that use a different type of boundary conditions, namely moving boundary conditions [43], [65], [100]. In this case, the formation and movement of animal groups is studied through the expansion and retraction of the boundaries. However, this requires extra equations for the moving boundaries. It is beyond the scope of this research to study this case. Nevertheless, it will be an interesting case

for further study.

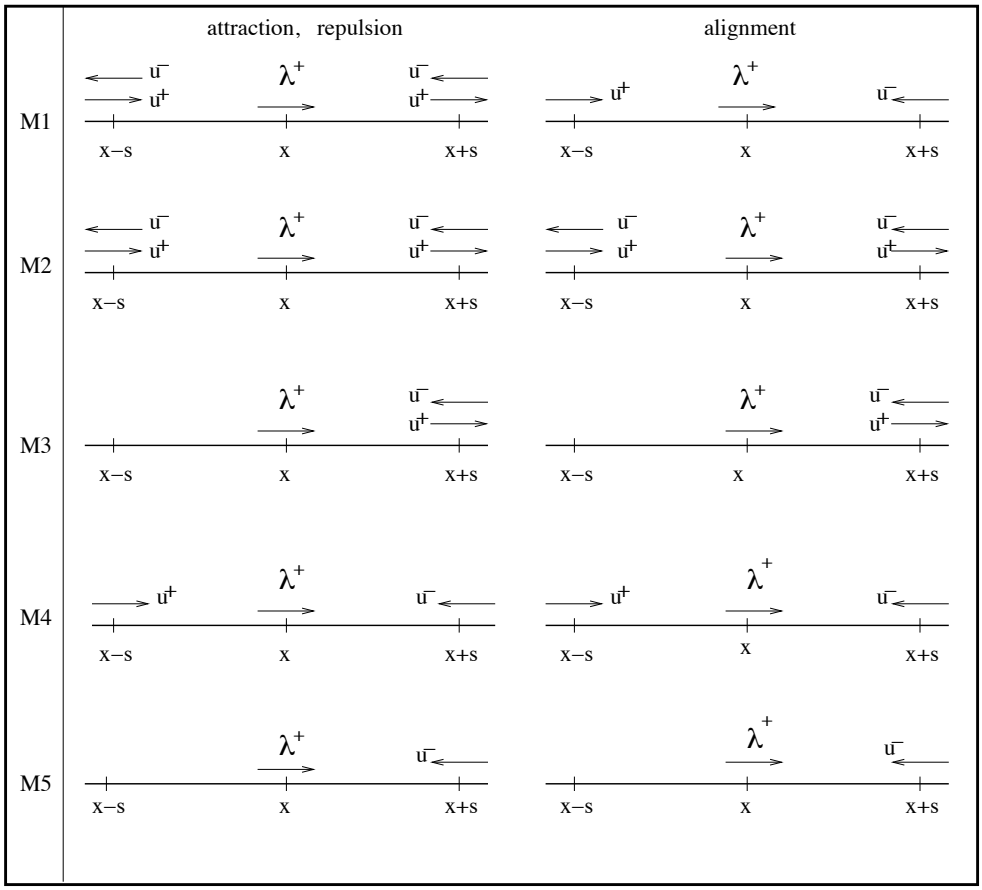

Figure 2.5: Five sub-models for signal reception. A reference right-moving individual is positioned at x. Its right-moving (u^+) and left-moving (u^-) neighbors are positioned at $x + s$ and $x - s$. **M1**: for attraction and repulsion, the information is received from all neighbors, while for alignment the information is received only from those moving towards the reference individual. **M2**: information is received from all neighbors (for attraction, repulsion and alignment). **M3**: information received only from ahead (with respect to the moving direction of the reference individual). **M4**: information received from ahead and behind, but only from those neighbors moving towards the reference individual. **M5**: information received only from ahead, and only from those neighbors moving towards the reference individual.

2.3 Alternative sub-models based on different communication mechanisms

In the previous section, we have discussed a particular case of signal reception. More precisely, we considered omnidirectional signals for attractive and

repulsive interactions, and directional signals for alignment interactions. However, there is evidence suggesting that not all animals receive and respond in a similar manner to the signals coming from their neighbors. For example, we mentioned in Introduction that for some species (e.g., the Mormon crickets) the movement is likely influenced by signals received from behind, while for other species (e.g., fish) the movement is influenced by signals received from ahead.

In the following, we focus on some different hypothetical sub-models for signal reception. In the previous three subsections, we chose the attractive and repulsive interactions to depend on information received from all neighbors, no matter whether they are moving away from, or towards an individual. Alignment, on the other hand, depends only on the information received from those neighbors moving towards an individual. The question that arises immediately is: what happens if we consider different reception mechanisms? A few individual-based models (e.g., [24, 58]) assume that individuals may not receive information from behind because of a so-called "blind spot". We go further and derive five hypothetical communication sub-models, to describe how an individual can receive information from its neighbors. These sub-models are examples that illustrate how environmental and physiological constraints can be represented with our modeling paradigm.

The five sub-models (M1-M5) are described in Figure 2.5. We focus here on a reference right-moving individual that is positioned at x, whereas its neighbors are potentially positioned at $x + s$ (ahead), and at $x - s$ (behind). The sub-models are defined as follows:

- M1: the attractive and repulsive interactions depend on the stimuli received from all neighbors, whereas the alignment depends only on the stimuli received from those neighbors moving towards the reference individual (this case was studied in the previous three subsections);

- M2: all three social interactions depend on the stimuli received from all neighbors;

- M3: the social interactions depend only on the information received from

Model	Attraction and Repulsion	Alignment
M1	$y_{r,a}^{\pm} = q_{r,a}\int_0^\infty K_{r,a}(s)(u(x\pm s) - u(x\mp s))ds$	$y_{al}^{\pm} = q_{al}\int_0^\infty K_{al}(s)(u^{\mp}(x\pm s) - u^{\pm}(x\mp s))ds$
M2	$y_{r,a}^{\pm} = q_{r,a}\int_0^\infty K_{r,a}(s)(u(x\pm s) - u(x\mp s))ds$	$y_{al}^{\pm} = q_{al}\int_0^\infty K_{al}(s)(u^{\mp}(x\pm s) + u^{\mp}(x\mp s) - u^{\pm}(x\pm s) - u^{\pm}(x\mp s))ds$
M3	$y_{r,a}^{\pm} = q_{r,a}\int_0^\infty K_{r,a}(s)(u(x\pm s))ds$	$y_{al}^{\pm} = q_{al}\int_0^\infty K_{al}(s)(u^{\mp}(x\pm s) - u^{\pm}(x\pm s))ds$
M4	$y_{r,a}^{\pm} = q_{r,a}\int_0^\infty K_{r,a}(s)(u^{\mp}(x\pm s) - u^{\pm}(x\mp s))ds$	$y_{al}^{\pm} = q_{al}\int_0^\infty K_{al}(s)(u^{\mp}(x\pm s) - u^{\pm}(x\mp s))ds$
M5	$y_{r,a}^{\pm} = q_{r,a}\int_0^\infty K_{r,a}(s)u^{\mp}(x\pm s)ds$	$y_{al}^{\pm} = q_{al}\int_0^\infty K_{al}(s)u^{\mp}(x\pm s)ds$

Table 2.2: The nonlocal terms used to describe the social interactions. The terms $y_{r,a}^{+}$ and y_{al}^{+} are the translation of the diagrams from Figure 2.5 into mathematical equations, when we sum up the information received from all neighbors ($s \in [0,\infty)$). The terms $y_{r,a}^{-}$ and y_{al}^{-} are obtained through a similar process, when we consider a left-moving reference individual. We define q_a, q_r, and q_{al} to be the strength of the attraction, repulsion, and alignment forces. Also, we define u to be the total density $u = u^{+} + u^{-}$.

ahead (with respect to the moving direction);

- M4: the social interactions depend on the stimuli received from ahead and behind, only from those neighbors moving towards the reference individual;

- M5: the social interactions depend on stimuli received only from ahead, and only from neighbors moving towards the reference individual.

We emphasize here that for attractive and repulsive interactions, these five communication mechanisms convey only the position of the neighbors. For alignment, on the other hand, they convey also the direction of movement of those neighbors located within the alignment range.

Note that model M2 is the immediate generalization of model M1. For example, M2 can describe the situation where individuals receive information from all their neighbors via omnidirectional sound or chemical signals. Model M3 can describe the situation where individuals use only unidirectional visual signals. They can see neighbors in front of them, but they cannot see anyone behind them. Model M4 can describe the situation where individuals use unidirectional sound signals. In this case, individuals only hear the sounds produced by those neighbors moving towards them. They do not receive any information from neighbors moving away from them. Model M5 is a particular case of model M3. Here, the turning rates depend only on the information received from neighbors moving in the opposite direction. This assumption can describe the communication mechanisms in colonies of Myxobacteria [59], [71].

Table 2.2 describes the nonlocal terms obtained by summing up the information from all neighbors ($s \in (0, \infty)$), as depicted in the diagrams of Figure 2.5. As in Section 2.2, the total density at (x, t) is $u(x, t) = u^+(x, t) + u^-(x, t)$. The interaction kernels are described by equations (2.9).

We emphasize again that these five sub-models are not the only possible ones. The aim here is not to describe all the possible ways of receiving information from neighbors. Rather, it is to give the reader a flavor of the possibilities offered by such a modeling procedure.

2.4 Model derivation from correlated random walk

In Section 2.2, we derived the model by starting with a known hyperbolic model, and changing the nonlocal turning rates to incorporate different social interactions and communication mechanisms. In the following, we show how the nonlocal system (2.1) can be derived from a correlated random walk.

Let us discretize space into small intervals of length Δx, and time into intervals of length Δt. For a population of size N, the probability of a *randomly chosen right or left-moving individual* to be found on the interval $[x-\Delta x/2, x+\Delta x/2)$ at time t, is defined as [41, 67],

$$p^{\pm}(x,t) = \frac{1}{N}\int_{x-\Delta x/2}^{x+\Delta x/2} u^{\pm}(s,t)ds \longrightarrow \frac{\Delta x u^{\pm}(x,t)}{N} \text{ when } \Delta x \to 0. \tag{2.16}$$

The classical Goldstein-Kac theory for correlated random walk (equations (1.9)) assumes that the probability of changing direction has only a random component. We, on the other hand, will assume that the probability to change direction has two components: a random component and a directed component. Therefore, the probability of a right-moving (left-moving) individual to turn left (right) is given by

$$\begin{aligned} \lambda^{\pm} &= \text{probability of turning randomly} + \\ &\quad \text{probability of turning left/right in response to distant neighbors} \\ &= \frac{\lambda_1}{2} + \frac{\lambda_2}{2}F^{\pm}. \end{aligned} \tag{2.17}$$

Here, $F^{\pm}$ are nondimensional, increasing, uniformly continuous functions of the difference between the right-moving and left-moving neighbors that are located far away. We choose $0 < \lambda_1,\ \lambda_2,\ F^{\pm} < 1$. To make things simpler, we will assume for now that individuals turn *only to align with neighbors located within the alignment range*. We will discuss the attractive and repulsive interactions at the end of this section. Moreover, we consider the communication mechanism introduced in Section 2.2, that is, the mechanism used for model M1. For this, we assume that the probability that an individual changes direction will increase if there are more distant neighbors in front of it, who

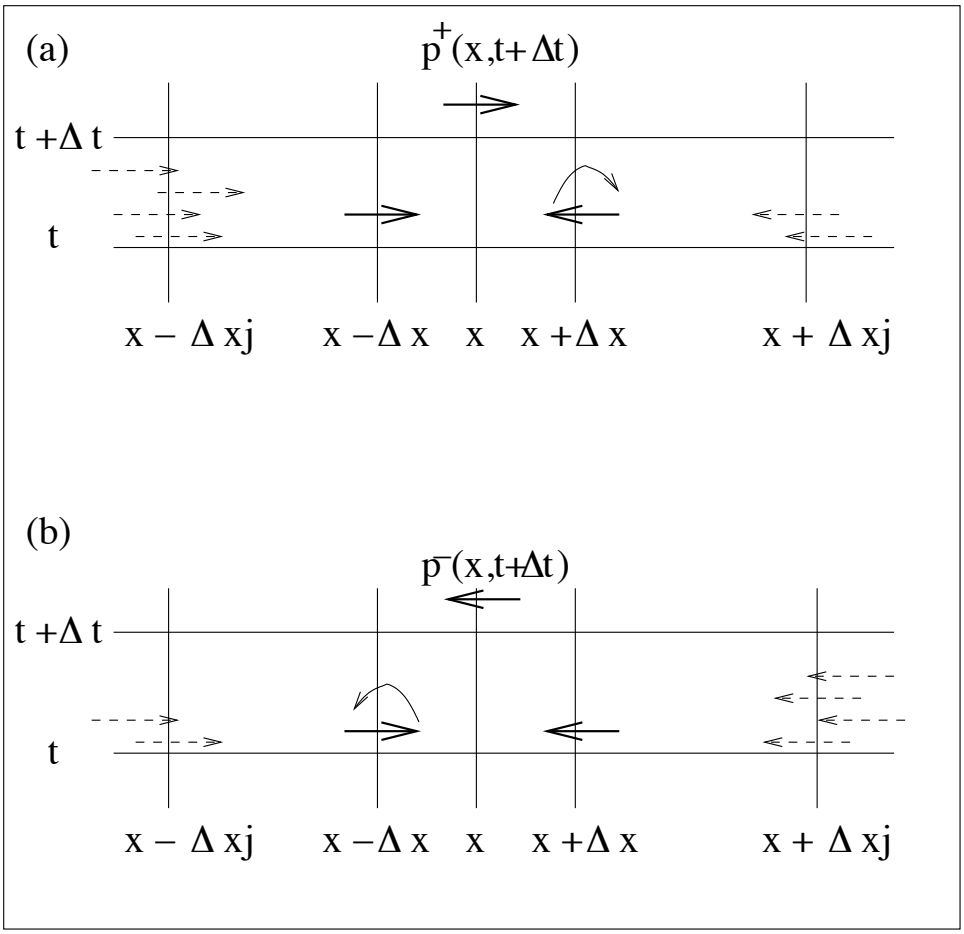

Figure 2.6: The movement of (a) a right-moving individual, and (b) a left-moving individual. The decision to change direction depends on the previous position at time t: the individual was either at $x - \Delta x$, or at $x + \Delta x$. Also, it depends on the movement direction of those neighbors positioned at $x - \Delta xj$ and $x + \Delta xj$, for some $j \gg 1$. In particular, an individual positioned at $x + \Delta x$ and moving left (case (a)), can turn randomly, or can turn if there are more neighbors in front of it, at $x - \Delta xj$, moving in the opposite direction. A similar explanation holds for (b).

are moving in the opposite direction, than neighbors behind it, moving in the same direction (see Figure 2.6). The probability will decrease if there are more distant neighbors behind it, who are moving in the same direction. Hence, $F^{\pm}$ will be defined in terms of the difference between right-moving and left-moving neighbors that are within the alignment range.

Before giving the expression for $F^{\pm}$, we will make one more assumption. In particular, we will assume that *all other individuals have the same probabilities* $p^{\pm}(x,t)$*,* independent of the location of the right-moving or left-moving individual chosen previously (see equations (2.16)). Hence, if the chosen individual is at point x, then the expected number of individuals at distance $j\Delta x$, that are moving right or left, is $Np^{\pm}(x+j\Delta x,t)$. Under these assumptions, the probability of turning in response to distant neighbors is described by

$$F^{\pm} = F\left(\pm N \sum_{j=-\infty}^{\infty} K_{al}(j\Delta x)\left(p^{-}(x+j\Delta x,t) - p^{+}(x-j\Delta x,t)\right)\right), \quad (2.18)$$

where F is a uniform continuous function of the difference between the left-moving and right-moving neighbors positioned within the alignment range. The kernels K_{al} are described by equations (2.9). Substituting (2.17) and (2.18) into equations (1.9), leads to

$$\begin{aligned}
p_t^+ + \frac{\Delta x}{\Delta t}p_x^+ &= -p^+\left(\frac{\lambda_1}{2} + \frac{\lambda_2}{2}F\left(N\sum_{j=-\infty}^{\infty} K_{al}(j\Delta x)(p^-(x+j\Delta x,t) - p^+(x-j\Delta x,t))\right)\right) \\
&+ p^-\left(\frac{\lambda_1}{2} + \frac{\lambda_2}{2}F\left(-N\sum_{j=-\infty}^{\infty} K_{al}(j\Delta x)(p^-(x+j\Delta x,t) - p^+(x-j\Delta x,t))\right)\right) \\
&+ O(\Delta x) \text{ terms} \\
p_t^- - \frac{\Delta x}{\Delta t}p_x^- &= p^+\left(\frac{\lambda_1}{2} + \frac{\lambda_2}{2}F\left(N\sum_{j=-\infty}^{\infty} K_{al}(j\Delta x)(p^-(x+j\Delta x,t) - p^+(x-j\Delta x,t))\right)\right) \\
&- p^-\left(\frac{\lambda_1}{2} + \frac{\lambda_2}{2}F\left(-N\sum_{j=-\infty}^{\infty} K_{al}(j\Delta x)(p^-(x+j\Delta x,t) - p^+(x-j\Delta x,t))\right)\right) \\
&- O(\Delta x) \text{ terms.} \qquad (2.19)
\end{aligned}$$

Now let $\Delta x, \Delta t \to 0$, such that $\frac{\Delta x}{\Delta t} \to \gamma$. Since we assumed that F is uniformly continuous, we can interchange the limit and the function. Multiplying

equations (2.19) by N, and using equation (2.16), we obtain

$$\begin{aligned}
u_t^+ + \gamma u_x^+ &= -u^+\left(\frac{\lambda_1}{2} + \frac{\lambda_2}{2}F\left(\int_{-\infty}^{\infty} K_{al}(s)(u^-(x+s,t) - u^+(x-s,t))\right)\right) \\
&+ u^-\left(\frac{\lambda_1}{2} + \frac{\lambda_2}{2}F\left(-\int_{\infty}^{\infty} K_{al}(s)(u^-(x+s,t) - u^+(x-s,t))\right)\right) \\
u_t^- - \gamma u_x^- &= u^+\left(\frac{\lambda_1}{2} + \frac{\lambda_2}{2}F\left(\int_{-\infty}^{\infty} K_{al}(s)(u^-(x+s,t) - u^+(x-s,t))\right)\right) \\
&- u^-\left(\frac{\lambda_1}{2} + \frac{\lambda_2}{2}F\left(-\int_{-\infty}^{\infty} K_{al}(s)(u^-(x+s,t) - u^+(x-s,t))\right)\right).
\end{aligned} \tag{2.20}$$

Here, $u^{\pm}$ are probability density functions.

In a similar way, one can incorporate attraction and repulsion. The resulting turning rates will be defined as

$$\begin{aligned}
\lambda^{\pm} &= \frac{\lambda_1}{2} + \frac{\lambda_2}{2}F\left(\pm N\sum_{j=-\infty}^{\infty} K_r(j\Delta x)(p(x+j\Delta x,t) - p(x-j\Delta x,t))\right. \\
&\mp N\sum_{j=-\infty}^{\infty} K_a(j\Delta x)(p(x+j\Delta x,t) - p(x-j\Delta x,t)) \\
&\left.\pm N\sum_{j=-\infty}^{\infty} K_{al}(j\Delta x)(p^-(x+j\Delta x,t) - p^+(x-j\Delta x,t)),\right)
\end{aligned} \tag{2.21}$$

with $p = p^+ + p^-$. This definition of the turning rates corresponds to the communication mechanism proposed for model M1 (and discussed in Section 2.2). However, one can consider different mechanisms corresponding to models M2-M5 (see Figure 2.5), and incorporate them into this random-walk approach.

Therefore, this modeling framework presents a straightforward way to incorporate animal communication into a Lagrangian model. Moreover, there is a clear connection between this Lagrangian model and the corresponding limiting Eulerian model. This allows us to tie the resulting group properties to different individual behaviors. However, we have not investigated the behavior of this random walk model. This is a subject for future research (see Chapter 8).

2.5 Discussion

In this chapter, we have discussed a one-dimensional nonlocal hyperbolic model that we will use to study the formation and movement of animal groups. The starting point was a model proposed by Pfistner and Alt to study the alignment behavior in Myxobacteria colonies [99]. We modified this model by changing the nonlocal turning rates to incorporate the assumptions made by many Lagrangian models, namely that individual behavior is determined by three social interactions: attraction, repulsion, and alignment. The way these social interactions were incorporated depended on some assumptions that we made about animal communication. In particular, we assumed that an organism changes its movement direction only after weighing the information received from left and right. Moreover, the received information depends on the type of communication signals used by those organisms. The social interactions were thus defined in terms of communication and distances, and not just distance alone.

The resulting model presents a straightforward way to incorporate different animal communication mechanisms. We can easily incorporate information that comes from all neighbors, as well as information that comes only from particular neighbors. To demonstrate this, we then derived five hypothetical sub-models for signal reception. These sub-models can account for different communication mechanisms used by different animal communities. It should be specified that these sub-models do not describe all the possible ways of receiving information. The aim here was to give a glimpse of the many possibilities offered by such a modeling procedure. The model can be easily adapted to account for other types of reception mechanisms. For example, one may assume that individuals can see all their neighbors that are in front of them, and can hear only those neighbors that are behind and moving towards them. In Chapter 4, we will show that these sub-models exhibit a wide variety of previously undescribed spatial and spatiotemporal patterns.

Moreover, in this chapter we proposed a new approach to derive the nonlocal hyperbolic model using the correlated random walk framework. This

approach allows us to incorporate animal communication into a stochastic individual-based model. Also, it provides the connection between the Lagrangian and Eulerian frameworks. In general, the advantage of Lagrangian models is that they can be related to experimental data. For small time and space steps, the Lagrangian model we propose here converges to the Eulerian model introduced in Section 2.2. Therefore, using this modeling approach, one can try to go further, and relate the Eulerian model with experimental data. Finally, this approach allows us to connect the resulting group patterns to individual behaviors.

In the following chapter, we begin to analytically investigate the hyperbolic model discussed here. In particular, we will focus on the existence of solutions for this hyperbolic system, and the reduction of this model to a well known nonlocal parabolic model used to study animal group formation (equations (1.2)). In Chapter 4, we will start investigating analytically the patterns displayed by this hyperbolic model. In particular, we will analyze the local stability of the spatially homogeneous steady states. In Chapter 5, we will investigate numerically the spatial and spatiotemporal patterns displayed by system (2.1). We conclude the analysis of this model in Chapter 6, when we will perform a nonlocal analysis of these patterns.

Chapter 3

Theoretical aspects regarding the hyperbolic model

3.1 Introduction

In this chapter, we focus on some analytical results for the new hyperbolic system we introduced in Chapter 2. In Section 3.2, we present an existence result for the mild solutions of system (2.1). This result will be particularly useful in Chapter 6, when we analyze analytically some of the spatial and spatiotemporal patterns of this system. In the mathematical literature, there are results regarding the existence and uniqueness of solutions for hyperbolic systems of the form (2.1), with local turning rates defined as $\lambda^+(u^+, u^-) = \lambda^-(u^-, u^+)$ (see [69]), or $\lambda^\pm = \lambda^\pm(S, S_x)$, where S is an external stimulus that depends on $u^\pm$ (see [55]). In contrast to these cases, the model introduced in the previous chapter has nonlocal turning rates. This requires a more careful discussion of the nonlocal terms.

In Section 3.3, the focus will be on the reduction of the hyperbolic model (2.1) to a well known nonlocal parabolic equation introduced by Mogilner and Edelstein-Keshet [80]. The parabolic equation described in [80] has generated a lot of interest in these past years (see equations (1.2)-(1.4) and the corresponding discussion in Chapter 1). The reason for this is that the model displays biologically realistic groups, with well defined boundaries and a constant interior density. We will show that when the speed becomes very large and the

individuals turn very frequently, system (2.1) formally reduces to an equation similar to (1.2)-(1.4). In this case, the convective movement is the result of the difference between the right and the left turning rates. However, compared to (1.2)-(1.4), our limiting equation does not have a local drift term. We will argue that because of this, the groups do not move. We will address this issue by showing that an asymmetry in the signal reception (caused, for example, by some environmental factors) induces a small nonlocal drift in the velocity of the limiting parabolic equation. This drift can lead to group movement.

We conclude with a discussion in Section 3.4.

3.2 Existence of mild solutions

In this section, we discuss the existence of solutions of system (2.1). For this, we assume that the turning rates (equations (2.2)) are continuously differentiable functions of the signals $y^{\pm}$. This implies that they are uniform continuous functions of $y^{\pm}$. Note that this assumption was necessary in Chapter 2, when we derived system (2.1) using a correlated random walk approach. Moreover, the turning function we will consider in the following chapters, namely the function defined by equations (2.2)-(2.4), satisfies this assumption. Also, to make things easier, we assume that the nonlocal interactions are described by equations (2.5), (2.7), and (2.8). The other cases can be dealt with in a similar manner.

For this hyperbolic system, the characteristic equations are

$$\frac{d\zeta^+}{ds} = \gamma, \qquad \frac{d\zeta^-}{ds} = -\gamma. \tag{3.1}$$

Let $\zeta^{\pm} = \Xi^{\pm}(s;x,t)$ be the solution of this differential system, passing through the point (x,t). If we set $U^{\pm}(s) = u(\Xi^{\pm}(s;x,t),s)$, we can rewrite the hyperbolic system (2.1) as

$$\begin{aligned}
\frac{dU^+}{dt}(s;x,t) &= -\lambda^+[U^+(s),U^-(s)]U^+(s) + \lambda^-[U^+(s),U^-(s)]U^-(s), \\
\frac{dU^-}{dt}(s;x,t) &= \lambda^+[U^+(s),U^-(s)]U^+(s) - \lambda^-[U^+(s),U^-(s)]U^-(s).
\end{aligned} \tag{3.2}$$

Integrating (3.2) along the characteristics gives

$$U^+(\zeta^+) = U^+(\zeta_0) + \int_{\zeta_0}^{\zeta^+} \left(-\lambda^+[U^+,U^-]U^+ + \lambda^+[U^+,U^-]U^-\right)(y)dy \quad (3.3)$$

$$U^-(\zeta^-) = U^-(\zeta_0) + \int_{\zeta_0}^{\zeta^-} \left(\lambda^+[U^+,U^-]U^+ - \lambda^-[U^+,U^-]U^-\right)(y)dy. \quad (3.4)$$

Note that a pair of functions $(u^+(x,t), u^-(x,t)) \in L^\infty\left(\mathbf{R}\times[0,t_0)\right)$ which satisfies equations (3.3)-(3.4) is called a *mild solution* of system (2.1).

Theorem 3.2.1. *Let us assume that the initial data is $u_0^\pm \in L^\infty(\mathbf{R})$, the turning rates are continuously differentiable as functions of the signals $y^\pm$, and the kernels $K_j \in L^1(\mathbf{R})$, $j = a, r, al$. Then there exists a unique mild solution $u^\pm \in L^\infty\left(\mathbf{R}\times[0,t_0)\right)$ of system (2.1), for some $t_0 > 0$. Moreover, the solution exists on $L^\infty\left(\mathbf{R}\times[0,\infty)\right)$, which implies global existence.*

Proof: To prove this existence result, we define the operator $G(U^+,U^-) = (G_1(U^+,U^-), G_2(U^+,U^-))$, where G_1 and G_2 are described by the two expressions on the right hand side of equations (3.3), and (3.4), respectively. Then, finding a unique mild solution of (2.1), reduces to finding a fixed point of the map $(U^+,U^-) \mapsto G(U^+,U^-)$.

Let us consider the Banach spaces $X := L^\infty(\mathbf{R}\times[0,t_0))$ with norm $\|u\|_X := \sup\|u(\cdot,t)\|_\infty$, and $\bar{X} := L^\infty(\mathbf{R})$. On $X\times X$ we have the norm $\|(u,v)\|_{X\times X} := \max(\|u\|_X, \|v\|_X)$. We also define $B = B(R,X) := \{u \in X : \|u(x,t)\|_X \le R\}$. Following the same steps as in [55, 69], for all $\omega \in X$ with $\omega^\pm(0,\cdot) = u_0^\pm \in L^\infty(\mathbf{R})$, we consider the following Cauchy problem

$$\begin{aligned} u_t^+ + \gamma u_x^+ &= -\lambda^+[\omega^+,\omega^-]\omega^+ + \lambda^-[\omega^+,\omega^-]\omega^-, \\ u_t^- - \gamma u_x^- &= \lambda^+[\omega^+,\omega^-]\omega^+ - \lambda^-[\omega^+,\omega^-]\omega^-, \\ u^\pm(0,x) &= u_0^\pm(x). \end{aligned} \quad (3.5)$$

This problem can be solved along the characteristics (3.1), with respect to the new variables $\zeta^\pm$. For this, we prove that the operator $G(\omega^+,\omega^-)$ defined by equations (3.3)–(3.4) is a contraction:

1. $G : X_R \times X_R \mapsto X_R \times X_R$ (where X_R is a closed subset of Banach space X)

2. For (ω^+, ω^-), $(\theta^+, \theta^-) \in X_R \times X_R$:

$$\|G(\omega^+, \omega^-) - G(\theta^+, \theta^-)\|_{X_R \times X_R} \leq \epsilon \|(\omega^+, \omega^-) - (\theta^+, \theta^-)\|_{X_R \times X_R}.$$

To prove that G maps a closed subset of a Banach space into itself, we only have to assume that $u_0^{\pm}$ is bounded in $\|.\|_{X_R}$ by a constant M^*. We then choose $R \geq M^* + \epsilon_1$, for some $\epsilon_1 > 0$. For $(\omega^+, \omega^-) \in B$, with $\omega^{\pm}(0, \cdot) = U_0^{\pm}$, we have

$$\begin{aligned}
\|G_1(\omega^+, \omega^-)\|_X &\leq \|U_0^{\pm}\|_{\bar{X}} + \int_{\zeta_0}^{\zeta^+} \| \left(-\lambda^+[\omega^+, \omega^-]\omega^+ + \lambda^-[\omega^+, \omega^-]\omega^-\right)(y,t)\|_X dy \\
&\leq M + \left|\zeta^+ - \zeta_0\right| \left(\sup_B \lambda_+[\omega^+, \omega^-]\|\omega^+\|_X \right. \\
&+ \left. \sup_B \lambda_-[\omega^+, \omega^-]\|\omega^-\|_X\right) \\
&\leq M^* + \gamma t_0 R \left(\sup_B \lambda^+[\omega^+, \omega^-] + \sup_B \lambda^-[\omega^+, \omega^-]\right).
\end{aligned}$$

In Chapter 2, we assumed that the turning rates $\lambda^{\pm}$ are bounded functionals. Let us then define $K = \sup_B \lambda^+(\omega^+, \omega^-) + \sup_B \lambda^-(\omega^+, \omega^-)$, and choose $t_0 \leq \frac{\epsilon_1}{\gamma R K} = T_1$. This way, we obtain the bound $\|G_1(\omega^+, \omega^-)\|_X \leq M^* + \epsilon_1 \leq R$. A similar result holds for G_2.

To prove the contraction condition, consider (ω^+, ω^-), $(\theta^+, \theta^-) \in B$, with $\omega^{\pm}(0, \cdot) = \theta^{\pm}(0, \cdot) = U_0^{\pm}$. Then,

$$\begin{aligned}
&\|G_1(\omega^+, \omega^-) - G_1(\theta^+, \theta^-)\|_{X \times X} = \| \int_{\zeta_0}^{\zeta^+} \left(\lambda^+[\theta^+, \theta^-]\theta^+ - \lambda^+[\omega^+, \omega^-]\omega^+ \right. \\
&\quad \left. + \lambda^-[\omega^+, \omega^-]\omega^- - \lambda^-[\theta^+, \theta^-]\theta^-\right)(y,t)dy\|_X \\
&= \frac{1}{2}\| - \int_{\zeta_0}^{\zeta^+} \left(\lambda^+[\omega^+, \omega^-] + \lambda^+[\theta^+, \theta^-]\right)(\omega^+ - \theta^+)(y,t)dy \\
&+ \int_{\zeta_0}^{\zeta^+} \left(\lambda^-[\omega^+, \omega^-] + \lambda^-[\theta^+, \theta^-]\right)(\omega^- - \theta^-)(y,t)dy \\
&+ \int_{\zeta_0}^{\zeta^+} \left(\lambda^+[\theta^+, \theta^-] - \lambda^+[\omega^+, \omega^-]\right)(\omega^+ + \theta^+)(y,t)dy \\
&- \int_{\zeta_0}^{\zeta^+} \left(\lambda^-[\theta^+, \theta^-] - \lambda^-[\omega^+, \omega^-]\right)(\omega^- + \theta^-)(y,t)dy\|_X .
\end{aligned} \tag{3.6}$$

We assumed that the turning rates are continuously differentiable functions of the perceived signals $y^{\pm}$. Therefore, they are locally Lipschitz continuous as functions of $y^{\pm}$. Let $L^{\pm}$ be the Lipschitz constants. Using equations (2.2), we obtain

$$\begin{aligned}
&\|\lambda^{\pm}[\omega^+,\omega^-]-\lambda^{\pm}[\theta^+,\theta^-]\|_{X\times X}=\|f(y^{\pm}[\omega^+,\omega^-])-f(y^{\pm}[\theta^+,\theta^-])\|_{X\times X}\\
\leq\;& L^{\pm}(R)\|y^{\pm}[\omega^+,\omega^-]-y^{\pm}[\theta^+,\theta^-]\|_{X\times X}\\
=\;& L^{\pm}(R)\|\int_0^{\infty}(\pm q_rK_r(s)\mp q_aK_a(s))\,(\omega(x\pm s,t)-\theta(x\pm s,t)-\omega(x\mp s,t)\\
+\;& \theta(x\mp s,t))\,ds\pm\int_0^{\infty}q_{al}K_{al}(s)\left(\omega^-(x+s,t)-\theta^-(x+s,t)-\omega^+(x-s)\right.\\
+\;& \left.\theta^+(x-s)\right)\,ds\|_X\\
\leq\;& L_{1,2}(R)\max(\|\omega^+-\theta^+\|_X,\|\omega^--\theta^-\|_X)\\
=\;& L_{1,2}(R)\|(\omega^+,\omega^-)-(\theta^+,\theta^-)\|_{X\times X}. \qquad (3.7)
\end{aligned}$$

Here $L_{1,2}(R)=L^{\pm}(R)C(q_r,q_a,q_{al})$, where $C(q_r,q_a,q_{al})$ is a constant that depends on the magnitudes of the social interactions. Hence, $\lambda^{\pm}$ are locally Lipschitz continuous as functions of $\omega^{\pm},\theta^{\pm}$, with $L_1(R)$ and $L_2(R)$ the Lipschitz constants. We therefore have

$$\begin{aligned}
&\|G_1(\omega^+,\omega^-)-G_1(\theta^+,\theta^-)\|_{X\times X}\leq\frac{1}{2}\left|\zeta^+-\zeta_0\right|2\sup_B\lambda^+(\omega^+,\omega^-)\|\omega^+-\theta^+\|_X\\
&+\frac{1}{2}\left|\zeta^+-\zeta_0\right|2\sup_B\lambda^-(\omega^+,\omega^-)\|\omega^--\theta^-\|_X\\
&+\frac{1}{2}\left|\zeta^+-\zeta_0\right|\|\omega^++\theta^+\|_XL_1(R)\max(\|\theta^+-\omega^+\|_X,\|\theta^--\omega^-\|_X)\\
&+\frac{1}{2}\left|\zeta^+-\zeta_0\right|\|\omega^-+\theta^-\|_XL_2(R)\max(\|\theta^+-\omega^+\|_X,\|\theta^--\omega^-\|_X). \qquad (3.8)
\end{aligned}$$

Since $\|\omega^{\pm}+\theta^{\pm}\|_X\leq 2R$, we obtain

$$\begin{aligned}
\|G_1(\omega^+,\omega^-)-G_1(\theta^+,\theta^-)\|_{X\times X}\quad&\leq\gamma t_0\,(K+L_1(R)R\\
&+\quad L_2(R)R)\,\|(\omega^+,\omega^-)-(\theta^+,\theta^-)\|_{X\times X}. \qquad (3.9)
\end{aligned}$$

Let us define $T_2=\frac{\epsilon_2}{\gamma(K+L_1(R)R+L_2(R)R)}$, for some $\epsilon_2>0$, and choose $t_0\leq T_2$. We then obtain

$$\|G_1(\omega^+,\omega^-)-G_1(\theta^+,\theta^-)\|_{X\times X}\leq\epsilon_2\|(\omega^+,\omega^-)-(\theta^+,\theta^-)\|_{X\times X}.$$

A similar estimate holds for G_2. Then, for $t_0 \le \min(T_1, T_2)$ we have

$$\|G(\omega^+, \omega^-) - G(\theta^+, \theta^-)\|_{X\times X} \le \epsilon \|(\omega^+, \omega^-) - (\theta^+, \theta^-)\|_{X\times X}, \tag{3.10}$$

which implies that G is a contraction. Therefore, G has a unique fixed point $(u^+, u^-) \in X \times X$. Replacing $\omega^\pm$ in (3.3)–(3.4) with $U^\pm$, results in:

$$\begin{aligned}
\|U^+(\zeta^+)\|_X &\le \|U^+(\zeta_0)\|_{\bar X} + \| \int_{\zeta_0}^{\zeta^+} \left(-\lambda^+[U^+, U^-]U^+ + \lambda^-[U^+, U^-]U^-\right)(y)dy\|_X, \\
\|U^-(\zeta^-)\|_X &\le \|U^-(\zeta_0)\|_{\bar X} + \| \int_{\zeta_0}^{\zeta^-} \left(\lambda^+[U^+, U^-]U^+ - \lambda^-[U^+, U^-]U^-\right)(y)dy\|_X,
\end{aligned}$$

and therefore

$$\begin{aligned}
\|U^+\|_X + \|U^-\|_X \le \|u_0^+\|_{\bar X} + \|u_0^-\|_{\bar X} &+ 2\gamma t_0 \left(K + (L_1(R) + L_2(R))R\right)\left(\|U^+\|_X + \right. \\
&\left. + \|U^-\|_X\right). \qquad (3.11)
\end{aligned}$$

Hence

$$\|U^+\|_X + \|U^-\|_X \le \frac{1}{1-\epsilon}(\|U_0^+\|_{\bar X} + \|U_0^-\|_{\bar X}), \tag{3.12}$$

which implies that $u^\pm \in L^\infty(\mathbf{R} \times [0, t_0\ ))$.

To prove that the solution is defined for all time, it is enough to show that $\|U^\pm\|_X$ are bounded on any bounded interval $[0, T]$:

$$\begin{aligned}
\frac{d}{ds}\|U^\pm(s,\cdot)\|_{L^\infty(\mathbf{R})} &\le \|\frac{d}{ds}U^\pm(s,\cdot)\|_{L^\infty(\mathbf{R})} \\
&\le \|\lambda^+(U^+, U^-)U^+\|_{L^\infty(\mathbf{R})} + \|\lambda^-(U^+, U^-)U^-\|_{L^\infty(\mathbf{R})} \\
&\le M_2(\|U^+\|_{L^\infty(\mathbf{R})} + \|U^-\|_{L^\infty(\mathbf{R})}), \qquad (3.13)
\end{aligned}$$

where M_2 is the upper bound for $\lambda^\pm$. Therefore

$$\|U^+\|_{L^\infty(\mathbf{R})} + \|U^-\|_{L^\infty(\mathbf{R})} \le (\|U_0^+\|_{L^\infty(\mathbf{R})} + \|U_0^-\|_{L^\infty(\mathbf{R})})e^{M_2 s}. \tag{3.14}$$

Since $U^\pm(t,\cdot)$ are bounded on any bounded interval $[0, T]$, the solution exists for all time. ♣

Note that since $\frac{d}{dt}\int_{-\infty}^{\infty}(u^+(x,t)+u^-(x,t))dx = 0$ it follows that if the initial condition satisfies $u_0^{\pm} \in L^1(\mathbf{R})$, then $u^{\pm} \in L^1(\mathbf{R})$.

Throughout chapters 4 to 6, we will investigate analytically and numerically some of the patterns displayed by system (2.1) when we consider a finite domain with periodic boundary conditions. In this context, it can be proved that if the initial data $u_0^{\pm}(x)$ is periodic, then the mild solution $u^{\pm}$ is periodic.

Theorem 3.2.2. *Consider the bounded domain $\Omega = [0, L]$. If $u_0^{\pm} \in L^{\infty}(\Omega)$, the turning rates are uniform continuous as functions of the signals $y^{\pm}$, and the kernels $K_j \in L^1(\Omega)$, $j = a, r, al$, then there exists a unique mild solution $u^{\pm} \in L^{\infty}(\Omega \times [0,\infty))$ of system (2.1).*

Proof: Let us extend the initial data $u_0^{\pm}$ by periodicity to the entire real line: $\bar{u}_0^{\pm}(x) = u_0^{\pm}(x \mod L)$, with $x \in \mathbf{R}$. Using the previous theorem, there exists a unique solution $\bar{u}^{\pm} \in L^{\infty}(\Omega \times [0,\infty))$ of system (2.1). Let us now define $w^{\pm}(x,t) = \bar{u}^{\pm}(x+L,t)$. Then, $w^{\pm}$ is also a solution of system (2.1). For example, for w^+ we have

$$\begin{aligned} w_t^+(x,t) + \gamma w_x^+(x,t) &= \bar{u}_t^+(x+L,t) + \gamma \bar{u}_x^+(x+L,t) \\ &= -\bar{u}^+(x+L,t)\lambda^+[\bar{u}^+(x+L,t), \bar{u}^-(x+L,t)] \\ &+ \bar{u}^-(x+L,t)\lambda^-[\bar{u}^+(x+L,t), \bar{u}^-(x+L,t)]. \end{aligned} \tag{3.15}$$

Note that, since

$$\begin{aligned} &\int_0^{\infty} K_j(s)\left(\bar{u}(x+L+s,t) - \bar{u}(x+L-s,t)\right) ds \\ &= \int_0^{\infty} K_j(s)\left(w(x+s,t) - w(x-s,t)\right) ds, \quad j = r, a, \quad \textbf{where } w = w^+ + w^-, \\ &\text{and} \\ &\int_0^{\infty} K_{al}(s)\left(\bar{u}^-(x+L+s,t) - \bar{u}^+(x+L-s,t)\right) ds \\ &= \int_0^{\infty} K_{al}(s)\left(w^-(x+s,t) - w^+(x-s,t)\right) ds, \end{aligned} \tag{3.16}$$

we actually obtain

$$\lambda^{\pm}[\bar{u}^{+}(x+L,t),\bar{u}^{-}(x+L,t)] = \lambda^{\pm}[w^{+}(x,t),w^{-}(x,t)]. \tag{3.17}$$

Therefore,

$$w_t^{+}(x,t)+\gamma w_x^{+}(x,t) = -w^{+}(x,t)\lambda^{+}[w^{+}(x,t),w^{-}(x,t)]+w^{-}(x,t)\lambda^{-}[w^{+}(x,t),w^{-}(x,t)], \tag{3.18}$$

and hence w^{+} is a solution of system (2.1) with the initial condition $w^{+}(x,0) = \bar{u}^{+}(x+L,0) = \bar{u}^{+}(x,0)$. A similar result holds for w^{-}. Uniqueness of solutions on R implies that the solution $\bar{u}^{\pm}(x,t)$ is periodic. Therefore, it can be restricted to Ω with periodic boundary conditions.♣

There are two remarks in regard to the semi-linear system (2.1):

1. First, we should note that if the initial data $u_0^{\pm}$ is continuous, then the mild solution of system (2.1) is a continuous function (see [14]).

2. As a result of Theorem 3.2.1, since the right-hand side of system (2.1) satisfies a bound of the form

$$|-u^{+}\lambda^{+}[u^{+},u^{-}]+u^{-}\lambda^{-}[u^{+},u^{-}]| \leq C(|u^{+}|+|u^{-}|), \tag{3.19}$$

then the solution $(u^{+}(\cdot,t),u^{-}(\cdot,t))$ will remain bounded for all $t \geq 0$. Since the system (2.1) is semi-linear, as long as the solution is bounded, its gradient remains bounded [14].

All these results will be useful later, in Chapters 5 and 6, when we will investigate numerically and analytically the solutions of system (2.1). In particular, these results ensure that the solutions will be continuous, and will not blow up.

3.3 Formal parabolic limit

In this section, we focus on the reduction of the hyperbolic model (2.1) to the parabolic equation (1.2)-(1.4) introduced in [80]. Recall that this parabolic

model assumes only attractive and repulsive interactions. For this reason, we also focus only on these two interactions (i.e., $q_r, q_a \neq 0$, and $q_{al} = 0$). At the end of this section we will briefly discuss the case when alignment is nonzero. Throughout this section, we focus on the model introduced in Section 2.2. There, we assumed that the these interactions depend on the information that comes from all neighbors (Figure 2.3), so that the interactions are defined in terms of $u = u^+ + u^-$. Because of this, we can rewrite the signals received from right- and left-moving individuals as $y^{\pm}[u^+, u^-] = y^{\pm}[u]$ (see equations (2.2)-(2.3)). Moreover, to compare our results with other results existent in the literature (see [80]), we use kernels defined by equations (2.11).

Let us rewrite the turning rates

$$\begin{aligned} \Lambda^+[u] &:= \lambda^+[u^+, u^-] = \lambda_1 + \lambda_2 f(y^+[u]), \\ \Lambda^-[u] &:= \lambda^-[u^+, u^-] = \lambda_1 + \lambda_2 f(y^-[u]). \end{aligned} \tag{3.20}$$

Adding and subtracting the first two equations of system (2.1), leads to

$$\begin{aligned} (u^+ + u^-)_t + \gamma(u^+ - u^-)_x &= 0, \\ (u^+ - u^-)_t + \gamma(u^+ + u^-)_x &= -2u^+\Lambda^+[u] + 2u^-\Lambda^-[u]. \end{aligned} \tag{3.21}$$

Define $v = u^+ - u^-$, $\alpha[u] = \Lambda^-[u] - \Lambda^+[u]$, and $\beta[u] = \Lambda^-[u] + \Lambda^+[u]$. System (3.21) can thus be rewritten as

$$u_t + \gamma v_x = 0, \tag{3.22}$$

$$v_t + \gamma u_x = u\alpha[u] - v\beta[u]. \tag{3.23}$$

Differentiating equation (3.22) with respect to t and equation (3.23) with respect to x, assuming zero flow at the boundaries, and taking into account that $v = -\frac{1}{\gamma}\int^x \partial_t u$ (from (3.22)), leads to the following hyperbolic equation

$$\gamma^2 u_{xx} = u_{tt} + \gamma(u\alpha[u])_x + \beta[u]u_t + (\beta[u])_x \int^x \partial_t[u]. \tag{3.24}$$

To transform this equation into a parabolic equation, one can scale the speed and the turning rates, or equivalently, scale the space and the time [53]. We focus here on the first approach, and assume that the speed as well as the

turning rates become very large. Note that, in this case, we have to scale not only the random turning rate, but also the directed turning rate. In the following, we introduce a new dimensionless parameter $\epsilon > 0$, and consider the following parameter scaling:

$$\begin{aligned} &(a) \quad \lambda_1 = \frac{\lambda_1^0}{\epsilon^2},\ \lambda_2 = \frac{\lambda_2^0}{\epsilon^2}; \\ &(b) \quad \gamma = \frac{\gamma_0}{\epsilon}; \\ &(c) \quad f(y^{\pm}[u]) = \epsilon f^0(y^{\pm}[u]). \end{aligned} \tag{3.25}$$

We let $\epsilon \to 0$ in such a way that

$$\frac{(\gamma_0)^2}{2\lambda_1^0} \;=\; D, \;\text{ and }\; \frac{\gamma_0 \lambda_2^0}{2\lambda_1^0} = B. \tag{3.26}$$

Here D and B are constants. This scaling means that when $\epsilon \to 0$, (a) the individuals turn very frequently, (b) move very fast, and (c) the previous two behaviors result in a reduced sensitivity to the environment. Let

$$\alpha[u] = \frac{\lambda_2^0 \alpha^0[u]}{\epsilon}, \quad \text{with } \alpha^0[u] = f^0(y^-[u]) - f^0(y^+[u]), \tag{3.27}$$

and

$$\beta[u] = \frac{2\lambda_1^0}{\epsilon^2} + \frac{2\lambda_2^0 \beta^0[u]}{\epsilon}, \;\text{ with } \beta^0[u] = f^0(y^-[u]) + f^0(y^+[u]). \tag{3.28}$$

Equation (3.24) now reads

$$\frac{\gamma_0^2}{\epsilon^2} u_{xx} = u_{tt} + \frac{\lambda_2^0 \gamma_0}{\epsilon^2}(u\alpha^0[u])_x + \left(\frac{2\lambda_1^0}{\epsilon^2} + \frac{2\lambda_2^0 \beta^0[u]}{\epsilon}\right) u_t + \frac{(2\lambda_2^0 \beta^0[u])_x}{\epsilon} \int^x u_t dx. \tag{3.29}$$

After multiplying with ϵ^2 and taking the formal limit $\epsilon \to 0$, we obtain the parabolic equation

$$u_t = D u_{xx} - B(u\alpha^0[u])_x. \tag{3.30}$$

The diffusion coefficient D and the advection coefficient B are given by (3.26). Note that the diffusion is constant, while the advection is the result of the difference between the nonlocal right (λ^+) and left (λ^-) turning rates. This is caused by $\alpha^0[u]$ which, in expanded form, can be written as

$$\begin{aligned} \alpha^0[u] \;&=\; -f\left(q_r \int_{-\infty}^{\infty} K_r(s) u(x+s,t) ds - q_a \int_{-\infty}^{\infty} K_a(s) u(x+s,t) ds\right) \\ &+\; f\left(-q_r \int_{-\infty}^{\infty} K_r(s) u(x+s,t) ds + q_a \int_{-\infty}^{\infty} K_a(s) u(x+s,t) ds\right) \end{aligned} \tag{3.31}$$

A similar result could have been obtained rescaling the time and the space (as in [53]).

Equation (3.30) is quite similar to parabolic equation (1.2)-(1.4), introduced by Mogilner and Edelstein-Keshet [80] to study the formation and movement of animal groups. However, compared to (1.2)-(1.4), equation (3.30) does not contain a local drift term. This suggests that (3.30) will not support traveling pulses, since the nonlocal odd kernel (2.11) cannot make the group move (see the discussion in [80]).

Note that the velocity term $\alpha^0[u]$ is a nonlinear function of the nonlocal interactions. However, to simplify the analysis, the majority of the results existent in the literature consider a linear dependence on the social interactions (see for example, [67], [78], [80], [122], [123]). This can be addressed if we assume that the repulsive and attractive interactions balance each other, that is, $f(y^{\pm}[u]) \approx f(0)$. In this case, we can linearize the nonlocal term $\alpha^0[u]$, and keep only the first approximation, namely

$$\alpha^0[u] \approx -2f^{0\prime}(0)\left(q_r\int_{-\infty}^{\infty}K_r(s)u(x+s,t)ds - q_a\int_{-\infty}^{\infty}K_a(s)u(x+s,t)ds\right). \tag{3.32}$$

We assume here that $f^{0\prime}(0) \neq 0$. Then, equation (3.30) can be written as

$$\partial_t u = D\partial_x^2 u + B\partial_x\left(u\left(q_r\int_{-\infty}^{\infty}(K_r(s)u(x+s,t)ds) - q_a\int_{-\infty}^{\infty}(K_a(s)u(x+s,t)ds)\right)\right), \tag{3.33}$$

where the diffusion coefficient D is given as before, while the advection coefficient is $B = \frac{2\gamma_0\lambda_2^0 f^{0\prime}(0)}{\lambda_1^0}$.

Therefore, in the absence of alignment, we can formally derive the parabolic model (1.2)-(1.4) from the hyperbolic system (2.1). Hence, when the speed and the turning rates are very large, two different biological assumptions, namely (i) velocity described in terms of attractive and repulsive interactions (as in [80]), and (ii) turning rates described in terms of attractive and repulsive interactions (this hyperbolic model), lead to similar behavior.

The relationship between the parabolic model (1.2)-(1.4) and the hyperbolic model (2.1) can be investigated not only through the parabolic limit, but also through the steady state equations. For the rest of the chapter, we

return to the more general parabolic equation (3.30). Note that the stationary pulses of this equation coincide with the stationary pulses of the hyperbolic system (2.1) when attraction and repulsion are the only social interactions. More precisely, for the parabolic equation (3.30), the zero-flux heterogeneous steady-state solution that satisfies $u(\pm\infty) = 0$ is described by

$$u_x = \frac{B}{D} u \alpha^0[u]. \tag{3.34}$$

On the other hand, the steady-state equations for the hyperbolic system (2.1) are

$$\gamma u_x^+ = -u^+ \left(\lambda_1 + \lambda_2 f(y^+[u])\right) + u^- \left(\lambda_1 + \lambda_2 f(y^-[u])\right), \tag{3.35}$$

$$-\gamma u_x^- = u^+ \left(\lambda_1 + \lambda_2 f(y^+[u])\right) - u^- \left(\lambda_1 + \lambda_2 f(y^-[u])\right). \tag{3.36}$$

Therefore, $u_x^+ = u_x^-$. When there is no flow at the boundaries, that is when $u^+(\pm\infty) - u^-(\pm\infty) = 0$, we obtain $u^+ = u^-$. In this case, equations (3.35)-(3.36) are reduced to

$$\gamma u_x^+ = -u^+ \lambda_2 \left(f(y^+[u]) - f(y^-[u])\right), \tag{3.37}$$

which is exactly the equation (3.34). Hence, the stationary pulses of limiting parabolic equation (3.30) coincide with the stationary pulses of hyperbolic system (2.1).

Recall that in the above treatment, alignment was absent. When alignment influences the turning rates, a formal parabolic limit cannot be obtained. In this case, the alignment term depends on the flux $v = u^+ - u^-$. However, there is no second equation for v. An eventual substitution for $v = \int^x u_t(s,t)ds$ leads to an equation similar to (3.30), with u_t defined implicitly ($\alpha^0[u] := \bar{\alpha}^0[u, u_t]$), although this is not a classic parabolic equation.

During the rescaling process we assumed that the random and directed turning rates approach infinity with the same speed, that is $\lambda_1 = \frac{\lambda_1^0}{\epsilon^2}$, and $\lambda_2 = \frac{\lambda_2^0}{\epsilon^2}$. However, one can assume that the individuals turn more often as a response to external stimuli than they turn randomly, that is $\lambda_1 = \frac{\lambda_1^0}{\epsilon}$, and $\lambda_2 = \frac{\lambda_2^0}{\epsilon^2}$. In this case, the term $\beta[u]$ changes slightly:

$$\beta[u] = \frac{2\lambda_1^0}{\epsilon} + \frac{2\lambda_2^0 \beta^0[u]}{\epsilon}. \tag{3.38}$$

As $\epsilon \to 0$, the hyperbolic equation (3.24) reduces to the following elliptic equation

$$u_{xx} = \frac{1}{\gamma_0 \lambda_2^0}(u\alpha^0[u])_x. \tag{3.39}$$

If, on the other hand, we assume that the random turning dominates the motion, that is $\lambda_1 = \frac{\lambda_1^0}{\epsilon^2}$ and $\lambda_2 = \frac{\lambda_2^0}{\epsilon}$, we obtain the diffusion equation

$$u_t = \frac{\gamma_0^2}{2\lambda_1^0} u_{xx}. \tag{3.40}$$

Therefore, different scaling for the directed and random turning rates leads to either parabolic or elliptic equations. A similar result has been obtained when considering different time scales [53]. For this case, it has been shown that the parabolic equation arises on a slow time scale, while the elliptic equation arises on a fast time scale.

3.3.1 Formal parabolic limit with a drift term

As previously mentioned, equation (3.30) does not contain a local drift term. The nonlocal odd kernels alone cannot make the group move, since individuals at the front and at the rear edge move towards the center of the group [80]. Therefore, equation (3.30) might not support traveling pulses. However, in Chapter 2, we have seen that it is possible to introduce environmental drift by considering asymmetry in the communication mechanism (see equations (2.5)-(2.8), where $p_r \neq p_l$). In this case, the nonlocal attractive and repulsive interactions can be rewritten as

$$\begin{aligned} &q_{r,a} \int_0^\infty K_{r,a}(s) \left(p_r u(x+s,t) - p_l u(x-s,t)\right) ds = \\ &q_{r,a} p_r \int_{-\infty}^\infty K_{r,a}(s) u(x+s,t) ds + q_{r,a}(p_r - p_l) \int_0^\infty K_{r,a} u(x-s,t) ds. \end{aligned} \tag{3.41}$$

Let $q_{r,a}^* = q_{r,a} p_r$ and drop the asterisk. Then, equation (3.30) reduces to

$$\begin{aligned} u_t \;=\; & D u_{xx} - B \left(-uf \left(\int_{-\infty}^\infty K(s) u(x+s,t) ds + (p_r - p_l) \int_0^\infty K(s) u(x-s,t) ds \right) + \right. \\ & \left. uf \left(- \int_{-\infty}^\infty K(s) u(x+s,t) ds - (p_r - p_l) \int_0^\infty K(s) u(x-s,t) ds \right) \right)_x, \end{aligned} \tag{3.42}$$

where $K(s) = q_r K_r(s) - q_a K_a(s)$. Here we consider $p_r - p_l \ll 1$. Therefore, the nonlocal term $(p_r - p_l)\int_0^\infty K(s)u(x-s,t)ds$ can be seen as a small drift. To show that this drift can make the group move, we follow the approach proposed in [80]. In particular, let us assume that there exists a rectangular group of width L_0 and density A. In Chapter 2, we assumed that the interaction kernels $K_{r,a}(s)$ have the support inside the interval $[0,\infty)$. These kernels can actually be approximated by kernels with the support inside the interval $[0, 6j)$, $j = s_{r,a}$. We will discuss this approximation in more detail in Chapter 5. Note that the attractive and repulsive kernels (2.11) satisfy

$$\int_0^{6s_r} K_r(s)ds = 1, \quad \int_0^{6s_a} K_a(s)ds = 1. \tag{3.43}$$

Therefore, the odd kernel K will satisfy

$$\int_0^{6s_a} K(s)ds = -(q_a - q_r), \quad \text{and} \quad \int_{-6s_a}^0 K(s)ds = (q_a - q_r). \tag{3.44}$$

Note that if the kernel K would be even, both integrals in (3.44) would be positive. We will come back to this result at the end of this section. An individual positioned at the front edge of the group (that is, at $x = L_0$), and that can sense its neighbors up to a distance $6s_a$ (where $6s_a < L_0$), will have a velocity

$$\begin{aligned} V_f &= -u(x,t)f\left(\int_{-6s_a}^{6s_a} K(s)u(x+s,t)ds + (p_r - p_l)\int_0^{6s_a} K(s)u(x-s,t)ds\right) + \\ &\quad u(x,t)f\left(-\int_{-6s_a}^{6s_a} K(s)u(x+s,t)ds - (p_r - p_l)\int_0^{6s_a} K(s)u(x-s,t)ds\right) \\ &= -u(x,t)f\left(\int_{x-6s_a}^{x+6s_a} K(y-x)u(y,t)dy + (p_r - p_l)\int_{x-6s_a}^{x} K(x-y)u(y,t)dy\right) + \\ &\quad u(x,t)f\left(-\int_{x-6s_a}^{x+6s_a} K(y-x)u(y,t)dy - (p_r - p_l)\int_{x-6s_a}^{x} K(x-y)u(y,t)dy\right). \end{aligned}$$

When $x = L_0$, there are no individuals inside the interval $(L_0, L_0 + 6s_a)$. Since the group density is $u(L_0,t) = A$, we obtain

$$
\begin{aligned}
V_f &= -Af\left(A\int_{L_0-6s_a}^{L_0} K(y-L_0)dy + A(p_r-p_l)\int_{L_0-6s_a}^{L_0} K(L_0-y)dy\right) + \\
&\quad Af\left(-A\int_{L_0-6s_a}^{L_0} K(y-L_0)dy - A(p_r-p_l)\int_{L_0-6s_a}^{L_0} K(L_0-y)dy\right) \\
&= -Af\left(A\int_{-6s_a}^{0} K(z)dz + A(p_r-p_l)\int_{0}^{6s_a} K(z)dz\right) + \\
&\quad Af\left(-A\int_{-6s_a}^{0} K(z)dz - A(p_r-p_l)\int_{0}^{6s_a} K(z)dz\right) \\
&= -Af\left(A(q_a-q_r)\left(1-(p_r-p_l)\right)\right) + Af\left(-A(q_a-q_r)\left(1-(p_r-p_l)\right)\right).
\end{aligned}
\tag{3.45}
$$

Similarly, one can calculate the speed of an individual positioned at the back edge ($x = L_0$). Note that in this case there are no individuals inside the interval $(L_0 - 6s_a, L_0)$, and hence, the second integral vanishes:

$$
\begin{aligned}
V_b &= -Af\left(A\int_{L_0}^{L_0+6s_a} K(y-L_0)dy\right) + Af\left(-A\int_{L_0}^{L_0+6s_a} K(y-L_0)dy\right) \\
&= -Af\left(-A(q_a-q_r)\right) + Af\left(A(q_a-q_r)\right).
\end{aligned}
\tag{3.46}
$$

We observe that for $p_r = p_l$, we obtain

$$
V_f = -Af\left(A(q_a-q_r)\right) + Af\left(-A(q_a-q_r)\right) = -V_b. \tag{3.47}
$$

In this case, the individuals at the front and the back edge of the group move with opposite velocities. In Chapter 2, we assumed that f is a positive, bounded, and increasing function. Therefore, if $q_a \geq q_r$, $f\left(-A(q_a-q_r)\right) < f\left(A(q_a-q_r)\right)$, and we obtain $V_f < 0$ and $V_b > 0$. Hence, the individuals move towards the center of the group, and the group will be stationary. On the other hand, if $q_r > q_a$, then $V_f > 0$ and $V_b < 0$, and the group will disperse. Since the stationary pulses displayed by the limiting parabolic equation (3.34), coincide with the stationary pulses displayed by the hyperbolic system (2.1), we conclude that the odd kernels have a similar effect on the hyperbolic system. We will come back to this result in Chapter 5. There, we will analyze numerically the solutions displayed by system (2.1). In particular, we will discuss the type of solutions that arise with only attractive and repulsive interactions.

We assumed that $f(y^{\pm}[u])$ is a monotone increasing function, and so is $f(y^{\pm}[u]) - f(-y^{\pm}[u])$. This suggests that when $p_r \neq p_l$, the two velocities are slightly different: $|V_f| \neq |V_b|$. In particular, since $p_r - p_l \ll 1$ and $A(q_a - q_r) > A(q_a - q_r)\,(1 - (p_r - p_l))$, it implies that for $q_a > q_r$, we obtain $V_f < 0$, $V_b > 0$, and $|V_f| < |V_b|$. Therefore, individuals at the front of the group will move slightly slower than those at the back of the group. This gives rise to a group drift, at least for a short period of time. Note that this difference between the velocity of the front and the back of the group is caused by large attraction, which influences especially those individuals positioned at the front. When $q_r = q_a$, we obtain $V_b = V_f = 0$, and the group is motionless.

Note that throughout this investigation we assumed that $p_r - p_l \ll 1$. However, if $p_r - p_l \gg 1$, and in particular $p_r - p_l = 2$, we obtain

$$V_f = V_b = -Af\left(-A(q_a - q_r)\right) + Af\left(A(q_a - q_r)\right). \tag{3.48}$$

In this case, the front and the back of the group move with the same velocity. Therefore, it requires a strong asymmetry in the reception of signals to overcome the strong attraction which slows down the front of the group.

These results show that it does not matter the particular shape of the turning function f. Only the monotonicity of f is important. If f is not monotone, then it is possible to find some values of q_r, q_a, and A, such that $V_b = -V_f$. In this case, the group will be stationary (even if $p_r \neq p_l$).

Mogilner and Edelstein-Keshet [80] showed that a nonlocal velocity with an odd kernel leads to stationary groups, while an even kernel gives rise to a group drift. This is true when the interactions are linear, that is when $\alpha^0[u]$ is a linear function of the nonlocal terms, as in equation (3.33). However, for nonlocal interactions defined by turning functions that are neither linear nor monotone, it is possible to have stationary groups when the kernel is even. For example, when $K(s)$ is even, $\int_{-6s_a}^{0} K(s)ds = \int_{0}^{6s_a} K(s)ds = (q_r - q_a)/2$. Then, the front and the back edge of the group are given by

$$V_f = -Af\left(\frac{A(q_r - q_a)}{2}\right) + Af\left(-\frac{A(q_r - q_a)}{2}\right) = V_f. \tag{3.49}$$

If f is not monotone, then it is possible to find some q_r, q_a, and A, such that $V_f = V_b = 0$, even for $q_a > q_r > 0$.

3.4 Discussion

In this chapter, we started analyzing the nonlocal hyperbolic model. In particular, we focused on the existence of mild solutions, and the reduction of this model to a well know parabolic model existent in the literature. The importance of the existence of solutions in L^∞ will be more clear in Chapter 6, when we will perform a weakly nonlinear analysis. This analysis will require solutions to belong to L^2. It is known that on a bounded domain, a solution bounded in the L^∞-norm, is also bounded in the L^2-norm [110].

In the second part of this chapter, we ignored the alignment interactions and formally connected the hyperbolic model (2.1) with the nonlocal parabolic model (1.2)-(1.4).This connection was made by assuming that both the speed and the turning rates approach infinity. The results show that the difference between the right and left turning rates leads to a nonlocal advection. Since the resulting parabolic equation does not have a local drift term, and the kernels are odd, the groups will be stationary. A similar result holds for the hyperbolic system (2.1). If asymmetry in the reception of communication signals is included, then this leads to a small, nonlocal drift term in the velocity, which can induce group movement. We will come back to this aspect in Chapter 5, when we will investigate numerically the effect of asymmetry in the communication on the patterns displayed by the hyperbolic system (2.1), and show that a similar result holds for it.

The condition that ensures the group movement is the monotonicity of the turning function. If the turning function is not monotone, one can obtain stationary groups even with nonlocal drift term in the velocity. In particular, when the kernels are even, the absence of this monotonicity assumption can lead to stationary groups. This results extends a results by Mogilner and Keshet [80] in regard to the effect of even and odd kernels on the velocities of individuals inside a group.

In the following chapter, we start investigating these patterns by studying the spatially homogeneous steady states and the temporal evolution of small perturbations of these states.

Chapter 4

Linear stability analysis

4.1 Introduction

A standard approach in the study of animal self-organization is to assess the possibility of pattern formation via linear stability analysis. In this chapter[1], we use this stability analysis to begin exploring the effect of social interactions on the group patterns. In particular, we will focus on the model described in Section 2.2, with interaction kernels defined by equations (2.11) (for attractive and repulsive interactions), and equation (2.9) for alignment. In Section 4.2, we first identify all the possible spatially homogeneous steady states. Then, in Section 4.3, we determine conditions under which these states lose their stability via growth of small spatial perturbations. The loss of stability through real or complex eigenvalues suggests a means by which aggregation or respectively, dispersive waves, can occur.

It is known that the observed group patterns depend on the scale of the social interactions [122]. Moreover, these scales depend on the type of communication signals used by animals [2, 134], the quality of the resources, and

[1] A version of this chapter has been published.

R. Eftimie, G. de Vries, M. A. Lewis, F. Lutscher, (2007) *Modeling group formation and activity patterns in self-organizing collectives of individuals*, Bull. Math. Biol., 69, 1537-1566.

R. Eftimie, G. de Vries, M. A. Lewis, (2007) *Complex spatial group patterns result from different communication mechanisms*, Proc. Natl. Acad. Sci., 104, 6974-6979.

the predation threat [7]. For example, the repulsion range decreases in case of predation, or when food resources are tightly packed. Another example is the range of a chemical signal. This range depends on the environmental conditions, but can be modified by an animal by varying the height at which the signal is emitted [2]. Motivated by these observations, in Section 4.4 we will use the stability results to investigate the effect of different interaction ranges on the formation of patterns. For simplicity, we will focus here on the particular communication mechanism introduced in Section 2.2 (model M1), and study the stability of the spatially homogeneous steady states as we vary the social interaction ranges.

In Section 4.5, we will go back to the five different hypothetical communication mechanisms, and investigate the conditions for full alignment within a population of individuals that is spread evenly over the domain. Previous results show that alignment makes animal groups more effective at finding food sources [40]. More precisely, because of the alignment, information regarding the surrounding environment propagates through the group much quicker, and therefore, the movement decisions are faster. It seems likely that the communication mechanisms used by different animal groups will play a role in these movement decisions. We will address this issue by answering the following question: how does the strength of the alignment force required for group polarization in each of the five sub-models depend on the amount of information an individual receives from its neighbors?

We conclude with a discussion in Section 4.6.

4.2 Spatially homogeneous steady states

To start, we assume that individuals are spread evenly over the domain, and we look for the spatially homogeneous steady states $u^+(x,t) = u^*$ and $u^-(x,t) = u^{**}$, with constant total density $A = u^* + u^{**}$. This leads to the following steady-state equation for system (2.1),

$$h(u^*; q_{al}, \lambda, A) = 0, \tag{4.1}$$

where h is being defined as

$$\begin{aligned} h(u^*; q_{al}, \lambda, A) \;:=\; & -u^* \left(1 + \lambda \tanh(Aq_{al} - 2u^* q_{al} - y_0)\right) + \\ & (A - u^*) \left(1 + \lambda \tanh(-Aq_{al} + 2u^* q_{al} - y_0)\right), \end{aligned} \tag{4.2}$$

where

$$\lambda = \frac{0.5\lambda_2}{0.5\lambda_2 + \lambda_1}. \tag{4.3}$$

Although the model involves a large number of parameters, only five of them arise in this steady-state equation: A, λ_1, λ_2, q_{al}, and y_0. Only the first four parameters will be varied, y_0 being fixed by our choice for the turning function. We look at the effect of varying A since we expect that the higher the population density, the stronger the inter-individual interactions. Therefore, we expect A to influence the aggregation process. A similar explanation holds for q_{al}. Intuitively, the turning rates also influence the formation of population clusters. The effects of varying all these parameters are presented in Figure 4.1.

From (4.2), we conclude that the only social interaction that determines the number of possible steady states is alignment. This follows from the choice of kernels $K_{r,a}$, which we have chosen to be odd, so that

$$\int_{-\infty}^{\infty} K_{r,a}(s)(u^* + u^{**})ds = 0. \tag{4.4}$$

Hence, the attraction and repulsion terms vanish in equation (4.2). When $q_{al} = 0$, the only steady state is $(u^+, u^-) = (A/2, A/2)$. Figure 4.1 (a) shows that this steady state does not depend on q_a. Actually, it does not depend on any of the other parameters describing the social interactions. However, as we will see in Section 4.3, the stability of this state will depend on these parameters. For $q_{al} \neq 0$, equation (4.1) can have one, three, or five solutions (Figure 4.1 (b)-(d)), depending on the values of λ. More precisely, there is a threshold value

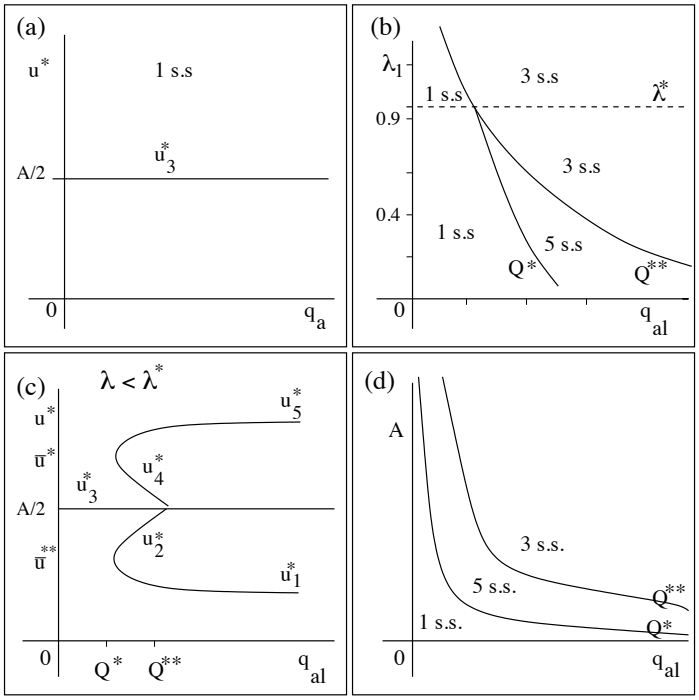

Figure 4.1: Bifurcation diagrams for the steady-state equation. (a) Bifurcation diagram when $q_{al} = 0$. The only steady state is $u^* = u^{**} = A/2$. (b) Two-parameter bifurcation diagram in (q_{al}, λ) space: the threshold values λ^*, Q^* and Q^{**} determine the number of possible steady states. Here $A = 2$ and $y_0 = 2$ are fixed parameters. (c) Bifurcation diagram in the five steady-state regime (i.e., $\lambda < \lambda^*$): $\bar{u}^*$ and $\bar{u}^{**} = A - \bar{u}^*$ are the two critical states that appear at Q^* as we increase q_{al}. These two states can take up to 5 values each: $\bar{u}^* \in \{u_1^*, u_2^*, u_3^*, u_4^*, u_5^*\}$, and $\bar{u}^{**} = A - \bar{u}^*$. Here $A = 2$, and λ is given by equation (14), with $\lambda_1 = 0.2$ and $\lambda_2 = 0.9$. (d) Two-parameter bifurcation diagram in (q_{al}, A) space: q_{al} and A have similar effects on the number of spatially homogeneous solutions. Here $\lambda_1 = 0.2, \lambda_2 = 0.9$.

$$\lambda^* = \frac{-1 + 3\tanh(y_0)^2}{2\tanh(y_0)} \tag{4.5}$$

such that for $\lambda > \lambda^*$ (i.e., for λ_1 much smaller than λ_2), there are up to three solutions, while for $\lambda < \lambda^*$, there are up to five solutions (Figure 4.1 (b)). We will denote these five solutions by u_i^*, $i = 1..5$. Therefore, the spatially homogeneous steady states generically denoted by $(u^*, u^{**}) = (u^*, A - u^*)$, can be any of the following pairs: (u_1^*, u_5^*), (u_5^*, u_1^*), (u_2^*, u_4^*), (u_4^*, u_2^*), or (u_3^*, u_3^*).

In the remainder of this chapter, we fix the ratio λ_1/λ_2 with $\lambda_1 << \lambda_2$, so that $\lambda < \lambda^*$, which implies that there can be up to five steady states (Figure 4.1 (b) and (c)). The other two threshold values for q_{al} from Figure 4.1 (b), namely Q^* and Q^{**}, are as follows: Q^{**} is given explicitly by

$$Q^{**} = \frac{-1 + \lambda\tanh(y_0)}{\lambda A\left(-1 + \tanh(y_0)^2\right)}, \tag{4.6}$$

while Q^* is a decreasing function of λ, defined implicitly by

$$\frac{\partial^3 h(A/2; Q^*, \lambda, A)}{\partial q_{al}^3} = 0. \tag{4.7}$$

The dependence of u^* on q_{al} is shown in Figure 4.1 (c), in the five steady states regime. As alignment becomes very large, and in particular $q_{al} \to \infty$, the three homogeneous steady states are $u^{\pm} \in \{A(1-\lambda)/2, A/2, A(1+\lambda)/2\}$. Figure 4.1 (d) illustrates the dependence of the number of steady states on both A and q_{al}, again in the five steady states regime. This last figure suggests that q_{al} and A have similar effects on the number of steady states: for small q_{al} or A, it is possible to have only one steady state $(u^*, u^{**}) = (A/2, A/2)$, while for large q_{al} or large A, there are three steady states. For intermediate values of q_{al} or A, there are five steady states.

4.3 Linear stability analysis: dispersion relation

Once we know the possible homogeneous steady states, the next step is to study the local stability of these solutions under small perturbations caused by spatially nonhomogeneous terms: $u^+(x,t) = u^* + u_p(x,t)$ and $u^-(x,t) = u^{**} + u_m(x,t)$, with (u^*, u^{**}) being the generic notation for the spatially homogeneous steady states. We approach the problem of pattern formation by choosing to define equation (2.1) on a bounded domain of length L with wrap-around boundary conditions for the nonlocal influence terms. This yields a problem with a discrete spectrum, and also approximates the process of pattern formation on an unbounded domain when L is large. In this case, the interaction kernels are, as in [109],

$$\Gamma_j(s) = \sum_{n=-\infty}^{+\infty} K_j(s + nL),\ j \in \{r, al, a\}. \tag{4.8}$$

The Fourier transform of the kernel $K_j(s)$ is given by

$$\hat{K_j}^{\pm}(k) = \int_{-\infty}^{\infty} K_j(s) e^{\pm iks} ds. \tag{4.9}$$

Also, we define

$$\hat{\Gamma_j}^{\pm}(k) := \int_{-L/2}^{L/2} \Gamma_j(s) e^{\pm iks} ds. \tag{4.10}$$

For large L, and in particular for $L \to \infty$, $\hat{\Gamma_j}^{\pm}(k)$ can be approximated by $\hat{K_j}^{\pm}(k)$. More precisely, we have the following:

$$\lim_{L\to\infty} \int_{-L/2}^{L/2} \Gamma_j(s) e^{\pm iks} ds = \lim_{L\to\infty} \int_{-L/2}^{L/2} \left(\sum_{n=-\infty}^{n=-1} K_j(s+nL) + K_j(s) + \sum_{n=1}^{\infty} K_j(s+nL) \right) e^{\pm iks} ds$$

$$= \lim_{L\to\infty} \int_{-L/2}^{L/2} K_j(s) e^{\pm iks} ds + \lim_{L\to\infty} \int_{-L/2}^{L/2} \left(\sum_{n=-\infty}^{n=-1} K_j(s+nL) + \sum_{n=1}^{n=\infty} K_j(s+nL) \right) e^{\pm iks} ds,$$

where the kernels decrease exponentially as $L \to \infty$ (see equations (2.9) and (2.11)). For large L, the terms containing the sums are approaching zero and therefore,

$$\lim_{L\to\infty} \int_{-L/2}^{L/2} \Gamma_j(s) e^{\pm iks} ds = \hat{K_j}^{\pm}(k). \tag{4.11}$$

Due to this correspondence, we will work on a large finite domain $[0, L]$, and use $\hat{K_j}(k)$ to approximate interactions on finite domain by interactions on infinite domain. Throughout this chapter, we will use the interaction kernels defined by equation (2.9) (for alignment) and equation (2.11) (for attraction and repulsion). The kernels are chosen such that the support of more than 98% of the kernels is small with respect to the length of the domain. The periodic boundary conditions that complete the description of the model on a finite domain are given by (2.12).

We let $u_{p,m}(x,t) \propto e^{\sigma t + ikx}$, with the discrete wave number $k_n = 2n\pi/L$, $n \in \mathbf{N}$, and the growth rate σ. Because of the conservation of the total density, $k_0 = 0$ is not an allowable wave number and hence, $n \in \mathbf{N}^+$. We substitute the expressions for $u_{p,m}(x,t)$ into system (2.1) to obtain the dispersion relation:

$$\sigma^2 + \sigma C(k) + D(k) = 0, \tag{4.12}$$

where

$$
\begin{aligned}
C(k) &= L_1 + L_2 - M_5 q_{al}(\hat{K}_{al}^{+}(k) + \hat{K}_{al}^{-}(k)), \\
D(k) &= \gamma^2 k^2 + \gamma i k \left(L_2 - L_1 + M_5 q_{al}(\hat{K}_{al}^{-}(k) - \hat{K}_{al}^{+}(k)) \right) \\
&\quad -2M_5 \gamma i k \left(q_r(\hat{K}_r^{+} - \hat{K}_r^{-}) - q_a(\hat{K}_a^{+} - \hat{K}_a^{-}) \right), \\
L_1 &= \lambda_1 + \lambda_2 0.5 + \lambda_2 0.5 \tanh(M_1 - y_0), \\
L_2 &= \lambda_1 + \lambda_2 0.5 + \lambda_2 0.5 \tanh(-M_1 - y_0), \\
P_1 &= \lambda_2 0.5(1 + \tanh^2(M_1 - y_0)), \\
P_2 &= \lambda_2 0.5(1 + \tanh^2(-M_1 - y_0)), \\
M_1 &= q_{al}(u^{**} - u^{*}), \\
M_5 &= P_1 u^{*} + P_2 u^{**}.
\end{aligned} \tag{4.13}
$$

Here, $\hat{K}_j$, $j \in \{a, r, al\}$ are the Fourier transforms of the interaction kernels (2.11) (for attraction and repulsion) and (2.9) (for alignment):

$$
\hat{K_j}^{+}(k) = \int_{-\infty}^{\infty} K_j(s) e^{iks_j} ds = iks_j \exp(-k^2 s_j^2/2),\ j = a, r, \tag{4.14}
$$

$$
\hat{K_{al}}^{\pm}(k) = \int_{-\infty}^{\infty} K_{al}(s) e^{\pm iks_{al}} ds = \exp(\pm i s_{al} k - k^2 m_{al}^2/2). \tag{4.15}
$$

Equations (4.12)-(4.13) show that the steady state (u^*, u^{**}) is locally unstable, i.e., $Re(\sigma(k)) > 0$, when $C(k) > 0$ or $D(k) < 0$. The first term, $C(k)$, is positive when λ_2 is large. For $D(k)$ to be negative, it requires either (a) a large λ_2, or (b) attraction to be larger than repulsion: $q_a \hat{K}_a(k) > q_r \hat{K}_r(k)$. If we focus now on each of the five solutions of equation (4.1) u_i^*, $i = 1..5$, we notice that equation (4.12) is important for the stability of $u_{1,5}^*$ (for $q_{al} > Q^*$), and of u_3^* (for $q_{al} < Q^{**}$). In this case, when λ_2 is large, the unstable modes are those with large k. When attraction is larger than repulsion, the modes with small k are unstable. However, the stability of $u_{2,4}^*$, as well as u_3^* when $q_{al} > Q^{**}$, is given not only by (4.12), but also by the domain length L. When the domain length becomes very large, and in particular $L \to \infty$, the first wave number $k_1 = 2\pi/L$ approaches zero. Consequently $C(k_1)$ approaches

$$
C(0) = L1 + L2 - 2M_5 q_{al}. \tag{4.16}
$$

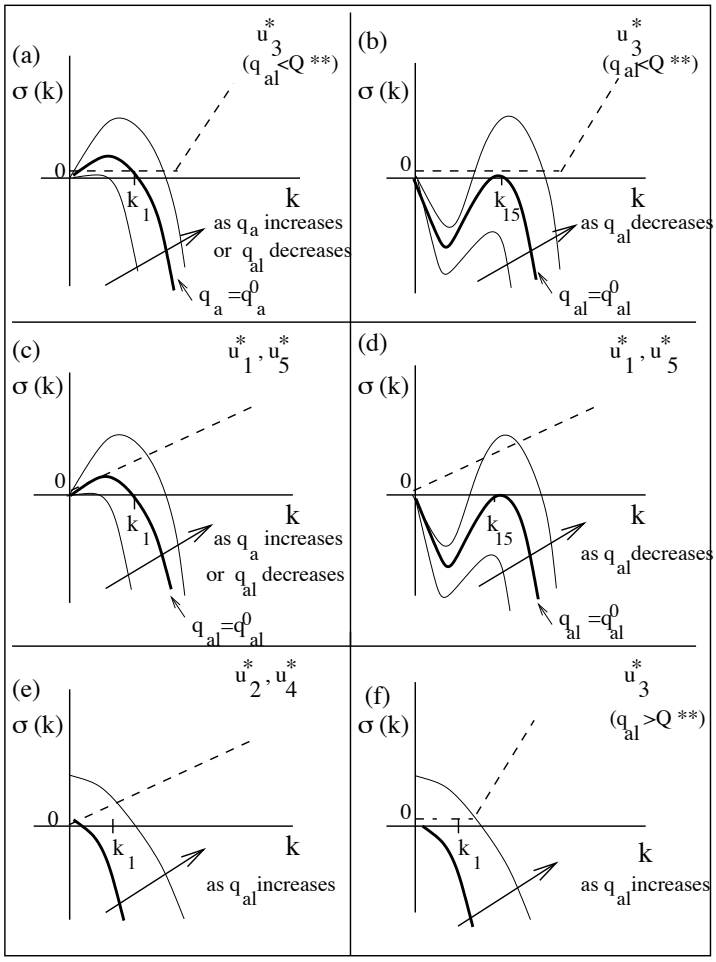

Figure 4.2: The dispersion relation $\sigma(k)$ for five possible spatially homogeneous steady states: u_1^*, u_2^*, u_3^*, u_4^*, u_5^*. The continuous line represents the real part of σ, while the dashed line represents the imaginary part. Cases (a) and (c) show the dispersion relation when attraction (q_a) is large. In this case, the critical wave number is $k = k_1$. Cases (b) and (d) show the dispersion relation for large turning rates (λ_2). The critical wave number that emerges is $k = k_j$, for some $j \gg 1$. Shown here is $k = k_{15}$. Note that for the steady state u_3^* (when $q_{al} < Q^{**}$), the imaginary part of the dispersion relation is zero at the critical wave number, whereas for u_1^* and u_5^*, it is always nonzero. Cases (e) and (f) show the dispersion relation for u_2^* and u_4^* when $q_{al} \in (Q^*, Q^{**})$, and for u_3^* when $q_{al} > Q^{**}$. In these cases, the critical wave number that emerges is k_1.

In this case, u_2^* and u_4^*, as well as u_3^* for $q_{al} > Q^{**}$, are always unstable. More precisely, for $u^* = u_3^*$, the condition $q_{al} > Q^{**}$ is equivalent to $C(0) > 0$, which means that u_3^* is locally unstable. The steady state $u^* = u_2^*$ (or $u^* = u_4^*$) and $u^{**} = A - u^*$ is given implicitly as a solution of the system

$$h(\bar{u}^*; Q^*, \lambda, A) = 0, \quad \frac{\partial h(\bar{u}^*; Q^*, \lambda, A)}{\partial q_{al}} = 0. \tag{4.17}$$

By studying the graph of $h(u)$, it can be deduced that the condition $q_{al} \in (Q^*, Q^{**})$ requires that $\frac{\partial h(u; q_{al}, \lambda, A)}{\partial q_{al}} > 0$, for any $u \in (\bar{u}^*, A/2)$. But this inequality is nothing else than $C(0) > 0$, which again leads to instability. Therefore, for large L, $u_{2,3,4}^*$ are locally unstable, even in the absence of attraction, or for small turning rates. This ensures that we have a standard subcritical pitchfork bifurcation, as shown in Figure 4.1(c).

Figure 4.2 (a)-(f) shows examples of the dispersion relation for system (2.1). The solid curve represents $Re(\sigma)$, while the dashed curve represents $Im(\sigma)$. Note that, for graphical purposes, we have replaced the discrete wave numbers with a continuum of values k. We observe that for cases (c), (d), and (e), $Im(\sigma(k)) \neq 0$, while for (a), (b), and (f), $Im(\sigma(k)) = 0$ for some $k > 0$. We recall that for the total density to be preserved, $k = 0$ is not an allowable wave number. Therefore, cases (e) and (f) do not contradict the conservation of the total density. The emergence of the first wave number k_1 (i.e., $Re(\sigma(k_1)) > 0$) (see Figure 4.2 (a) and (c)) is the result of large attraction, while the emergence of k_i, $i \gg 1$ (Figure 4.2 (b) and (d)) is the result of large turning rates. Therefore, when attraction is large, we would expect the emergence of one group. When the turning rates λ_1 and λ_2 are large, we would expect the emergence of i small groups, where $i \gg 1$. The last two cases (Figure 4.2 (e) and (f)) show the dispersion relation corresponding to $u_{2,4}^*$ for $q_{al} \in (Q^*, Q^{**})$, and to u_3^* for $q_{al} > Q^{**}$. As we can see here, the first wave number k_1 is always unstable, provided that the domain length L is large enough. In this case, k_1 is very close to 0 (but greater than 0), and we have already seen that $C(0) > 0$, which implies instability.

We can now connect the stability results shown in Figure 4.2 with the

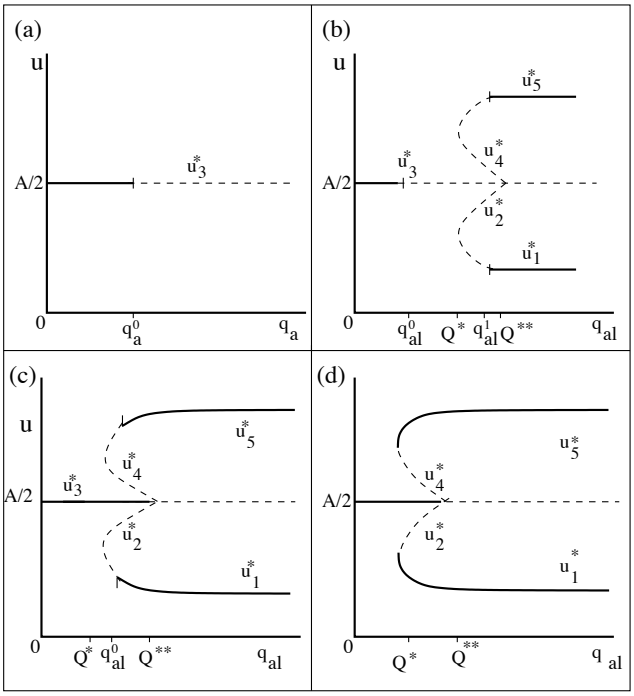

Figure 4.3: Bifurcation diagrams for the steady-state equation. (a) Zero alignment ($q_{al} = 0$); the only steady state is $u_3^* = A/2$. (b) Nonzero alignment ($q_{al} \neq 0$); $(u_3^*, u_3^*) = (A/2, A/2)$ is always a steady state; at the critical value $q_{al} = Q^*$, four new steady states appear through a saddle-node bifurcation. These states can be any of the following pairs: $(u_1^*, u_5^*), (u_5^*, u_1^*), (u_2^*, u_4^*), (u_4^*, u_2^*)$. At a second critical value of the alignment parameter, $q_{al} = Q^{**}$, two of these spatially homogeneous steady states (u_2^* and u_4^*) disappear through a subcritical pitchfork bifurcation. (c) A particular case of (b), obtained for a different parameter space. In all three cases, the solid lines denote the stable solution, while the dashed lines denote the unstable solution (with respect to spatial perturbations). Shown here is the stability of the steady states to small spatial perturbations when: (a) $q_{al} = 0$, $q_r = 2.2$, $\lambda_1 = 0.2$, $\lambda_2 = 0.9$, $\gamma = 0.1$, $A = 2$; here q_a is the bifurcation parameter; at $q_a = q_a^0$ there is a real bifurcation; (b) $q_a = q_r = 0$, $\lambda_1 = 0.2/0.7$, $\lambda_2 = 0.9/0.7$, $\gamma = 0.1$, $A = 2$; (u_3^*, u_3^*) undergoes a real bifurcation at $q_{al} = q_{al}^0$, while (u_1^*, u_5^*) undergoes an imaginary bifurcation at $q_{al} = q_{al}^1$; (c) $q_a = q_r = 0$, $\lambda_1 = 2.0$, $\lambda_2 = 9.0$; at $q_{al} = q_{al}^0$ there is an imaginary bifurcation

spatially homogeneous steady states $u_1^*...u_5^*$ described in Figure 4.1 (a) and (c). We can summarize the results as follows:

- Combining Figure 4.1(a) and Figure 4.2(a) leads to Figure 4.3(a). More precisely, when there is no alignment, the stability of the steady state u_3^* is determined by the magnitude of attractive interactions. There is a critical value of attraction $q_a = q_a^0$ such that the steady state u_3^* is stable for $q_a < q_a^0$, and unstable otherwise.

- Combining Figure 4.1(c) and Figures 4.2(a)-(f) gives Figures 4.3(b), (c), and (d). For example, if we focus on attraction (which influences the wave number k_1), then Figures 4.3 (b), (c), and (d) correspond to large, medium, and small values of attraction. Similarly, if we focus on the turning rates (which influence the large wave numbers $k_i, i \gg 1$), these figures correspond to large, medium, and small turning rates. In each of these cases, the spatially homogeneous steady state undergoes a bifurcation as we increase the value of alignment. The relative position of the bifurcation point depends on the parameter space. For example, Figure 4.3 (b) shows that for large attraction or turning rates, there exists a critical value of alignment $q_{al}^0 < Q^*$ such that for $q_{al} < q_{al}^0$, the solution u_3^* is stable, while for $q_{al} > q_{al}^0$ it is unstable. Moreover, there is there exists a second critical value $q_{al}^1 > Q^*$ such that for $q_{al} < q_{al}^1$, the solutions u_1^* and u_5^* are unstable, while for $q_{al} > q_{al}^1$ they are unstable. Figure 4.3 (c) shows that for medium attraction or turning rates, u_3^* changes stability at $q_{al} = Q^{**}$, while u_1^* and u_5^* change stability at a critical value $q_{al}^0 > Q^*$. Figure 4.3 (d) shows that for small attraction or turning rates, the only steady state that changes stability is u_3^*. The bifurcation point is $q_{al} = Q^{**}$.

It should be noted that equation (4.12) is complex when $u^* \neq u^{**}$, but real when $u^* = u^{**}$. This has implications for the type of the eigenvalues of system (2.1). For the first case, all eigenvalues are complex. For the second case, the eigenvalues can be real or complex, depending on the values of the parameters. We will come back to this aspect in Chapter 6, when we will

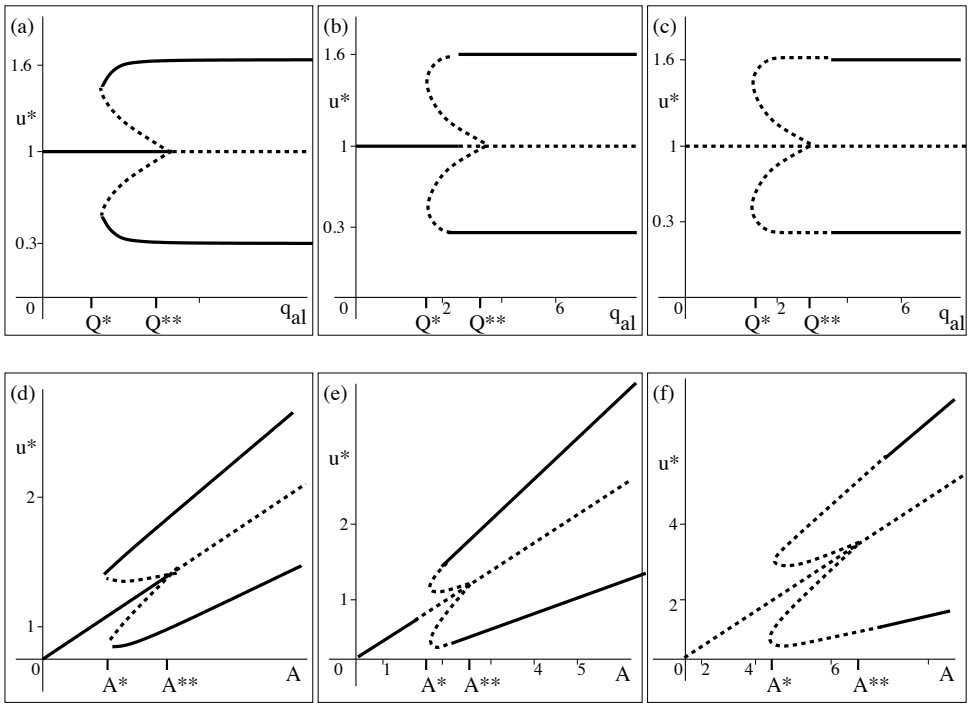

Figure 4.4: Spatially homogeneous steady states and their stability, as inter-individual attraction, q_a, increases: (a)-(c) show bifurcations in the (q_{al},u) plane, while (d)-(f) show bifurcations in the (A, u) plane. Solid curves represent the stable steady states, while the dotted curves represent the unstable steady states, as given by $Re(\sigma_1(k_1)) \geq 0$. The magnitude of attraction is increased from $q_a = 0.1$ for (a) and (d), to $q_a = 2$ for (b) and $q_a = 1$ for (e), and to $q_a = 10$ for both (c) and (f). As a result, the parameter range for the unstable steady states (i.e., the dotted curve) is also increasing.

perform a nonlinear analysis in the neighborhood of some bifurcation points at which the steady states become unstable.

The results concerning the steady states and the effect of the attraction, alignment and total population size on their stability are summarized in Figure 4.4. The solid curve represents stable steady states, while the dashed curve represents unstable steady states. Cases (a)-(c) show the effect of alignment and attraction on the stability of the steady states, whereas cases (d)-(f) show the effect of total population size and attraction on this stability. The values of

the turning rates are the same for all cases. The threshold values Q^*, Q^{**}, A^* and A^{**} determine the number of spatially homogeneous steady states. However, the stability of these steady states is greatly influenced by attraction and, not shown here, by the turning rates. One can see that an increase in the magnitude of attraction, from $q_a = 0.1$ for (a) and (d) to $q_a = 10$ for (c) and (f), leads to an increase in the parameter range (A and q_{al}) for the unstable steady states. If we look at the total population size, for instance, these results suggest that unless there is a very strong attraction, large number of individuals do not aggregate. Therefore, we conclude that both alignment and total population size have similar qualitative effects on the number of steady states (Figure 4.1(d)) as well as their stability (Figure 4.4).

We should also note that for small attraction ($q_a \leq q_r$) and large turning rates, it is possible to have a hysteresis phenomenon (Figure 4.4 (a) and (d)). More precisely, if we start for example with a very small q_{al}, then the only possible steady state is (u_3^*, u_3^*), and it is stable. As we increase alignment, this state will lose stability at $q_{al} = Q^{**}$ (Figure 4.4 (a)). Depending on initial conditions, the system will choose one of the two other solutions: (u_1^*, u_5^*) or (u_5^*, u_1^*), both of which are stable. However, if we now decrease the alignment beyond Q^{**}, the system will not return immediately to (u_3^*, u_3^*). It will return later, when u_1^* and u_5^* lose stability at Q^*. A similar phenomenon is observed when increasing and decreasing the total population size A.

4.4 The effect of different social interaction ranges on group formation

We now use the dispersion relation (4.12) to study the effect of the three interaction ranges, s_r, s_{al} and s_a on group formation. We investigate the stability of the spatially homogeneous steady state (u_3^*, u_3^*) by increasing (or decreasing) the size of these ranges while keeping all other parameters constant. At the end, we will briefly discuss the effect of these ranges on the stability of u_i^*, $i = 1, 2, 4, 5$. It should be mentioned that if for some j we have $Re(\sigma(k_j)) >$

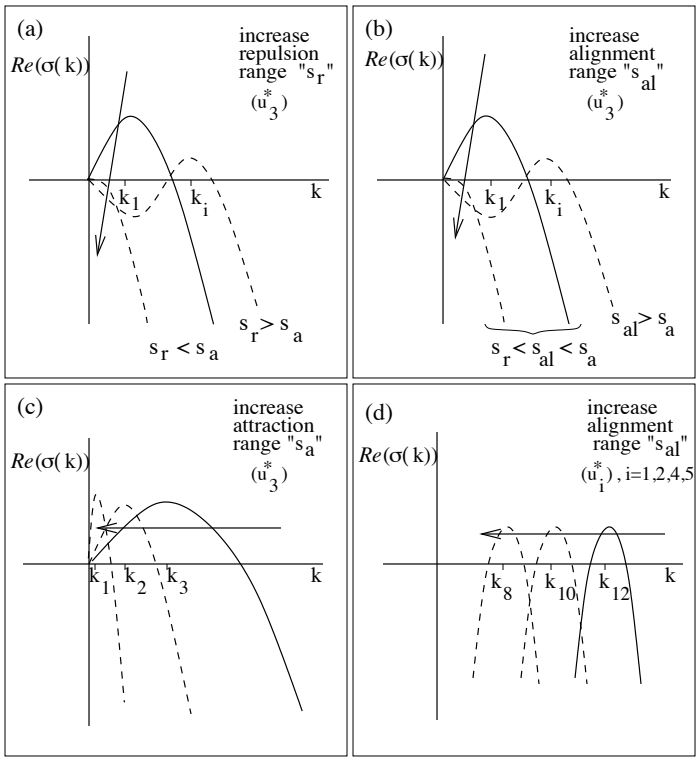

Figure 4.5: The effect of the interaction ranges s_r, s_{al} and s_a, on the local stability of homogeneous steady states u_i^*, $i = 1..5$. The plots show $Re(\sigma_1(k))$. The arrows show what happens with the graph of $Re(\sigma_1)$ as we increase the interaction ranges. For u_3^*, an increase in the repulsion range (case (a)) or the alignment range (case (b)) leads to stability of the steady state. For example, for case (a), let us assume that initially the mode that emerges is the one with the wave number k_1. As we increase the repulsion range s_r, making sure at the same time that $s_r < s_a$, we see that this mode becomes stable ($Re(\sigma_1(k_1)) < 0$). Increasing s_r even more (i.e., $s_r > s_a$), the mode that emerges is the one with the wave number k_i, $i > 1$. A similar explanation holds for (b). An increase in the attraction range (case (c)) results in a shift to the left of the wave number that will emerge. For u_i^*, $i = 1, 2, 4, 5$, an increase in the alignment range leads to the same shift to the left (case (d)).

0, while for all other $i \neq j$ we find $Re(\sigma(k_i)) < 0$, then the linear analysis predicts that j groups will emerge.

If we graph the dispersion relation, we see that an increase in the repulsion range, s_r, while keeping everything else constant, leads to the stability of u_3^* (Figure 4.5(a)). Increasing it even further would lead to the biologically unrealistic situation $s_r > s_a$. For alignment (Figure 4.5(b)), the results are similar to those obtained for the repulsion case. In particular, as we increase the alignment range s_{al}, making sure at the same time that $s_{al} < s_a$, the mode with the wave number k_1 becomes stable ($Re(\sigma(k_1)) < 0$). Increasing s_{al} even more (i.e., $s_{al} > s_a$), leads to the emergence of some mode with the wave number k_i, $i > 1$.

If we increase the attraction range, the dispersion relation shows a translation to the left of the wave number that becomes unstable (Figure 4.5(c)). For example, suppose k_2 is the unstable wave number initially (correspondingly, there are two groups). After increasing the attraction range, k_1 is the unstable wave number (correspondingly, there is one group). Biologically, this makes sense since when s_a is increased, individuals perceive information over larger distances. Two separate groups now can sense each other and merge.

The stability of the other four steady states u_i^*, $i = 1, 2, 4, 5$, does not seem to be influenced significantly by alterations in the size of the attraction or repulsion ranges. More precisely, neither the location nor the amplitude of the leading eigenmode varies much as the corresponding interaction ranges s_a and s_r vary. However, an increase in the alignment range results in a translation to the left of the wave number that emerges (Figures 4.5 (d)). This means that when there are more individuals moving in one direction than the other (i.e., the steady states (u^*, u^{**}) with $u^* \neq u^{**}$), the attempt to match one's movement direction to the movement direction of those neighbors that are farther away causes small groups of individuals to come together and form larger aggregations.

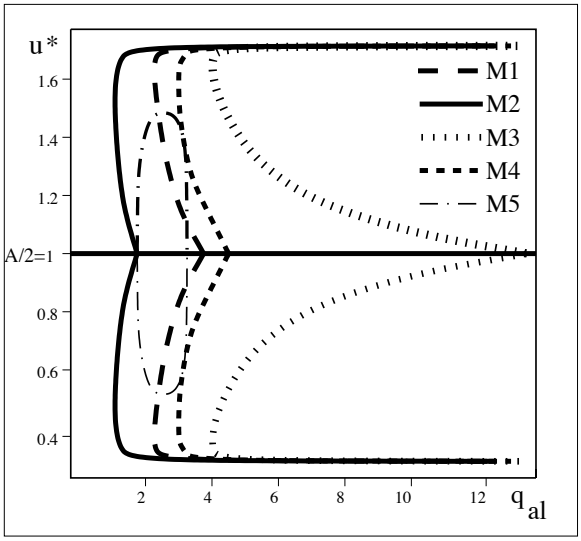

Figure 4.6: Bifurcation diagram comparing the spatially homogeneous steady states $(u^*, A-u^*)$ displayed by the five models M1 - M5, as alignment increases (total density $A = 2$, $q_a = 1.5, q_r = 1.1, \lambda_1 = 0.2, \lambda_2 = 0.9$). We see that for M2, a small q_{al} value already leads to polarization (i.e., the steady state is $(u^*, A - u^*)$, with $u^* \neq A/2$). M3, on the other hand, requires a larger value for q_{al}. For M5, only intermediate values of q_{al} lead to some polarization.

4.5 Relation between animal communication and alignment

It has been previously shown that while attraction and repulsion lead to the formation of animal aggregations [80, 123], alignment facilitates group movement by ensuring that the information propagates faster through the group [40]. However, how information propagates through the group depends on the communication signals (directional or omnidirectional) that animals use. Therefore, the question that arises is: what is the relation between alignment and the different communication mechanisms?

In the following, we investigate conditions under which a population of individuals that is evenly spread over the domain has most of its members

aligned in the same direction. That is, we look for spatially homogeneous steady states of the form $(u^*, A - u^*)$, with $u^* \neq A/2$. For this, we focus on the relation between the strength of the alignment force required in each of the five sub-models M1-M5 introduced in Chapter 2 (see table 2.2), and the amount of information an individual receives about its neighbors. Figure 4.6 shows the relationship between the strength of this force (q_{al}) and the spatially homogeneous steady states that arise in each of the sub-models. Depending on how much information it receives about its neighbors, an individual requires different levels of alignment. For example, we see that for M2, small q_{al} already leads to polarization. In this case, the individuals receive all possible information about neighbors positioned ahead and behind them (see Figure 2.5). For M3, on the other hand, only a large q_{al} value leads to polarization. In this case, the individuals receive information only from ahead. By comparing M3 and M4, we see that group polarization occurs for smaller values of alignment (q_{al}) when receiving partial information from both ahead and behind (M4), as compared to receiving full information only from ahead (M3). However, receiving information only from ahead, and only from neighbors moving in one direction (M5), leads to a lower level of polarization. Moreover, this polarization happens only for some intermediate values of q_{al}.

We conclude that there is an inverse relation between the amount of information received and the strength of alignment force required to fully align with neighbors. A similar result holds also for the turning rates.

4.6 Discussion

In this chapter, we performed a linear analysis of the model (2.1). First, we investigated the spatially homogeneous steady states, and showed that there is only one steady state independent of the parameters describing the social interactions. All other steady states depend on the magnitude of alignment, and therefore, they undergo saddle-node and pitchfork bifurcations, as this alignment parameter is varied.

The stability of all steady states depends on the magnitude of the interaction parameters, as well as the magnitude of the turning rates. In particular, attraction influences mainly the emergence of the first wave number k_1, while the turning rates influence the emergence of large wave numbers k_i, $i \gg 1$. In Chapter 6 we will come back to this result, when we will investigate some of the spatial and spatiotemporal patterns displayed by system (2.1).

The length scale of the interaction ranges also plays an important role in self-organization, as shown by analyzing the stability of the spatially homogeneous steady states when we vary these interaction ranges. However, the implications of these results are more complex. It is known that some communication signals (such as omnidirectional sound signals) act on long ranges, while other signals (such as directional sound signals) act on short ranges [134]. It is possible that understanding the effect of changing the interaction ranges on the resulting group patterns would offer important information on which communication signals are involved in the formation of these patterns. However, this aspect has not been investigated here.

Furthermore, the results suggest that there is an inverse relation between the amount of information received by an organism (due to environmental or physiological limitations), and the strength of the alignment that leads to a polarized population. More precisely, the more information one receives, the less alignment is necessary to form a polarized group. On the other hand, it is well known that animal signals and behaviors are not evolutionary independent traits [31]. On the contrary, since their functions are related, they will influence each other's evolution. Therefore, our analytical results suggest that there might be a possible evolutionary connection between the different communication mechanisms employed by various animals and the magnitudes of the social interactions required by group behaviors.

In the next chapter, we will use the stability results discussed here to investigate numerically the spatial and spatiotemporal patterns displayed by system (2.1).

Chapter 5

Numerical results

5.1 Introduction

Due to the complexity of the hyperbolic system (2.1), it is very difficult, if not impossible, to find an analytical solution. We therefore have to focus our attention on numerical solutions. In this chapter[1] , we perform numerical simulations for the two types of kernels we discussed in Chapter 2: (i) odd kernels for attractive and repulsive interactions, and translated Gaussian kernels for alignment (equations (2.11)), and (ii) translated Gaussian kernels for all three social interactions (equations (2.9)). Note that the first type of kernels have been used by Mogilner and Edenstein-Keshet [80] to model the long-range attractive and repulsive interactions in a parabolic model. We will use these kernels to compare the effect on the patterns displayed by our hyperbolic system with their results (see also the discussion in Chapter 3). However, these kernels have overlapping ranges, as in Figure 2.4(b). It might be more realistic to consider more distinct interaction ranges. For this reason, we will also perform simulations with the second type of kernels.

[1] A version of this chapter has been published.

R. Eftimie, G. de Vries, M. A. Lewis, F. Lutscher, (2007) *Modeling group formation and activity patterns in self-organizing collectives of individuals*, Bull. Math. Biol., 69, 1537-1566.

R. Eftimie, G. de Vries, M. A. Lewis, (2007) *Complex spatial group patterns result from different communication mechanisms*, Proc. Natl. Acad. Sci., 104, 6974-6979.

In the introductory chapter, we discussed the parabolic and hyperbolic models existent in the literature, none of which can account for the multitude of complex patterns that one can observe in nature. We recall that none of the one-dimensional models presented there incorporate all three social interactions, namely attraction, repulsion, and alignment. For example, the stationary pulses reported in [80, 123] were obtained with only attractive and repulsive interactions, whereas those reported in [71] were obtained with only alignment interactions. Also, the ripples reported in [59, 71] were the result of alignment interactions alone. In this chapter, we investigate the social interactions that are necessary for the formation of these spatial and spatiotemporal patterns. In particular, to allow for comparison with the previous models, we investigate the types of patterns that arise in the following three cases: (a) only attraction and repulsion; (b) only alignment; (c) full model with attraction, repulsion and alignment.

In Section 5.2, we discuss the numerical methods we use to simulate the solutions. Then, in Section 5.3, we begin investigating the patterns displayed by system (2.1). First, we focus on the communication mechanism introduced in Section 2.2 (and which corresponds to model M1), and thoroughly analyze this case. For comparison with other models existent in the literature, we use the kernels defined by (i). In Section 5.4, we broaden our investigation and discuss some of the patterns obtained with all five sub-models introduced in Chapter 2. To study the effect of non-overlapping interaction ranges on the resulting spatial and spatiotemporal patterns, we will consider the kernels defined by (ii) (that is, translated Gaussian kernels for all interactions). Therefore, for the communication mechanisms described in model M1, we can compare the patterns obtained with both types of kernels. Since the parameter spaces for which the solutions of the five sub-models are unstable do not coincide, we will focus only on some parameter subspaces. Note that we could also have studied models M2-M5 with kernels defined by (i). However, kernels (ii) seem more biologically realistic. For this reason we will use them throughout the rest of this thesis.

In Section 5.5, we investigate numerically the effect of introducing asym-

metry in the reception of signals. This aspect was discussed analytically in Chapter 3, when we derived the limiting parabolic equation. Here, we present some numerical results for the hyperbolic system.

We conclude with a discussion in Section 5.6.

5.2 Numerical method

To understand the behavior of system (2.1), we investigate numerically the evolution of small perturbations of the spatially homogeneous solutions (u^*, u^{**}) discussed in Chapter 4. To discretize equations (2.1), we first write them as

$$\mathbf{u}_t + (\mathbf{F}(\mathbf{u}))_x = \mathbf{s}(\mathbf{u}), \tag{5.1}$$

where $\mathbf{u} = (u^+, u^-)^T$, the flux term $\mathbf{F}(\mathbf{u}) = (\gamma u^+, -\gamma u^-)^T$, and the source term $\mathbf{s}(\mathbf{u}) = (-u^+\lambda^+[u^+, u^-] + u^-\lambda^-[u^+, u^-], u^+\lambda^+[u^+, u^-] - u^-\lambda^-[u^+, u^-])^T$. We discretize the space-time plane choosing a space step $\Delta x = h$, and a time step $\Delta t = k$. Also, we define the discrete mesh points $(x_j, t_n) = (jh, nk)$, $j, n \in \mathbf{N}$. The solutions $u1_j^n$ and $u2_j^n$ are seen as approximations of the cell averages of $u^{\pm}(x, t_n)$:

$$u1_j^n = \frac{1}{h}\int_{x_{j-1/2}}^{x_{j+1/2}} u^+(x, t_n)dx, \quad u2_j^n = \frac{1}{h}\int_{x_{j-1/2}}^{x_{j+1/2}} u^-(x, t_n)dx. \tag{5.2}$$

Moreover, we define the discrete flux $F_j^n = \mathbf{F}(u1_j^n, u2_j^n)$, and the discrete source terms $s_j^n = \mathbf{s}(u1_j^n, u2_j^n)$.

Since the eigenvalues of the Jacobian matrix of $F(\mathbf{u})$ have fixed signs $(\pm\gamma)$, we will use the following first-order upwind schemes to propagate the solution at the next time step (e.g., [47, 66]):

$$u1_j^{n+1} = u1_j^n - \frac{k}{h}(F_j^n - F_{j-1}^n) + ks_j^n, \tag{5.3}$$

$$u2_j^{n+1} = u2_j^n - \frac{k}{h}(F_{j+1}^n - F_j^n) + ks_j^n. \tag{5.4}$$

This numerical scheme is known to produce numerical diffusion, which smooths the shock fronts [66]. However, for the semi-linear system (2.1), the solutions have bounded gradients (see [14]), and eventual discontinuities can arise only

from the initial data. Moreover, higher-order schemes are not necessarily more accurate than the first-order schemes [47]. Based on these two facts, we prefer to use the upwind method throughout this chapter.

It should be specified that there are two types of instabilities associated with this numerical scheme [47]. First, there is a convective instability, when the Courant-Friedrichs-Lewy (CFL) condition is not satisfied, that is, when the time step k is such that $|\gamma|k/h > 1$. Second, because of the nonlocal turning rates, there is a relaxation instability determined by the eigenvalues of the matrix for the source term (that is, the right-hand-side of equations (2.1)). This second instability causes further restrictions on the time step k. The restrictions will depend on the maximum density of individuals. Throughout the simulations, we use the space step $h = 0.01$, and the time step $k = 0.038$ chosen such that it satisfies the CFL condition $| \pm \gamma|k/h = 0.38 < 1$ (here $\gamma = 0.1$). Note that this time step is enough to ensure that there is no relaxation instability.

To calculate the source terms s_j^n, we approximate the infinite integrals (2.5) – (2.8) by integrals on finite domains: $0 < x < 6j$, $j = s_r, s_a$, for attractive and repulsive kernels, and $0 < x < 2s_{al}$ for alignment. The approximation is accurate to order 10^{-8}:

$$\begin{aligned}
&\left| \int_0^\infty K_j(s) \left(u(x+s,t) - u(x-s,t)\right) ds - \right. \\
&\qquad \left. \left| \int_0^{6s_j} K_j(s) \left(u(x+s,t) - u(x-s,t)\right) ds \right| \leq 10^{-8}, \quad j = r, a \right. \\
&\left| \int_0^\infty K_{al}(s) \left(u^{\mp}(x+s,t) - u^{\pm}(x-s,t)\right) ds - \right. \\
&\qquad \left. \left| \int_0^{2s_j} K_{al}(s) \left(u^{\mp}(x+s,t) - u^{\pm}(x-s,t)\right) ds \right| \leq 10^{-8}. \right. \qquad (5.5)
\end{aligned}$$

These finite integrals are further discretized using Simpson's method [118]. Moreover, we choose the domain length L such that $6j \ll L$, $j = s_r, s_a$. We will perform simulations with both types of kernels K_j, $j = r, al, a$ (i.e., kernels described by equations (2.11), and kernels described by equations (2.9)).

As mentioned in Chapter 2, we use periodic boundary conditions throughout this thesis to allow for comparison with other models (see [17, 60]). This

requires the nonlocal interaction terms to wrap around the boundaries. More precisely, we define

$$\begin{aligned} u^{\pm}(x+s) &= u^{\pm}(0+s) \quad \text{if } x+s \geq L, \quad \text{and} \\ u^{\pm}(x-s) &= u^{\pm}(L-s) \quad \text{if } x-s \leq 0. \end{aligned} \tag{5.6}$$

A discussion of other types of boundary conditions for nonlocal transport problems can be found in [47].

To check the validity of the results obtained via linear stability analysis (Chapter 4), we choose the initial conditions to be small random perturbations of the spatially homogeneous steady states. The parameters for the domain length and interaction ranges are chosen to be $L = 10$, $s_r = 0.25$, $s_{al} = 0.5$, and $s_a = 1$. These four parameters, as well as y_0, m_{al}, m_a, m_r and A, are kept fixed during the simulations (see Table 2.1). All other parameters will be varied at some point. The parameters that are varied are precisely those that can be used to characterize animal groups during different behaviors.

We verified the numerical results by comparing with analytical predictions obtained via linear stability analysis, which predicted the wave numbers of perturbations which are unstable (see the discussion in Chapter 4). In particular, for predicted unstable wave numbers, the numerical simulations show pattern formation, while for stable wave numbers, there is no pattern. Moreover, the number of groups that arise in the simulations agree with the wave number that becomes unstable: $k_j = 2j\pi/L$, $j \in \mathbb{N}^+$.

To exclude the effect of the boundaries, we doubled the domain size. Moreover, to exclude possible artifacts of the numerical scheme, we refined the grid mesh. The results showed no significant differences.

The upwind scheme is sufficient for the results in this chapter. However, in Chapter 6 we will identify some bifurcation points for the spatially homogeneous steady states, and perform a weakly nonlinear analysis in the neighborhood of these points. Because of the diffusivity of the upwind scheme, it cannot be used to exactly identify the points where the steady states lose their stability. The points are identified with an accuracy of $O(10^{-1})$ only. To

increase the accuracy with which these points are identified, in Chapter 6 we will use a second-order McCormack scheme [47]:

$$\begin{aligned} \bar{u1}_j^n &= u1_j^n - \frac{k}{h}(F_j^n - F_{j-1}^n) + ks_j^n, \\ u1_j^{n+1} &= 0.5\left(\bar{u1}_j^n + u1_j^n - \frac{k}{h}(\bar{F}_{j+1}^n - \bar{F}_j^n) + k\bar{s}_j^n\right), \qquad (5.7) \\ \bar{u2}_j^n &= u2_j^n - \frac{k}{h}(F_j^n - F_{j-1}^n) + ks_j^n, \\ u2_j^{n+1} &= 0.5\left(\bar{u2}_j^n + u2_j^n - \frac{k}{h}(\bar{F}_{j+1}^n - \bar{F}_j^n) + k\bar{s}_j^n\right). \qquad (5.8) \end{aligned}$$

This scheme can identify the bifurcation points with a $O(10^{-2})$ error. Note that the final patterns obtained with this McCormack scheme are similar to those obtained using the upwind scheme.

5.3 Spatial and spatiotemporal patterns obtained for model M1 with odd attractive and repulsive kernels

We start the analysis of the spatial and spatiotemporal patterns displayed by system (2.1) by thoroughly investigating the model M1 introduced in Section 2.2, with kernels defined by (2.11). We should mention that all the patterns we will present in this section describe the long-time behavior of the solutions. In Section 5.4, we will also investigate some transitory patterns.

The numerical simulations show four types of possible behavior: stationary pulses, traveling pulses, traveling trains and zigzag pulses (Figures 5.1 and 5.2). By stationary pulses (Figure 5.1 (a) and (d)), we mean spatially nonhomogeneous steady states. Traveling pulses (Figure 5.1 (b)) are defined as spatially nonhomogeneous solutions that have a fixed shape and move at a constant speed c: $u^{\pm}(x,t) = U^{\pm}(z)$, $z = x - ct$, and $U^{\pm}(\pm\infty) = 0$. The periodic boundary conditions allow us to treat the domain as infinite, and therefore it makes sense to consider traveling pulses. Traveling trains (Figure 5.1 (c)) are periodic solutions of the form $u^{\pm}(x,t) = U^{\pm}(z)$, $z = x - ct$, with

$U^{\pm}$ periodic functions of z. The zigzag pulses (Figure 5.2) are traveling solutions that periodically change direction. Moreover, compared to the case of traveling pulses, where the shape of the solutions does not change, for zigzag pulses the shape changes slightly when the entire group turns around.

A first observation is that both stationary and moving groups have clearly defined boundaries, where the population density drops to zero very quickly. Moreover, in the case of moving groups (Figure 5.1(b)), the profile is steeper at the leading edge of the group, and shallower at the back. This phenomenon is caused by attraction towards other individuals. Under the influence of the attractive force, organisms at the front of the group have the tendency to turn around more often, to stay in contact with the others. Therefore, they move slower than those at the rear of the group, and this leads to crowding at the leading edge of the group.

In what follows, we present the results in three separate cases: (a) a case that contains only attraction and repulsion, (b) a case with only alignment, and (c) a case that takes into consideration all three social interactions. The types of solutions that can be obtained in each of these cases are summarized in Table 5.1, and discussed below. These results were simulated with fixed parameters sampled from the ranges described in Table 5.2.

(i) Only attraction and repulsion. For $q_{al} = 0$, the only possible spatially homogeneous solution is $(u^+, u^-) = (u_3^*, u_3^*)$ (as described by Figure 4.3 (a)). In the parameter range where it is unstable, if we start with small random perturbations of this steady state as initial conditions, we obtain stationary pulses (Figure 5.1 (a)). We sampled a large number of parameter combinations (from the parameter space where u_3 is unstable), and the results always showed stationary pulses. These results suggest that attraction and repulsion are sufficient to cause group formation, but not sufficient to make the group travel.

(ii) Only alignment. When alignment is the only social force considered, it is possible to have up to five spatially homogeneous solutions (u_i^*, $i = 1..5$) (Figure 4.3). Locally unstable steady states (Figure 4.2 (d) and (b))

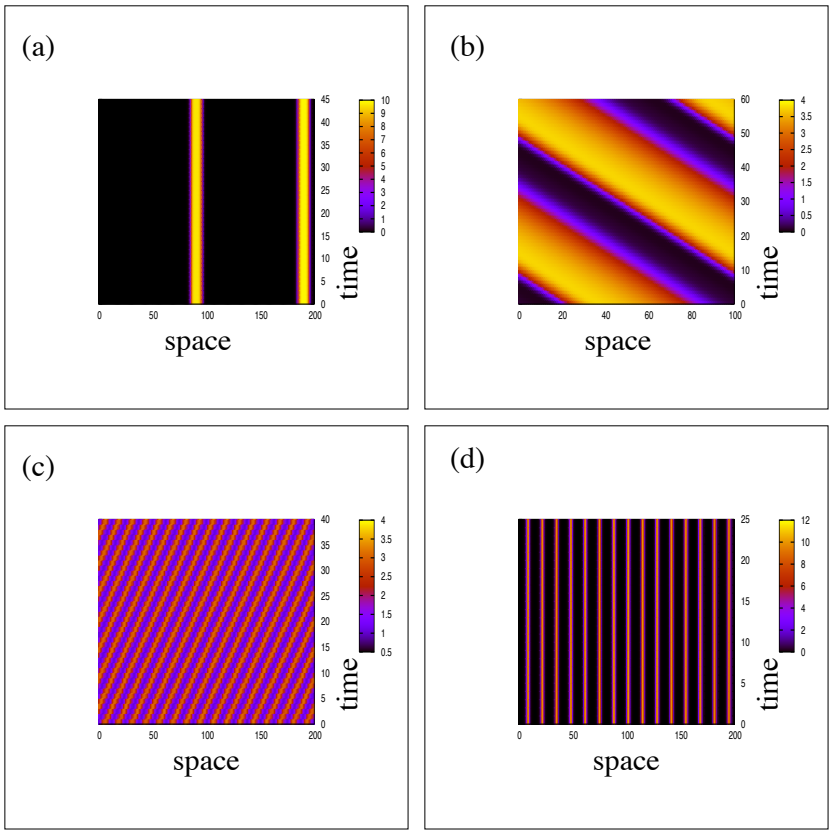

Figure 5.1: Examples of long-time behavior displayed by model M1, with odd attractive and repulsive kernels: (a) Stationary pulses obtained for $q_a > q_r$ and no alignment: $q_a = 10$, $q_r = 0.1$, $q_{al} = 0$, $\gamma = 0.1$, $\lambda_1 = 0.2$, $\lambda_2 = 0.9$; (b) Traveling pulse: $q_a = 3.2$, $q_r = 1.0$, $q_{al} = 2.6$, $\gamma = 0.1$, $\lambda_1 = 0.2$, $\lambda_2 = 0.9$; (c) Traveling trains obtained for $q_{al} = 2.0$, $q_a = 0$, $q_r = 0$, $\gamma = 0.1$, $\lambda_1 = 0.4$, $\lambda_2 = 1.8$; (d) Stationary pulses, obtained for $q_{al} = 2$, $q_a = 0$, $q_r = 0$, $\gamma = 0.1$, $\lambda_1 = 1.33$, $\lambda_2 = 6$.

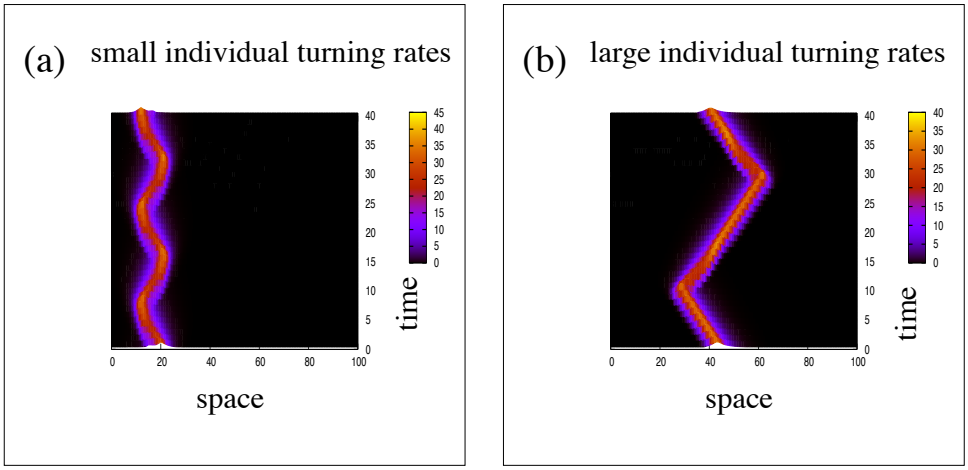

Figure 5.2: Zigzag movement obtained for model M1, with odd attractive and repulsive kernels. The brighter the color, the higher the population density. Here $q_a \gg q_r$. Case (a) shows the pattern for small turning rates, whereas (b) shows the pattern for large turning rates. The following parameters are the same for all these two cases: $q_r = 1.2$, $q_a = 15.0$, $q_{al} = 2.0$, $\gamma = 0.1$. The turning rates are as following: for (a) $\lambda_1 = 0.2$, and $\lambda_2 = 0.9$; for (b) $\lambda_1 = 0.33$, $\lambda_2 = 1.5$. The structure of a turn during zigzag movement is determined by the turning rates. For small individual turning rates, the density is higher *during* the turn (i.e., the group is more compact), while for large individual turning rates (especially for large λ_2), the density is higher *between* the turns.

Case	Social interactions	Traveling trains	Traveling pulses	Stationary pulses	Zigzag pulses
(i)	**Only attraction and repulsion**	No	No	Yes	No
(ii)	**Only alignment**	Yes	No	Yes	No
(iii)	**Attraction, repulsion, and alignment**	Yes	Yes	Yes	Yes

Table 5.1: A summary of the different types of possible solutions exhibited by model M1 under the influence of three different sets of social interactions: traveling trains, traveling pulses, stationary pulses, and zigzag pulses. The patterns represent the long-time behavior of the solutions.

Activity	γ	λ_1, λ_2	q_{al}	q_r	q_a
Traveling	large	small	large	small	large
Foraging	medium, large	large	medium	large	small
Rest	small	medium	small	medium	medium

Table 5.2: Examples of magnitudes of model parameters that characterize animal behavior corresponding to different activities. The magnitudes correspond to parameters varying within the following ranges: $\gamma \in (0.01, 0.1)$, $\lambda_1 \in (0.2, 2)$, $\lambda_2 \in (0.9, 9)$, $q_{al} \in (0, 3)$, $q_r \in (0.1, 3)$, $q_a \in (0.1, 3)$.

are possible when the turning rates are large, and these solutions evolve into either traveling trains (Figure 5.1 (c)) or stationary pulses (Figure 5.1 (d)). More precisely, traveling trains are possible when the initial conditions are perturbations of $(u^+, u^-) = (u_1^*, u_5^*)$, whereas stationary pulses are obtained

when we start either with perturbations of (u_3^*, u_3^*), or with perturbations of (u_1^*, u_5^*) and very large turning rates.

(iii) Attraction, repulsion and alignment. The most complex behavior is obtained when all three social interactions take place. In addition to the behaviors described above, we observe zigzag pulses in this case (Figure 5.2 (a), (b)). This behavior is caused by high inter-individual attraction ($q_a \gg q_r$).

Note that for the zigzag movement, the lengths of the paths are correlated with the turning rates, λ_1 and λ_2. In Figure 5.2 (a), the turning rates are small (i.e., $\lambda_1 = 0.2, \lambda_2 = 0.9$), and we observe short path lengths. In contrast, when we increase the turning rates (e.g., $\lambda_1 = 0.33$, $\lambda_2 = 1.5$), we observe longer path lengths, as shown in Figure 5.2 (b). The explanation for this is that when these rates are small, the individuals in the middle part of the group as well as those at the back do not turn very often. However, due to large attraction, those at the front of the group turn around to make sure they are still with the rest of the group. This leads to a steep increase in the number of individuals at the leading edge of the group, who move in the opposite direction. As a result, the entire group turns around. On the other hand, when the turning rates are large, the straight paths between group turning maneuvers are much longer. The individual turns help organisms to move away from their neighbors, and keep them well spaced for a longer time.

Another important aspect of the zigzag movement that should be mentioned is the structure of the turn. More precisely, small turning rates (Figure 5.2 (a)) lead to a very compact group *during* the turns, while large turning rates (Figure 5.2 (b)) make the group more compact *before* the turning maneuver, but less compact during and after the turn.

Zigzag movement can be understood to be a transitory type of behavior between traveling pulses, obtained when attraction is small, and stationary pulses, obtained when attraction is extremely large compared to repulsion, as shown in Figure 5.3. If we increase attraction, the model shows a transition from one type of solution to another. For attraction taking small to medium values compared to repulsion, the system displays traveling pulses (as

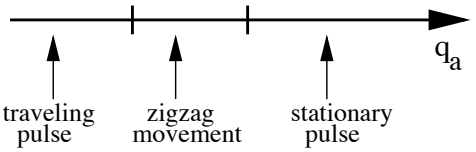

Figure 5.3: An illustration of the possible types of solutions and the transitions between them as one varies the attraction parameter q_a. Initially, there is a traveling pulse, and as attraction increases, it starts moving in a zigzag manner. A very large attraction force keeps all individuals together, hindering the group movement.

in Figure 5.1(b)). As the magnitude of attraction increases, these groups start moving back and forth, in a zigzag manner (as in Figure 5.2). When this social interaction becomes extremely strong (for example $q_a = 20$, and $q_r = 0.1$, and all other parameters as specified in Figure 5.2), the aggregations become stationary.

A similar transitory type of behavior can be obtained when varying multiple parameters. For example, the model could be used to describe the succession of daily activity patterns exhibited by different groups of animals. Usually, these transitions from one activity to another can be influenced by internal factors (e.g., hunger, necessity to rest, etc.) or external ones (e.g., temperature [125] or light [48]). These factors have an impact on group parameters, such as motility, and this translates into different turning rates and speed [125].

To exemplify this transitional process, we look at the following succession of activities: forage $\rightarrow$ rest $\rightarrow$ travel $\rightarrow$ forage. The initial conditions for forage are random perturbations of spatially homogeneous steady state (u_1^*, u_5^*). For the next three activities, the initial conditions for the simulations are the densities generated by the previous activity. Table 5.2 summarizes possible relative magnitudes for model parameters.

Figure 5.4 shows the outcome of the numerical simulation which describes this succession of activities. Initially, there are many small clusters that travel for a while, and then stop. During the resting period, the groups are stationary, with the peak of total local densities decreasing. However, as both

attraction and alignment increase to simulate travel, all animals gather into one large aggregation, which moves towards a new site. Once arrived there, parameters are changed to simulate foraging and the group spreads again. It should be noted that even though we use the same parameters to simulate the two foraging behaviors, the initial conditions play a very important role. Initially, the small groups that form during foraging are moving through the domain. When we change the parameters from travel back to foraging, the groups that arise are now stationary. A similar hysteresis phenomenon was obtained in [24], with a Lagrangian model.

It was previously shown [37, 40] that group polarization helps populations to improve their searching behavior, by climbing noisy gradients faster. Our model shows that without alignment and in the absence of external environmental cues, group movement does not occur. Group movement is possible with alignment, but it depends on the magnitude of the turning rates: high individual turning rates make it impossible for the group to move as an entity. Therefore, we can say that alignment appears to be a necessary ingredient, but not a sufficient one for group movement.

In conclusion, the model shows that interactions between different social factors give rise to a wide range of patterns. We have seen, for example, that medium attraction combined with repulsion and alignment leads to traveling pulses, while large attraction plus repulsion and alignment leads to zigzag pulses. None of these two types of solutions can be obtained with alignment alone, nor with attraction and repulsion alone. They are the result of all three social interactions.

5.4 Spatial and spatiotemporal patterns for different communication mechanisms

We now focus on the patterns displayed by the hyperbolic model (2.1) when we consider five different communication mechanisms. Here, we will consider the interaction kernels defined by equations (2.9).

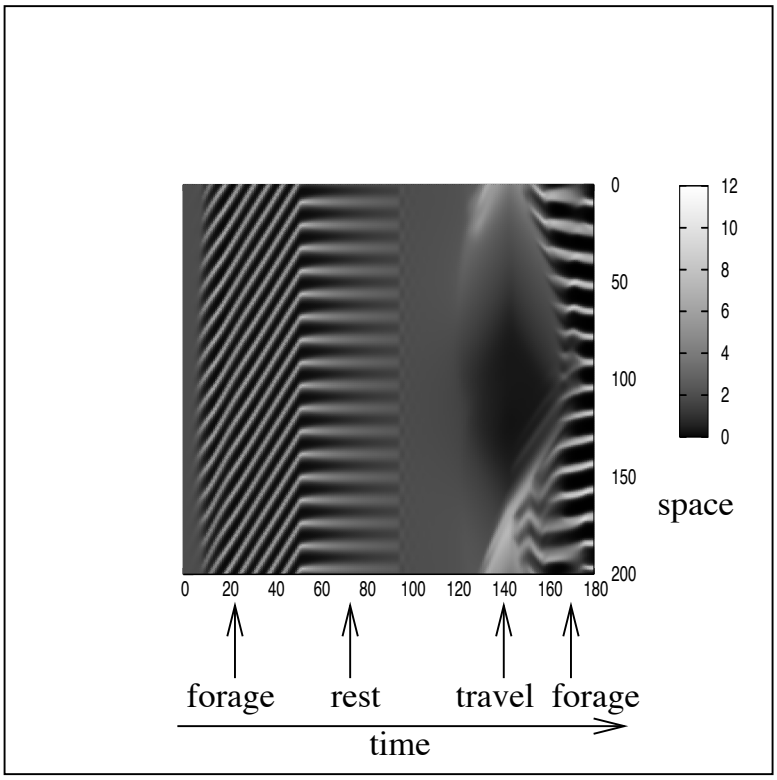

Figure 5.4: The figure shows a "bird's eye view" for the total population density during the succession of three activities: forage → rest → travel → forage. The lighter the color, the higher the population density. Parameter values are chosen in accordance with Table 2. During foraging ($q_r = 2.0$, $q_a = 0.1$, $q_{al} = 1.9$, $\gamma = 0.089$, $\lambda_1 = 1.3$, $\lambda_2 = 6$), individuals turn frequently and attraction is smaller than repulsion, which leads to many small groups moving around the domain. During rest ($q_r = 0.10$, $q_a = 2.1$, $q_{al} = 0.5$, $\gamma = 0.015$, $\lambda_1 = 0.286$, $\lambda_2 = 1.286$), the individuals slow down and turn less frequently. The groups have now a tendency to disperse. To travel ($q_r = 0.5$, $q_a = 4.1$, $q_{al} = 2.0$, $\gamma = 0.1$, $\lambda_1 = 0.2$, $\lambda_2 = 0.9$), the attraction increases and all the individuals come together to form one large group that moves around the domain. To forage again, the group splits into multiple small groups that spread over the domain.

As in the previous section, we investigate the types of spatial patterns that arise in three cases: (a) only attraction and repulsion; (b) only alignment; (c) full model with attraction, alignment and repulsion. Moreover, compared to Section 5.3, where we investigated only the patterns that represent the long-time behavior of the solutions, in this section we also discuss some transitory patterns that occur at intermediate times.

For the numerical simulations, we focused on the parameter space where the wave numbers of the perturbations are unstable, as predicted by the linear stability analysis. However, since there are so many parameters (even after nondimensionalization), and the parameter spaces corresponding to the five sub-models do not overlap perfectly, we have sampled only some parameter subspaces.

- Case (a): we fix $q_{al} = 0, \gamma = 0.1, \lambda_1 = 0.2, \lambda_2 = 0.9$, and $A = 2$. The sampled parameter subspace is (q_a, q_r), with $q_a, q_r \in [0.5, 9]$. For the initial conditions we consider $u^* = u^{**}$.

- Case (b): we fix $q_a = q_r = 0, \gamma = 0.1, A = 2$, and investigate the influence of the turning rates on the group structure. For this, we define $\lambda_1 = 0.2/\tau$, $\lambda_2 = 0.9/\tau$, and vary τ. The sampled parameter subspace is (q_{al}, τ), with $q_{al} \in [0.5, 10]$, and $\tau \in [0.006, 1]$. As initial conditions, we consider $u^* \neq u^{**}$.

- Case (c): we fix $\gamma = 0.1, \lambda_1 = 0.2, \lambda_2 = 0.9, A = 2$. The sampled parameter subspace is (q_a, q_r), with $q_a, q_r \in [0.5, 10]$. As initial conditions, we consider $u^* = u^{**}$.

It should be specified that the obtained patterns are robust to parameter changes, in the sense that each pattern is observed for a range of parameters.

The numerical simulations reveal ten types of spatial and spatiotemporal patterns, shown in Figures 5.5 and 5.6: (1) stationary pulses formed of small, high-density subgroups; (2) stationary pulses that have a relatively constant internal density; (3) ripples; (4) feathers; (5) traveling pulse; (6) traveling train ; (7) zigzag pulses; (8) breathers; (9) traveling breathers; (10) semi-

zigzag pulses. Patterns (1)-(3), and (5)-(6) are classic patterns (see [85] and [60]). The other five patterns are new for this area of animal group formation. In the following we give a short characterization of all of these patterns.

- **Stationary pulses.** As mentioned in Section 5.3, the stationary pulses (Figure 5.1(a),(d), and Figure 5.5(1),(2)) are spatially nonhomogeneous steady states that are motionless in time. Note that, compared to the pulses obtained in Section 5.3, here we can also obtain pulses formed of high-density subgroups. These pulses are the result of considering very localized attractive and repulsive interactions.

- **Traveling pulses.** Traveling pulses (Figure 5.1(b) and Figure 5.5(5)) are defined as spatially nonhomogeneous solutions that have a fixed shape and move at a constant speed c: $u^{\pm}(x,t) = U^{\pm}(z)$, $z = x - ct$, and $U^{\pm}(\pm\infty) = 0$. With this definition, we can understand the stationary pulses as as being traveling pulses that move with zero speed ($c = 0$).

- **Traveling trains.** Traveling trains (Figure 5.1(c) and Figure 5.5(6)) are periodic solutions of the form $u^{\pm}(x,t) = U^{\pm}(z)$, $z = x - ct$, with $U^{\pm}$ periodic functions of z. We should specify here that the traveling train is a pattern that doubles the number of its peaks when we double the domain size. A traveling pulse, on the other hand, has the same number of peaks when we double the domain size.

- **Ripples.** Ripples (Figure 5.5 (3)) are left-moving and right-moving traveling waves that pass through each other [60]. Note that the pattern show in Figure 5.5 (3) is a transient pattern. For very large time, the individuals aggregate into a stationary group.

- **Feathers.** We call feathers (Figure 5.5 (4)) those stationary pulses that lose and gain subgroups of individuals at the edge.

- **Breathers.** Breathers (Figure 5.5 (8)) are stationary pulses that periodically expand and contract. This leads to a periodic change in the amplitude of the solutions.

- **Traveling breathers.** Traveling breathers (Figure 5.5 (9)) are breather-like groups that travel through the domain.

- **Zigzag pulses.** As mentioned in Section 5.3, the zigzag pulses (Figure 5.2, and Figure 5.5 (7)) are traveling solutions that periodically change direction. Moreover, compared to the case of traveling pulses, where the shape of solutions does not change, for zigzag pulses the shape changes slightly when the entire group turns around ([30]).

- **Semi-zigzag pulses.** The semi-zigzag pulses (Figure 5.6 (a),(b)) are pulses characterized by movement in one direction, alternated by rest. These pulses are a temporal transition between traveling trains (at the start of the simulations) and stationary pulses (after the simulations run for a long time). It should be mentioned that it is possible to obtain these pulses also for the case discussed in Section 5.3 (i.e., model M1 with type (i) kernels). In that section, we focused only on the long-time behavior of solutions, and therefore this pattern was not discussed there. As we will shortly see, the patterns are obtained when alignment is the only social interaction. Therefore, it does not matter what type of kernels we consider for attractive and repulsive interactions.

Table 5.3 shows a summary of the patterns observed in the three cases: (a) only attraction and repulsion, (b) only alignment, (c) attraction, repulsion and alignment. The *dashes* indicate that the pattern was not observed. Since we do not sample the entire parameter space, we note that Table 5.3 might not be complete. Moreover, it is likely to find other new and interesting patterns, in different parameter subspaces. Such an example will be discussed in Section 5.5. Our aim here is not to find all patterns, but to open the door towards the numerous possibilities offered by our modeling procedure.

By fixing all the parameters, we can investigate the role of different model assumptions (M1 versus M2, etc.) in determining the resulting spatial pattern. We do this in the context of all three social interactions: attraction, repulsion, and alignment (i.e., case (c)). We set $q_r = q_a = 4, q_{al} = 2$ (that is, attraction

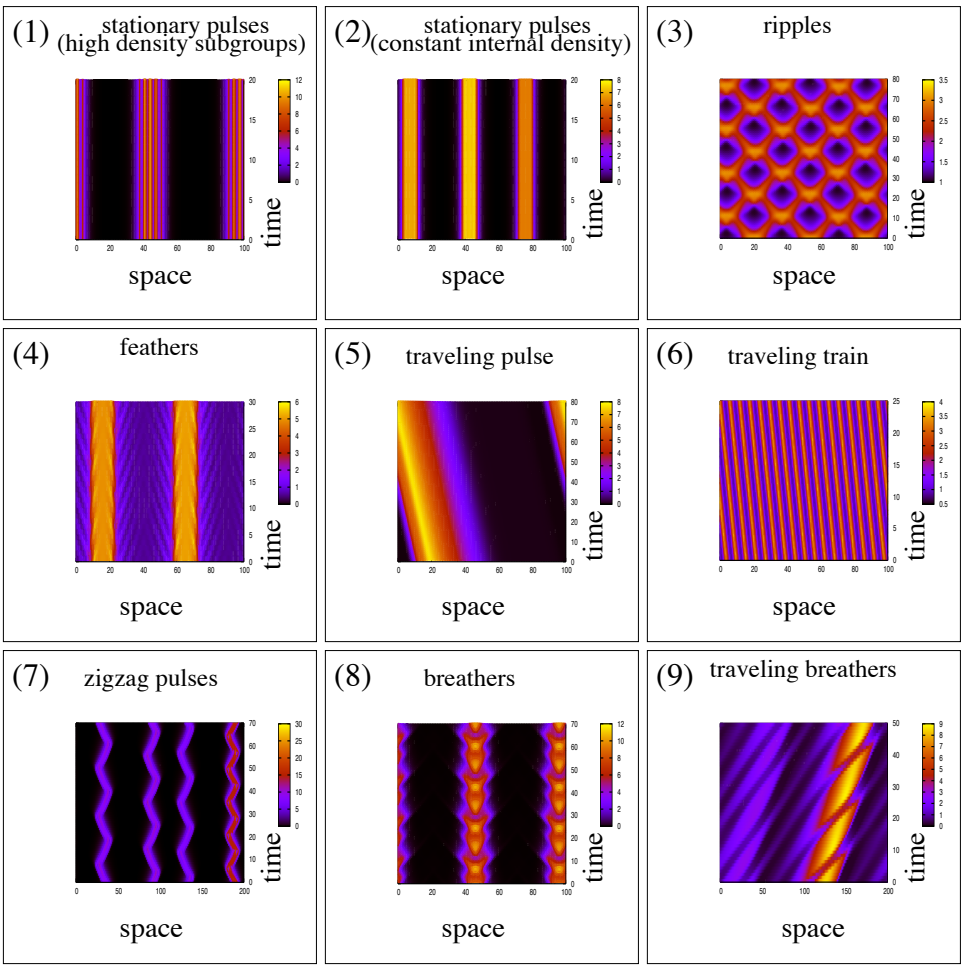

Figure 5.5: Examples of spatial patterns displayed by models M1-M5 (shown is total density $u = u^+ + u^-$): (1) stationary pulses formed of small, high-density subgroups (shown M1: $q_{al} = 0, q_a = 2, q_r = 2.4, \lambda_1 = 0.2, \lambda_2 = 0.9$); (2) stationary pulses (density even distributed over the group) (shown M2: $q_{al} = 0, q_a = 4, q_r = 0.5, \lambda_1 = 0.2, \lambda_2 = 0.9$); (3) ripples (shown M5: $q_{al} = 2, q_a = 1.5, q_r = 1.1, \lambda_1 = 0.2, \lambda_2 = 0.9$); (4) feathers (shown M3: $q_{al} = 0, q_a = 6, q_r = 6.4, \lambda_1 = 0.2, \lambda_2 = 0.9$); (5) traveling pulse (shown M1: $q_{al} = 2, q_a = 1.6, q_r = 0.5, \lambda_1 = 0.2, \lambda_2 = 0.9$); (6) traveling trains (shown M3: $q_{al} = 2, q_a = 0, q_r = 0, \lambda_1 = 6.67, \lambda_2 = 30.0$); (7) zigzag pulses (shown M4: $q_{al} = 0, q_a = 2, q_r = 2, \lambda_1 = 0.2, \lambda_2 = 0.9$); (8) breathers (shown M4: $q_{al} = 0, q_a = 2, q_r = 1, \lambda_1 = 0.2, \lambda_2 = 0.9$); (9) traveling breathers (shown M4: $q_{al} = 2, q_a = 4, q_{al} = 4, \lambda_1 = 0.2, \lambda 2 = 0.9$). The rest of the parameters are: $\gamma = 0.1, s_r = 0.25, s_{al} = 0.5, s_a = 1.0, m_r = s_r/8, m_{al} = s_{al}/8, m_a = s_a/8$. For these simulations, we choose the function f in equation [2.3] to be described by

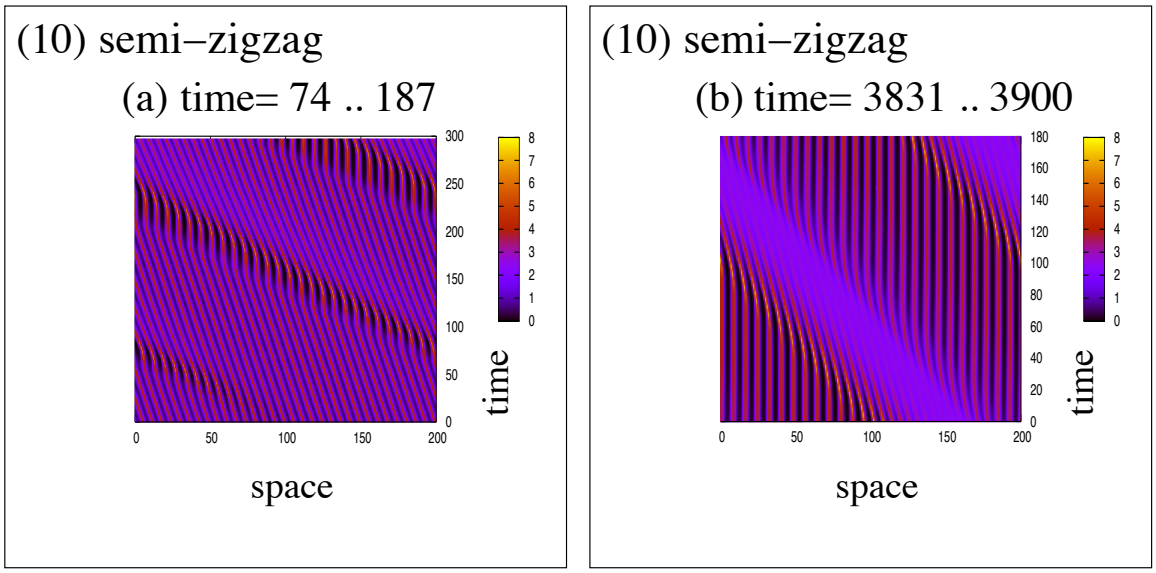

Figure 5.6: Semi-zigzag pattern (10). (a) Initially, all subgroups move to the left. After approximatively 20 time steps some groups of individuals (shown here to be positioned in space around the mark 50) become stationary for a very short time (approximately 10-20 time steps). This leads to other neighboring groups, which are positioned at their left, to become stationary for a short period of time. This stationary behavior propagates to the left, in a wave-like manner. Moreover, the behavior is superimposed on the movement to the left displayed by these groups. (b) As time progresses, the groups remain stationary longer, and so, the temporal length of this wave increases. For example, the groups positioned at the right-end of the domain are stationary for about 120 time-steps. Eventually, the spatially nonhomogeneous solution will be formed only of high density stationary groups. The parameters are: $q_a = q_r = 0$, $q_{al} = 2.2$, $\lambda_1 = 0.667$, $\lambda_2 = 3.0$, $\gamma = 0.1, s_r = 0.25, s_{al} = 0.5, s_a = 1.0, m_r = s_r/8, m_{al} = s_{al}/8, m_a = s_a/8$. The simulations were run for $200,000$ time steps (up to time t=3900). Here we plot (a) some 300 time steps at the beginning of the simulations, and (b) the last 180 time steps.

Model	Travel. train	Travel. pulse	Stat. pulse	Zigzag pulse	Semi-zigzag pulse	Breather	Travel. breather	Feather	Ripples
M1	(b)	(c)	(a),(b),(c)	–	(b)	–	–	–	–
M2	(b),(c)	(b),(c)	(a),(c)	(c)	–	–	–	–	–
M3	(b)	(c)	–	–	–	–	–	(a),(c)	–
M4	(b)	(c)	(a),(b),(c)	(a),(c)	(b)	(a)	(a),(c)	–	–
M5	–	–	(b)	–	–	–	–	–	(a),(c)

Table 5.3: A summary of the different types of possible solutions exhibited by the five models, M1 - M5. Here (a), (b), and (c) represent the three discussed cases: (a) only attraction and repulsion, (b) only alignment, (c) attraction, repulsion, and alignment. The *dashes* mean that the pattern has not been observed. We focused on the parameter space where the wave numbers of the perturbations are unstable, as predicted by the linear stability analysis. However, since this parameter space is very large, we have sampled only some parameter subspaces. Case (a): fix $q_{al} = 0, \gamma = 0.1, \lambda_1 = 0.2, \lambda_2 = 0.9$, and $A = 2$. The sampled parameter subspace is (q_a, q_r), with $q_a, q_r \in [0.5, 9]$. For the initial conditions we consider $u^* = u^{**}$. Case (b): fix $q_a = q_r = 0, \gamma = 0.1, A = 2$, and investigate the influence of the turning rates on the group structure. For this, we define $\lambda_1 = 0.2/\tau$, $\lambda_2 = 0.9/\tau$, and vary τ. The sampled parameter subspace is (q_{al}, τ), with $q_{al} \in [0.5, 10]$, and $\tau \in [0.006, 1]$. For the initial conditions we take $u^* \neq u^{**}$. Case (c): fix $\gamma = 0.1, \lambda_1 = 0.2, \lambda_2 = 0.9, A = 2$. The sampled parameter subspace is (q_a, q_r), with $q_a, q_r \in [0.5, 10]$. For the initial conditions we consider $u^* = u^{**}$. The obtained patterns are robust to parameter changes, in the sense that each pattern is observed for range of parameters.

and repulsion greater than alignment), and $\lambda_1 = 0.2, \lambda_2 = 0.9$. The rest of the parameters are given in the caption of Figure 5.5. Models M1 and M2 yield stationary pulses, as shown in Figure 5.5, pattern (1). This suggests that for this particular case (i.e., $q_r, q_a > q_{al}$), it does not matter whether the signals received from within the alignment range come only from neighbors moving towards the reference individual (M1), or from neighbors moving in both directions (M2). Model M3 shows feathers, as in Figure 5.5, pattern (3). In this case, the group as a whole is stationary. However, those individuals positioned at the edge, facing away from the group, leave and do not turn around. This happens because the individuals do not receive information from behind. Model M4 shows traveling breathers, as in Figure 5.5, pattern (9). This behavior is the result of two factors. First, since repulsion has the same magnitude as attraction, individuals can escape the group. These individuals move faster than the rest of the group. The rest of the group executes a sort of zigzag (those very high density patches displayed by pattern (9)). Second, the boundary conditions are periodic. That is, individuals that have left the group now are joining it again. This leads to expanding and contracting moving groups (i.e., traveling breathers). Model M5 shows ripples, as in Figure 5.5, pattern (3). In this case, the individuals react only to signals coming from ahead. This way, when two left-moving and right-moving waves approach each other, the majority of individuals within each group turn around, to avoid collision. However, there are some individuals that continue moving in the same direction. This behavior leads to the appearance that the waves pass through one another.

5.5 Spatiotemporal patterns caused by drift in communication

The patterns shown in Table 5.3 are likely not the only possible patterns. There are two main reasons for this. First, we have focussed only on the five sub-models M1-M5. However, it is possible to consider different communica-

tion mechanisms and to derive corresponding sub-models. Second, we have not sampled the entire parameter space. It may be possible to obtain new patterns in different parameter subspaces. For example, as discussed in Chapter 2, one can consider an asymmetry in the communication mechanisms by assuming that the information received from the right is more intense than the information received from the left ($p_r > p_l$). The assumption makes sense if we consider environmental effects (e.g., the wind blowing from the right). Figure 5.7 shows some examples of spatiotemporal patterns obtained for models M1, M3, M4, and M5, when we assume a drift in communication: (a) traveling feathers, obtained for model M3; (b) traveling zigzags obtained for model M1; (c) a different type of traveling breathers, obtained for model M4; (d) traveling pulses, obtained for model M1, in the absence of alignment. Note that patterns (a), (b), and (c) are new.

In Sections 5.3 and 5.4, we have seen that in the absence of external stimuli, attractive and repulsive interactions alone cannot lead to a traveling pulse (see Tables 5.1 and 5.3). These results are consistent with the analysis presented in Chapter 3, when we investigated the effect of an odd kernel. There, we have seen that neither the hyperbolic system nor the limiting parabolic equation can display moving groups in the absence of alignment. However, for the parabolic equation (3.33), destroying the symmetry of the kernel by assuming a drift in the communication mechanism can make the groups move. Figure 5.7(d) suggests that a similar effect is obtained for the hyperbolic system (2.1). When $p_r = p_l = 1$, the group does not move (the resulting pattern being similar to the one shown in Figure 5.5 (2)). However, when $p_r = 1.1$ and $p_l = 0.9$, the group does move (as shown in Figure 5.7(d)). Comparing these two patterns, we conclude that in the absence of alignment, asymmetry in the reception of signals can lead to moving groups.

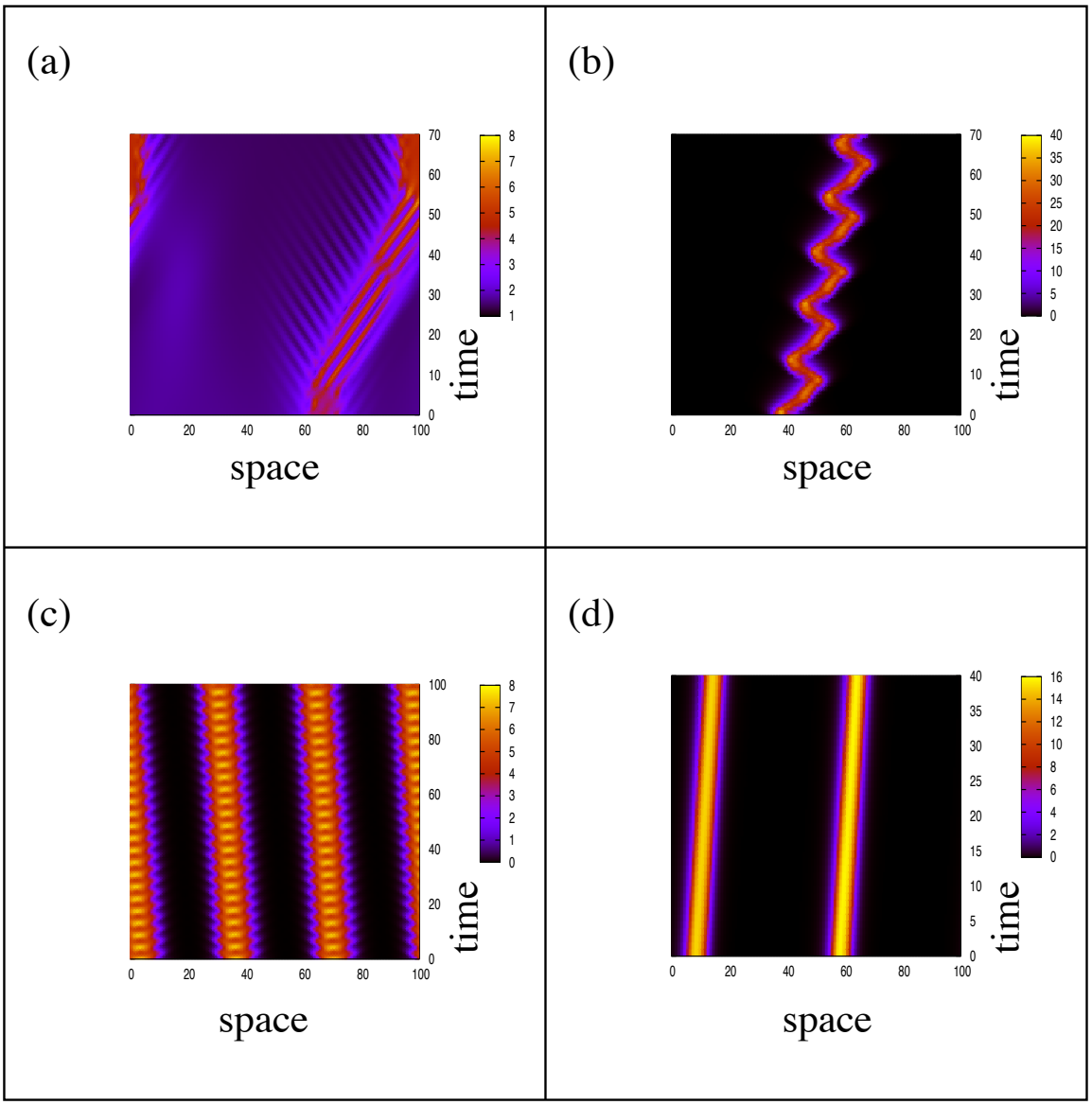

Figure 5.7: Examples of patterns obtained when we assume asymmetric communication. In the following, we choose $p_r = 1.10$, $p_l = 0.9$. (a) traveling feathers, obtained for model M3; $q_{al} = 2.0$, $q_a = 1.91$, $q_r = 2.05$, $\lambda_1 = 0.2$, $\lambda_2 = 0.9$. (b) traveling zigzags obtained for model M1; $q_r = 1.2$, $q_a = 15.0$, $q_{al} = 2.0$, $\gamma = 0.1$, $\lambda_1 = 0.2$, $\lambda_2 = 0.9$. (c) a different type of traveling breathers, obtained for model M4; $q_{al} = 0$, $q_a = 2$, $q_r = 1$, $\lambda_1 = 0.2$, $\lambda_2 = 0.9$. (d) traveling pulse, obtained for model M1, in the absence of alignment; $q_{al} = 0$, $q_a = 2.4$, $q_r = 0.1$, $\lambda_1 = 0.2$, $\lambda_2 = 0.9$.

5.6 Discussion

In this chapter, we investigated numerically the spatial and spatiotemporal patterns displayed by the hyperbolic system (2.1). Since the one-dimensional models existent in the literature consider either only attractive and repulsive social interactions, or only alignment interactions, we studied the patterns that occur in three different cases: (a) only attractive and repulsive interactions; (b) only alignment interactions; (c) attractive, repulsive, and alignment interactions. We showed that alignment is a necessary ingredient for the movement in the absence of external environmental cues. More precisely, attraction and repulsion alone lead to stationary groups. However, when alignment is included, moving groups are possible. An alternative to including alignment is to consider an environmental drift, which induces asymmetry in the reception of signals. This assumption, too, can lead to moving groups.

We also investigated the patterns obtained considering different communication sub-models. The results show at least 13 different emergent patterns. We should note that the described new patterns hold scientific interest. To our knowledge, some of these patterns (e.g., feathers) have never been previously observed. The results also show that the way organisms receive information may play a central role in the emergence of complex patterns observed in biological aggregations.

In this chapter, we performed simulations with two types of kernels: odd kernels and translated Gaussian kernels. Comparing the patterns obtained in Section 5.3 with the patterns displayed by model M1 in Section 5.4, we observe that the long-time behavior is similar, no matter what type of kernels we use. In both cases, we obtain stationary pulses, traveling pulses, traveling trains, and zigzag pulses.

Also, we have studied the transitions between different daily activities, as the model parameters are varied. This is the first time that transitions are studied in the context of a continuum model. Similar transition results were previously obtained with an individual-based model [24].

To verify that the patterns are not artifacts of the periodic boundary condi-

tions, we also performed simulations with homogeneous Neumann, Dirichlet, and open boundary conditions (not shown here). For Neumann boundary conditions, it was not possible to obtain traveling trains, or traveling pulses, both of which require an infinite domain. However, the other patterns were qualitatively similar to those obtained with periodic conditions. For Dirichlet and open boundary conditions, the results were similar only for a quite short period of time, until the moving groups leave the domain.

In the following chapter, we will investigate analytically some of these patterns. The linear analysis performed in Chapter 4 gives conditions on the parameters that determine when the steady states become linearly unstable and form spatial and spatiotemporal patterns. The spatially homogeneous solutions that become unstable when $\sigma(k) > 0$ are eventually bounded by nonlinear terms. It is precisely these terms that determine the final patterns we have investigated numerically in this chapter. In Chapter 6, we will take into consideration these nonlinear terms and use them to derive amplitude equations that govern the behavior of the solutions for large time. In particular, we will use weakly nonlinear theory to understand the mechanisms involved in the formation of these patterns.

Chapter 6

Weakly nonlinear analysis of the model

6.1 Introduction

The results of the previous chapter show that the hyperbolic model (2.1) displays a wide variety of complex spatial and spatiotemporal patterns. In the following[1], we will investigate the mechanisms involved in the formation of some of these patterns.

The linear stability analysis we discussed in Chapter 4 is only valid for small time and infinitesimal perturbations. For large time, the nonlinear terms dominate the growth of the unstable modes. To study the influence of these nonlinear terms on the final heterogeneous pattern, we will employ the classical method of weakly nonlinear analysis (see [74, 119]). It is weakly nonlinear since, although it incorporates the nonlinear terms, it only involves perturbation about the critical points obtained through linear stability [117]. This analysis has been originally developed in a fluid dynamics context (e.g., the Bénard problem [74]). However, the method is now widely applied in different areas, such as physics [9], mathematical biology [68, 88, 117], etc. The method uses separate time scales to study how the amplitude of the heterogeneous so-

[1] A version of this chapter has been submitted for publication.

R. Eftimie, G. de Vries, M. A. Lewis, (2007) *Weakly nonlinear analysis for a hyperbolic model for animal group formation*, J. Math. Biol.

lution varies with time. More precisely, there is a fast time scale and a slow time scale. The fast time scale is represented by the initial time region (t), where the solution starts to develop. This is the time scale where the linear stability analysis is valid. The slow time scale is represented by a second time region ($T = \epsilon^2 t$), where the effects of the nonlinear terms become important. Here, the amplitude of these heterogeneous patterns varies slowly. The two time variables t and T are considered to be independent as ϵ approaches zero.

In the following, we will focus on one of the communication sub-models proposed in Chapter 2, namely model M1, with interaction kernels defined by (2.9). We will investigate the mechanisms that lead to the formation of some of the patterns displayed by this model. In Section 5.4, we showed that this particular model can display at least four different spatial and spatiotemporal patterns (see Table 5.3, and Figure 5.5): stationary pulses, traveling trains, semi-zigzag pulses, and traveling pulses. Here, we will investigate the emergence of two of these patterns: stationary pulses and traveling trains. Both patterns occur near bifurcation points of the spatially homogeneous steady states. The semi-zigzag pulses are a temporal transition from traveling trains to stationary pulses. The fourth pattern, traveling pulses, seems to occur far from the bifurcation point.

Figure 6.1 shows two patterns that emerge through a real bifurcation ((a) and (b)), and two patterns that emerge through an imaginary bifurcation ((c) and (d)). Figure 6.1(a) corresponds to a single stationary pulse obtained for large attractive interactions (q_a). Figure 6.1(b) corresponds to multiple stationary pulses which are obtained for large turning rates (λ_2). Figure 6.1(c) corresponds to a traveling train formed of one peak, obtained for large attraction. Figure 6.1(d) corresponds to a traveling train formed of 17 peaks, and obtained for large turning rates. As mentioned in Chapter 5, we define a traveling train to be a pattern that doubles the number of its peaks when we double the domain size. A traveling pulse, on the other hand, has the same number of peaks when we double the domain size. By this definition, the pattern shown in Figure 6.1(c) is a traveling train, since doubling the domain size leads to the formation of two moving groups.

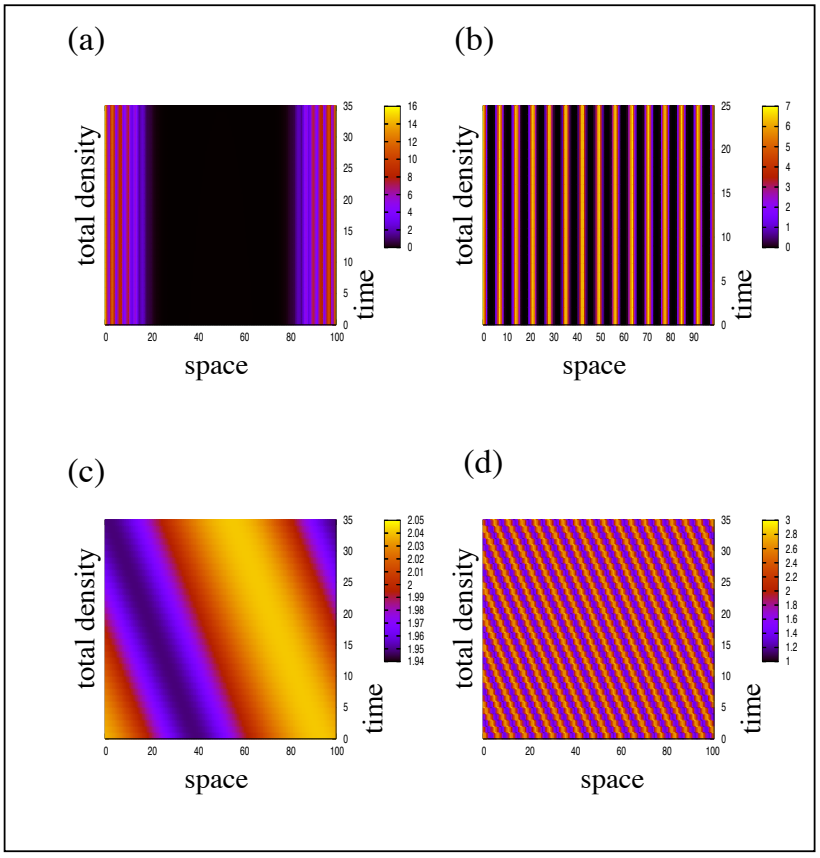

Figure 6.1: Patterns exhibited by model M1. Shown is the total density $u(x,t) = u^+(x,t) + u^-(x,t)$. (a) Stationary pulses; $q_a = 0.93$, $q_r = 2.2$, $q_{al} = 0$, $\lambda_1 = 0.2$, $\lambda_2 = 0.9$, $\gamma = 0.1$. (b) Stationary pulses; $q_r = q_a = 0$, $q_{al} = 0.85$, $\lambda_1 = 2.0$, $\lambda_2 = 9.0$, $\gamma = 0.1$. (c) Traveling train; $q_a = 1.0$, $q_r = 0.1$, $q_{al} = 2.45$, $\lambda_1 = 0.2$, $\lambda_2 = 0.9$. (c) Traveling trains; $q_a = q_r = 0$, $q_{al} = 2.08$, $\lambda_1 = 0.2/0.7$, $\lambda_2 = 0.9/0.7$, $\gamma = 0.1$.

In Sections 6.2 and 6.3, we focus on the situation when the bifurcation occurs at a real eigenvalue, as seen in Figure 4.3(a) at $q_a = q_a^0$, and in Figure 4.3(b) at $q_{al} = q_{al}^0$. Here, the focus will be on the spatially homogeneous steady state $(u^*, u^{**}) = (u_3^*, u_3^*)$. We first analyze system (2.1) when only attractive and repulsive interactions are present (that is, $q_r, q_a \neq 0$, $q_{al} = 0$). In this case, we know from the results in Chapter 5 that it is possible to obtain stationary heterogeneous patterns, such as the single stationary pulse shown in Figure 6.1(a). At the end of Section 6.3, we will briefly discuss the case when $q_a = q_r = 0$ and $q_{al} \neq 0$. In this case, it is possible to obtain multiple stationary pulses, such as those shown in Figure 6.1(b).

In Sections 6.4 and 6.5, we will study a bifurcation that occurs at a purely imaginary eigenvalue, as seen in Figure 4.3 (b) at q_{al}^1, and in Figure 4.3 (c) at q_{al}^0). Now, the focus will be on the steady state $(u^*, u^{**}) = (u_1^*, u_5^*)$. To keep the results tractable, we will consider the situation when alignment is the only social interaction (that is, $q_{al} \neq 0$, $q_a = q_r = 0$). In this case, we obtain spatiotemporal patterns described by traveling trains, as shown in Figure 6.1(d). At the end of Section 6.5, we will briefly discuss the situation when we include repulsive and attractive interactions. The traveling train pattern that results in this case is shown in Figure 6.1(c).

We should specify that throughout this chapter, we will ignore the steady states (u_2^*, u_4^*) and (u_4^*, u_2^*). First, as seen in Chapter 4, these states are always unstable. Moreover, the numerical simulations suggest that the solutions perturbed from u_2^* and u_4^* go to the same attractor as the solutions perturbed from the other three steady states (u_1^*, u_3^*, and u_5^*).

6.2 Weakly nonlinear analysis in the neighborhood of a real bifurcation

In this section, we will consider only attractive and repulsive social interactions (that is, $q_{al} = 0$). The only spatially homogeneous steady state is $(u^*, u^{**}) = (A/2, A/2)$. We are interested in the stability of this steady state as we increase

the magnitude of attraction (q_a). Let us denote by q_a^0 the critical value of q_a for which the dispersion relation satisfies $\sigma(q_a^0, k_c) = 0$ (the case is depicted in Figure 4.2(a) and Figure 4.3(a)). Let $k = k_c$ be the critical wave number. A solution of (2.1) near the bifurcation point is given by

$$u^{\pm}(x,t) \propto e^{\sigma t + ik_c x} + \text{c.c.}, \tag{6.1}$$

where "c.c." stands for "complex conjugate". We perform a perturbation analysis in a neighborhood of the critical value (q_a^0):

$$q_a = q_a^0 + \nu\epsilon^2, \;\; 0 < \epsilon \ll 1, \;\; \nu = \pm 1. \tag{6.2}$$

Writing the dispersion relation in a power series about q_a^0, namely

$$\sigma(q_a, k_c) = \sigma(q_a^0, k_c) + \frac{\partial \sigma(q_a^0, k_c)}{\partial q_a}\epsilon^2\nu + O(\epsilon^4), \tag{6.3}$$

and substituting it into (6.1), gives us

$$e^{\sigma(q_a,k_c)t + ik_c x} = e^{ik_c x + \frac{d\sigma(q_a^0,k_c)}{dq_a}\nu\epsilon^2 t} \approx e^{ik_c x}\alpha(\epsilon^2 t). \tag{6.4}$$

The amplitude α depends on the slow time $\epsilon^2 t$. This suggests we introduce a new time variable $T = \epsilon^2 t$ and consider fast and slow time scales, t^* and T, respectively:

$$t \to t^* + T.$$

In the limit $\epsilon \to 0$ we treat these two time scales as being independent [84]. We denote $\tilde{u}^{\pm}(x, t^*, \epsilon, T) = u^{\pm}(x,t)$. For notational simplicity, we drop the asterisk and the tilde, and assume the following formal expansion

$$\begin{aligned} u^+(x,t,\epsilon,T) &= u^* + \epsilon u_1^+ + \epsilon^2 u_2^+ + \epsilon^3 u_3^+ + O(\epsilon^4), \\ u^-(x,t,\epsilon,T) &= u^{**} + \epsilon u_1^- + \epsilon^2 u_2^- + \epsilon^3 u_3^- + O(\epsilon^4). \end{aligned} \tag{6.5}$$

Throughout this chapter, we consider the turning rates to be defined by equation (2.4). We then expand the nonlinear function $\tanh(y^{\pm}[u^+, u^-] - y_0) = \tanh(y^{\pm}[u^*, u^{**}] + \sum_j \epsilon^j y^{\pm}[u_j^+, u_j^-] - y_0)$ in a Taylor series about $y^{\pm}[u^*, u^{**}]$. The turning functions (2.2) can therefore be written as

$$\begin{aligned} \lambda^{\pm} &= L_{1,2} + P_{1,2}\sum_j \epsilon^j y^{\pm}[u_j^+, u_j^-] + S_{1,2}(\sum_j \epsilon^j y^{\pm}[u_j^+, u_j^-])^2 + \\ &\quad T_{1,2}(\epsilon^j \sum_j y^{\pm}[u_j^+, u_j^-])^3 + O(\epsilon^4), \;\; j = 1, 2, 3..., \end{aligned} \tag{6.6}$$

with $L_{1,2}$ and $P_{1,2}$ defined by (4.13), and

$$
\begin{aligned}
S_1 &= \frac{\lambda_2}{2}\tanh(M_1-y_0)\left(1-\tanh^2(M_1-y_0)\right),\\
S_2 &= \frac{\lambda_2}{2}\tanh(-M_1-y_0)\left(1-\tanh^2(-M_1-y_0)\right),\\
T_1 &= \frac{\lambda_2}{12}\left(-(1-\tanh(M_1-y_0)^2)^2+4\tanh(M_1-y_0)^2(1-\tanh(M_1-y_0)^2)\right),\\
T_2 &= \frac{\lambda_2}{12}\left(-(1-\tanh(-M_1-y_0)^2)^2+4\tanh(-M_1-y_0)^2(1-\tanh(-M_1-y_0)^2)\right).
\end{aligned}
$$

Since we consider $q_{al}=0$, this implies that $M_1=0$, $L_1=L_2$, $P_1=P_2$, $S_1=S_2$, and $T_1=T_2$.

The nonlinear system (2.1) can be written as

$$\mathbf{N}(\mathbf{u})=0, \tag{6.7}$$

with $\mathbf{u}=(u^+,u^-)^T$. Substituting expressions (6.5)-(6.6) into this equation leads to $\mathbf{N}(\sum_{j=1}\epsilon^j\mathbf{u}_j)=\sum_j \mathbf{N}_j(\mathbf{u}_j)\epsilon^j$. At each $O(\epsilon^j)$, we can write $\mathbf{N}_j(\mathbf{u}_j)=L(\mathbf{u}_j)-N_j-E_j$. Here $L(\mathbf{u}_j)$ represents the linear part of the system (2.1), N_j contains the nonlinear terms formed of $u^\pm_{j-1}$, $u^\pm_{j-2}$, etc., and E_j contains the slow time derivatives $\partial_T u^\pm_{j-2}, (j\geq 3)$ and the terms multiplied by ν. The linear operator L is the same at each $O(\epsilon^j)$ step, whereas N_j and E_j have to be calculated every time. Therefore, $\mathbf{N}_j(\mathbf{u}_j)=0$ reduces to

$$L(\mathbf{u}_j)=N_j+E_j,\quad j=1,2,3,.... \tag{6.8}$$

Since the eigenvalues are real, the spatially homogeneous steady state becomes linearly unstable to spatial patterns, and therefore, the linear operator L is defined as

$$L(\mathbf{u})=\begin{pmatrix} \gamma\partial_x+L_1+M_5K*\cdot & -L_1+M_5K*\cdot \\ -L_1-M_5K*\cdot & -\gamma\partial_x+L_1-M_5K*\cdot \end{pmatrix}\begin{pmatrix} u^+\\ u^-\end{pmatrix}, \tag{6.9}$$

where the convolution $K*\cdot$ is defined by

$$K*u^\pm=q_r\left(\tilde{K}_r*u^\pm-K_r*u^\pm\right)-q_a^0\left(\tilde{K}_a*u^\pm-K_a*u^\pm\right), \tag{6.10}$$

with $\tilde{K}_{r,a}(s)=K_{r,a}(-s)$, and $(K_{r,a}*u^\pm)(x)=\int_{-\infty}^{\infty}K_{r,a}(s)u^\pm(x-s)ds$. Throughout the analysis, we will use the operator L_{k_c}, which is obtained by applying L to solutions of the form e^{ik_cx}:

$$L_{k_c}=\begin{pmatrix} \gamma ik_c+L_1+M_5\hat{K}^+(k_c) & -L_1+M_5\hat{K}^+(k_c) \\ -L_1-M_5\hat{K}^+(k_c) & -\gamma ik_c+L_1-M_5\hat{K}^+(k_c)\end{pmatrix}. \tag{6.11}$$

Here we define

$$\hat{K}^+(k_c) = q_r \left(\hat{\tilde{K}}_r^+(k_c) - \hat{K}_r^-(k_c) \right) - q_a^0 \left(\hat{\tilde{K}}_a^+(k_c) - \hat{K}_a^-(k_c) \right), \tag{6.12}$$

where $\hat{K}_j^{\pm}$, $j = r, a$ are the Fourier transforms (4.14). Later, we will also use $\hat{K}^-(k_c) = -\hat{K}^+(k_c)$, $\hat{K}^+(2k_c)$, and $\hat{K}^-(2k_c) = -\hat{K}^+(2k_c)$. At $O(\epsilon^1)$, the nonlinear terms are $N_1 = E_1 = 0$, and therefore, equation (6.7) reduces to solving

$$L(\mathbf{u_1}) = 0, \tag{6.13}$$

where $\mathbf{u_1} = (u_1^+, u_1^-)^T = \alpha(T)\mathbf{v}e^{ik_c x} + \text{c.c.}$, with $\mathbf{v} = (v_1, v_2)^T$, and "c.c." denoting the complex conjugate terms. The components v_1 and v_2 are given by:

$$v_1 = \frac{L_1 - M_5\hat{K}^+}{\gamma ik + L_1 + M_5\hat{K}^+}, \quad v_2 = 1. \tag{6.14}$$

The linear equation (6.13) has a nontrivial solution. Therefore, for $O(\epsilon^j)$, $j \geq 2$, the nonlinear equation (6.8) has a solution if and only if $N_j + E_j$ satisfies the Fredholm alternative [106]. Hence, $N_j + E_j$ has to be orthogonal to the bounded solution of the adjoint homogeneous problem

$$L^*(\hat{\mathbf{u}}) = 0. \tag{6.15}$$

Let us consider this solution $\hat{\mathbf{u}} = (\hat{u}^+, \hat{u}^-)^T$ to be defined by

$$\hat{\mathbf{u}} = \beta_1(T)\mathbf{W}e^{ik_c x} + \beta_2(T)\bar{\mathbf{W}}e^{-ik_c x}. \tag{6.16}$$

Then, equation (6.15) results in

$$\bar{L}_{k_c}^T(\hat{\mathbf{u}}) = 0, \tag{6.17}$$

with the adjoint operator defined as

$$\bar{L}_{k_c}^T = \begin{pmatrix} -\gamma ik_c + L_1 + M_5\hat{K}^-(k_c) & -L_1 - M_5\hat{K}^-(k_c) \\ -L_1 + M_5\hat{K}^-(k_c) & \gamma ik_c + L_1 - M_5\hat{K}^-(k_c) \end{pmatrix}$$

In Chapter 2, we have seen that the solution is bounded in L^∞, which implies that it is also bounded in L^2 [110]. Throughout this section, as well as Section

6.4, we will assume that $u^+, u^- \in L^2(\Omega)$, where $\Omega = \{(x,\tau)|x \in [0,L], \tau \in [0,\infty)\}$. On this space, we define the following inner product

$$\langle \mathbf{v}, \mathbf{w} \rangle = \lim_{T\to\infty} \frac{1}{T} \int_0^T \int_0^{L=\frac{2\pi}{k_c}} (v^1 \bar{w}^1 + v^2 \bar{w}^2) dx d\tau, \tag{6.18}$$

with $\mathbf{v} = (v^1, v^2)^T, \mathbf{w} = (w^1, w^2)^T$. Moreover, u^+ and u^- are bounded on Ω. The orthogonality condition reads

$$\langle \hat{\mathbf{u}}, \overline{(\mathbf{N}_j + \mathbf{E}_j)} \rangle = 0. \tag{6.19}$$

We are interested only in those terms of $\mathbf{N}_i + \mathbf{E}_i$ that contain $e^{\pm ik_c x}$ since these terms give rise to secular solutions. However, these terms do not appear at $O(\epsilon^2)$. Here, the nonlinear terms are $E_2 = 0$, and

$$N_2 = \begin{pmatrix} u_1^+ P_1 K * u_1 + u_1^- P_1 K * u_1 \\ -u_1^+ P_1 K * u_1 - u_1^- P_1 K * u_1, \end{pmatrix}, \tag{6.20}$$

where K^+ is defined by (6.10). Actually, N_2 can be rewritten as

$$N_2 = \alpha^2(T) e^{2ik_c x} \mathbf{Q^{(1)}} + |\alpha|^2 \mathbf{Q^{(2)}} + \text{c.c.}, \tag{6.21}$$

with $\mathbf{Q^{(1)}} = (Q_1^{(1)}, Q_2^{(1)})^T$ and $\mathbf{Q^{(2)}} = (Q_1^{(2)}, Q_2^{(2)})^T$ described by

$$Q_1^{(1)} = P_1 (v_1 + v_2)^2 \hat{K}^+, \quad Q_2^{(1)} = -Q_1^{(1)}, \tag{6.22}$$

$$Q_1^{(2)} = |v_1 + v_2|^2 (\hat{K}^+ + \hat{K}^-), \quad Q_2^{(2)} = -Q_1^{(2)}. \tag{6.23}$$

Hence, N_2 does not contain terms of the form $e^{\pm ik_c x}$. Equation $L(\mathbf{u_2}) + N_2 = 0$ is then solved for $\mathbf{u_2} = (u_2^+, u_2^-)^T$, where

$$\mathbf{u_2} = \alpha_1(T) \mathbf{v_0} e^{ik_c x} + \alpha^2(T) \mathbf{v^{(1)}} e^{2ik_c x} + |\alpha|^2 \mathbf{v^{(2)}} + \text{c.c.}, \tag{6.24}$$

with $\mathbf{v^{(1)}} = (v_1^{(1)}, v_2^{(1)})^T$, and $\mathbf{v^{(2)}} = (v_1^{(2)}, v_2^{(2)})^T$ satisfying the following two equations

$$L_{2k_c}(\mathbf{v^{(1)}}) + \mathbf{Q^{(1)}} = 0, \tag{6.25}$$

$$L_0(\mathbf{v^{(2)}}) + \mathbf{Q^{(2)}} = 0. \tag{6.26}$$

Solving system (6.25) gives us

$$v_1^{(1)} = \frac{-Q_1^{(1)}}{2\gamma i k + 2M_5 \hat{K}_2^+}, \quad v_2^{(1)} = v_1^{(1)}. \tag{6.27}$$

Here we define $\hat{K}_2^+ = q_r(\hat{\tilde{K}}_r^+(2k_c) - \hat{K}_r^-(2k_c)) - q_a^0(\hat{\tilde{K}}_a^+(2k_c) - \hat{K}_a^-(2k_c))$. System (6.26) reduces to one equation in two unknowns. To solve it for $v_1^{(2)}$ and $v_2^{(2)}$, we have to impose the conservation of the total density on the interval $[0, L] = [0, \frac{2\pi}{k_c}]$. This condition requires that $v_2^{(2)} = -v_1^{(2)}$. We therefore have

$$v_1^{(2)} = \frac{-Q_1^{(2)}}{2L_1}, \quad v_2^{(2)} = -v_1^{(2)}. \tag{6.28}$$

At $O(\epsilon^3)$, we obtain terms that can lead to secular solutions. In this case, the nonlinear interactions $N_3 + E_3$ are described by

$$\begin{aligned} N_3 + E_3 &= \frac{\partial \alpha}{\partial T} e^{ik_c x} \mathbf{R^{(3)}} + \frac{\partial \bar{\alpha}}{\partial T} e^{-ik_c x} \bar{\mathbf{R}}^{(3)} + \alpha e^{ik_c x} \nu \mathbf{R^{(2)}} + \bar{\alpha} e^{-ik_c x} \nu \bar{\mathbf{R}}^{(2)} + \\ &\quad \alpha |\alpha|^2 e^{ik_c x} \mathbf{R^{(1)}} + \bar{\alpha} |\alpha|^2 e^{-ik_c x} \bar{\mathbf{R}}^{(1)} + \text{other terms}, \end{aligned} \tag{6.29}$$

where "other terms" describe those terms of the form $e^{\pm 2ik_c x}, e^{\pm 3ik_c x}$, etc. The coefficients $\mathbf{R}^{(j)}, j = 1, 2, 3$, are described by the following expressions:

$$\begin{aligned} R_1^{(1)} &= P_1 \bar{v} v^{(1)} \hat{K}^- + P_1 v v^{(2)} \hat{K}^+ + P_1 \bar{v} v^{(1)} \hat{K}_2^+ + S_1 (\bar{v}_1 - \bar{v}_2) v^2 (\hat{K}^+)^2 + \\ &\quad 2 S_1 \bar{v} v (v_1 - v_2) \hat{K}^+ \hat{K}^- + 3 T_1 A \hat{v} v^2 \hat{K}^- (\hat{K}^+)^2, \\ R_2^{(1)} &= -R_1^{(1)}, \\ R_1^{(2)} &= -M_5 v (\hat{\tilde{K}}_a - \hat{K}_a^+)(k_c), \\ R_2^{(2)} &= -R_1^{(2)}, \\ R_1^{(3)} &= v_1, \\ R_2^{(3)} &= v_2. \end{aligned} \tag{6.30}$$

We define here $v = v_1 + v_2$, and $v^{(1)} = v_1^{(1)} + v_2^{(1)}$. The solution $\mathbf{W}$ of the adjoint equation (6.17) is given by

$$W_1 = 1, \quad W_2 = \frac{\gamma i k - L_1 - M_5 \hat{K}^-(k_c)}{-L_1 - M_5 \hat{K}^-(k_c)}. \tag{6.31}$$

Then, the orthogonality condition (6.19) can be written as

$$\begin{aligned} \lim_{T \to \infty} \frac{1}{T} \int_0^T \int_0^{\frac{2\pi}{k_c}} &(\beta_1(T) \mathbf{W} e^{ik_c x} + \beta_2(T) \bar{\mathbf{W}} e^{-ik_c x}) \left(\mathbf{R^{(1)}} \alpha |\alpha|^2 e^{ik_c x} + \bar{\mathbf{R}}^{(1)} \bar{\alpha} |\alpha|^2 e^{-ik_c x} \right. \\ &\left. + \mathbf{R^{(2)}} \alpha \, e^{ik_c x} \nu + \bar{\mathbf{R}}^{(2)} \bar{\alpha} e^{-ik_c x} \nu + \mathbf{R^{(3)}} \frac{d\alpha}{dT} e^{ik_c x} + \bar{\mathbf{R}}^{(3)} \frac{d\bar{\alpha}}{dT} e^{-ik_c x} \right) dx dT = 0. \end{aligned}$$

Since $\int_0^{\frac{2\pi}{k_c}} e^{\mp 2ik_c x} dx = 0$, we obtain

$$\bar{\mathbf{W}} \cdot \mathbf{R^{(1)}} \alpha |\alpha|^2 + \bar{\mathbf{W}} \cdot \mathbf{R^{(2)}} \alpha \nu + \bar{\mathbf{W}} \cdot \mathbf{R^{(3)}} \frac{d\alpha}{dT} = 0, \tag{6.32}$$

and its complex-conjugate

$$\mathbf{W} \cdot \bar{\mathbf{R}}^{(1)} \bar{\alpha} |\alpha|^2 + \mathbf{W} \cdot \bar{\mathbf{R}}^{(2)} \bar{\alpha} \nu + \mathbf{W} \cdot \bar{\mathbf{R}}^{(3)} \frac{d\bar{\alpha}}{dT} = 0. \tag{6.33}$$

Equation (6.32) can be rewritten as

$$\frac{d\alpha}{dT} = -\nu \alpha Y - \alpha |\alpha|^2 X, \tag{6.34}$$

where

$$Y = \frac{\bar{\mathbf{W}} \cdot \mathbf{R^{(2)}}}{\bar{\mathbf{W}} \cdot \mathbf{R^{(3)}}}, \quad X = \frac{\bar{\mathbf{W}} \cdot \mathbf{R^{(1)}}}{\bar{\mathbf{W}} \cdot \mathbf{R^{(3)}}}. \tag{6.35}$$

We can verify that

$$Y = \frac{d\sigma}{dq_a} = \frac{\gamma i k M_5 (\hat{K}_a^+ - \hat{K}_a^-)}{L_1}. \tag{6.36}$$

Therefore the linear approximation of this amplitude equation agrees with the linear prediction given by the dispersion relation (equation (6.3)).

The amplitude equation (6.34) is complex. To obtain a real equation, let us define $\alpha(T) = R(T) e^{i\theta(T)}$, with real terms $R(T) = |\alpha|$ and $\theta(T)$. Thus, equation (6.34) can be rewritten as

$$\frac{dR}{dT} = -\nu R \Re(Y) - R^3 \Re(X), \tag{6.37}$$

$$\frac{d\theta}{dT} = -\nu \Im(Y) - R^2 \Im(X), \tag{6.38}$$

with $\Re$ and $\Im$ denoting the real and imaginary parts of the two coefficients X and Y. The two steady-state solutions of (6.37) are $R = 0$ and $R = \sqrt{-\nu \Re(Y)/\Re(X)}$. To study the stability of these solutions, we write $R = R_0 + R_\delta$, where R_0 is the steady state and R_δ is a small perturbation. Equation (6.37) then becomes

$$\frac{dR_\delta}{dT} = R_\delta \left(-\nu \Re(Y) - 2R_0^2 \Re(X) \right). \tag{6.39}$$

We can observe that the trivial state $R_0 = 0$ is stable if $\nu \Re(Y) > 0$, and unstable otherwise. The nontrivial state $R_0 = \sqrt{-\nu \Re(Y)/\Re(X)}$ is unstable if $\nu \Re(Y) > 0$, and stable otherwise.

To compare the results of the nonlinear analysis with the numerical results, we substitute α into the expressions for $u_1^{\pm}$, and derive a formula for the actual amplitude of the spatial patterns:

$$\max(u)-\min(u) = \epsilon(\max(u_1^+ + u_1^-) - \min(u_1^+ + u_1^-)) = \epsilon 4\Re((v_1+v_2)\alpha). \quad (6.40)$$

The dashed curve in Figure 6.2 shows the variation of the amplitude for the stationary pulses described in Figure 6.1(a). For $u_3^* = A/2 = 1$, $q_r = 2.2$, $q_{al} = 0$, $\gamma = 0.1$, $\lambda_1 = 0.2$, $\lambda_2 = 0.9$, the bifurcation to spatial patterns occurs at $q_a^0 = 1.008$. The coefficients that appear in the amplitude equation (6.34) are both negative: $\Re(X) < 0$, $\Re(Y) < 0$. Therefore, when $\nu = -1$, the curve $|\alpha|^2 = -\nu\Re(Y)/\Re(X) > 0$ is unstable, while $|\alpha| = 0$ is stable. Hence, the nonzero amplitude (the dashed curve) bifurcates subcritically to the left. In the next section, we perform numerical simulations to verify these analytical results.

6.3 Numerical results for a real bifurcation

To verify the results of this weakly nonlinear analysis, we perform numerical simulations. The numerical scheme we use is the second-order McCormack scheme described in Section 5.1. The initial conditions are perturbations of the spatially homogeneous steady states (u^*, u^{**}) with terms of the form $0.02\cos(k_c\pi x)$, $x \in [0, L]$. For the parameter values specified in the previous section, the final heterogeneous pattern is similar to the one described in Figure 6.1(a). Figure 6.2 shows the amplitude of the total density, as determined by $\max(u^+ + u^-) - \min(u^+ + u^-)$. The solid circles represent the stable numerical solution, while the open circles represent the unstable numerical solution.

For $q_a > q_a^0$, the spatially homogeneous steady state ($|\alpha| = 0$) bifurcates numerically to a large amplitude solution (solid circles). However, as we decrease q_a, we observe hysteresis behavior: the solution does not return to the spatially homogeneous steady state when $q_a = q_a^0$. It will eventually return to this steady state for some $q_a < q_a^0$. This is consistent with the previous analytical results regarding the existence of an unstable amplitude that bifurcates

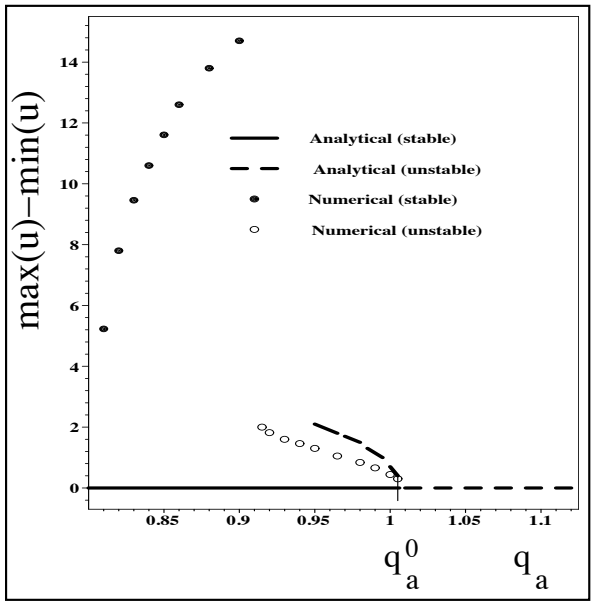

Figure 6.2: The amplitude of the spatially heterogeneous solution $u(x,t) = u^+(x,t) + u^-(x,t)$ as we perturb the magnitude of attraction q_a. The dashed curves represent the unstable branch obtained using the weakly nonlinear analysis. The solid circles represent the stable branch obtained numerically, whereas the open circles represent the unstable branch obtained numerically. The critical value of q_a is $q_a^0 = 1.008$. The other parameters are: $\lambda_1 = 0.2$, $\lambda_2 = 0.9$, $\gamma = 0.1$, $q_r = 2.2$, $q_{al} = 0$, $y_0 = 2$. For $q_a < q_a^0$, the zero amplitude branch (corresponding to $|\alpha^2| = 0$) is stable (continuous line). For $q_a > q_a^0$ it becomes unstable (dashed line). When $q_a < q_a^0$, the curve formed by the open circles marks the boundary of the stability region, as determined numerically. Perturbations with amplitude on or above this curve grow to the upper branch (solid circles), while perturbations with amplitude below this curve decay to zero.

subcritically. We checked numerically the existence of this branch by choosing the initial conditions to be perturbations of the spatially homogeneous steady states with terms of the form $\hat{A}\cos(k_c\pi x)$, where $\hat{A}$ is the variable amplitude. For $q_a < q_a^0$, the curve formed of open circles represents the unstable branch. This curve represents a threshold: perturbations with amplitude $\hat{A}$ on or above this curve grow until the solution reaches the upper stable branch, whereas perturbations with amplitude below this curve decay to zero. Since the spatially homogeneous steady state is $(u_3^*, u_3^*) = (1, 1)$, imposing the condition that the initial solution is positive, forces us to use $\hat{A} \leq 2$. This happens for $q_a \in [0.915, 1.008]$.

There are two remarks regarding Figure 6.2. First, it is known that for subcritical bifurcations, the cubic amplitude equation (6.34) can give only a qualitative behavior of the solutions [25]. However, this qualitative behavior is enough for the biological questions we want to address in this thesis. We note here that for $q_a < q_a^0$, the two unstable curves (the analytical and the numerical one) agree acceptably well, especially near the bifurcation point. Second, the high-amplitude solution drops to zero far from the bifurcation point (i.e., at $q_a = 0.83$). However, the weakly-nonlinear analysis does not hold near the point where the solution drops to zero. Therefore, we do not expect here the stable high-amplitude curve and the unstable analytical curve to match. To study the behavior of the solution far from the bifurcation point, one can derive "phase equations" [87].

Figure 6.2 can be used to investigate the effect of attraction on the structure of stationary groups. Since the bifurcation is subcritical, the stable high-amplitude solution gives us the effect of the attractive interactions. More precisely, we notice that increasing the strength of the attraction (q_a) leads to larger amplitudes for the total density u. This means more compact groups. Moreover, for attraction less than q_a^0, solutions with amplitude less than $\sqrt{-\nu\Re(Y)/\Re(X)}$ will decay. This suggests that groups that have a density less than a certain threshold will eventually disperse. Of course, this threshold depends not only on q_a, but also on all other parameters.

If we now consider $q_r = q_a = 0$ and large turning rates (λ_1, λ_2), we obtain

similar results. However, in this case, the bifurcation parameter is the magnitude of alignment q_{al}. The final heterogeneous pattern is described in Figure 6.1(b). Figure 6.3 shows the amplitude of the stationary pattern that bifurcates subcritically to the left at $q_{al}^0 = 0.845$. Therefore, when the individual turning rates are very large, but at the same time organisms align with their neighbors, increasing the strength of alignment leads to higher amplitude solutions. Again, this means that the groups become more compact. Moreover, there is a similar threshold for the total density below which the groups will disperse.

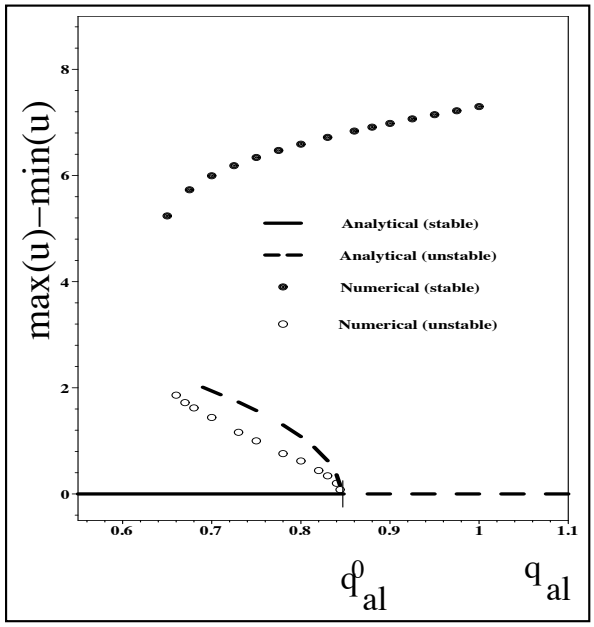

Figure 6.3: The amplitude of the spatially heterogeneous solution $u(x,t) = u^+(x,t) + u^-(x,t)$ as we perturb the magnitude of alignment q_{al}. The solid circles represent the stable branch obtained numerically, while the open circles represent the unstable branch obtained numerically. The dashed curve represents the unstable branch obtained using weakly nonlinear analysis. For $q_{al} < q_{al}^0$, the zero amplitude branch (corresponding to $|\alpha^2| = 0$) is stable (the continuous curve). For $q_a > q_a^0$ it becomes unstable (the dashed curve). The parameters are: $q_{al}^0 = 0.845$, $k_c = k_{14} = 8.867$, $\lambda_1 = 2.0$, $\lambda_2 = 9.0$, $\gamma = 0.1$, $q_r = 0$, $q_a = 0$, $y_0 = 0$.

6.4 Weakly nonlinear analysis in the neighborhood of an imaginary bifurcation

In the following, we consider the case when the bifurcation to spatial heterogeneous patterns occurs at an imaginary eigenvalue. To keep the results tractable, we will assume that alignment is the only social interaction (that is, $q_a = q_r = 0$). This corresponds to the pattern shown in Figure 6.1(d). Consequently, we will fix all other parameters and assume that the bifurcation to spatially nonhomogeneous patterns occurs as q_{al} passes through a critical value q_{al}^0. At the critical point (q_{al}^0, k_c), the two eigenvalues of the dispersion relation (4.12) are $\sigma_1(q_{al}^0, k_c) = i\omega$, and $\sigma_2(q_{al}^0, k_c) = \omega_0 + i\omega$, with $\omega_0 < 0$. As mentioned before, this happens when the spatially homogeneous steady state is any of the pairs (u_1^*, u_5^*), or (u_5^*, u_1^*). Throughout this section, we will assume that $(u^*, u^{**}) = (u_1^*, u_5^*)$ and study what happens in this case. Since the second eigenvalue has always a negative real part, we ignore it and focus only on the first eigenvalue. A solution of system (2.1) near the bifurcation point (q_{al}^0, k_c) has the form

$$u^{\pm}(x,t) \propto e^{i\omega t + ik_c x} + \text{c.c.} \tag{6.41}$$

As before, we perturb q_{al} away from the critical value q_{al}^0,

$$q_{al} = q_{al}^0 + \epsilon^2 \nu, \;\; 0 < \epsilon \ll 1, \;\; \nu = \pm 1.$$

Note that the spatially homogeneous steady state (u_3^*, u_3^*), which we discussed in the previous section, does not depend on the bifurcation parameter. However, as shown in Figure 4.3 (b) and (c), the spatially homogeneous steady state (u_1^*, u_5^*) does depend on the magnitude of alignment (q_{al}): as we increase q_{al}, u^* increases while u^{**} decreases. Therefore, in this case, a perturbation of q_{al} will induce a perturbation of these steady states:

$$u^* = u_0^* - \epsilon^2 \nu \left| \frac{du^*(q_{al}^0)}{dq_{al}} \right|, \quad u^{**} = u_0^{**} + \epsilon^2 \nu \left| \frac{du^*(q_{al}^0)}{dq_{al}} \right|, \tag{6.42}$$

where

$$\frac{\partial u^*(q_{al}^0)}{\partial q_{al}} = -\frac{M_5(u^{**} - u^*)}{L_1 + L_2 - 2q_{al}^0 M_5}, \tag{6.43}$$

and the constants L_1, L_2 and M_5 are given by (4.13). For notational simplicity, we will drop the index "0" from the spatially homogeneous steady states u_0^* and u_0^{**}. Therefore, the left- and right-moving densities can be written as

$$\begin{aligned} u^+(x,t,\epsilon,T) &= u^* - \epsilon^2\nu|\frac{du^*(q_{al}^0)}{dq_{al}}| + \epsilon u_1^+ + \epsilon^2 u_2^+ + \epsilon^3 u_3^+ + O(\epsilon^4), \\ u^-(x,t,\epsilon,T) &= u^{**} + \epsilon^2\nu|\frac{du^*(q_{al}^0)}{dq_{al}}| + \epsilon u_1^- + \epsilon^2 u_2^- + \epsilon^3 u_3^- + O(\epsilon^4). \end{aligned} \tag{6.44}$$

Expanding the dispersion relation in power series leads to

$$\sigma(q_{al}, k_c) = \sigma(q_{al}^0, k_c) + \frac{\partial\sigma(q_{al}^0, k_c)}{\partial q_{al}}\epsilon^2\nu + O(\epsilon^4). \tag{6.45}$$

To calculate the $O(\epsilon^2)$ term that appears in equation (6.45), we use equation (4.12):

$$\frac{\partial\sigma(q_{al}^0, k_c)}{\partial q_{al}} = \frac{-i\omega\frac{\partial C(q_{al}^0,k_c,u^*)}{\partial q_{al}} - \frac{\partial D(q_{al}^0,k_c,u^*)}{\partial q_{al}}}{2i\omega + C(q_{al}^0, k_c, u^*)}. \tag{6.46}$$

Because u^* and $u^{**} = A - u^*$ depend on q_{al}, the terms $\frac{\partial C}{\partial q_{al}}$ and $\frac{\partial D}{\partial q_{al}}$ are given in terms of the derivative of u^* with respect to q_{al}. Hence, when $\sigma(q_{al}^0, k_c) = i\omega$, we obtain

$$\frac{\partial\sigma}{\partial q_{al}} = \frac{-(u^{**}-u^*)P - M_7\Delta - \frac{2q_{al}^0(u^{**}-u^*)M_5}{L1+L2-2q_{al}^0M_5}\left(P + \Delta(P1 - P2 - 4q_{al}^0(u^*S_1 - u^{**}S_2))\right)}{2i\omega + L1 + L2 - M_5q_{al}^0(\hat{K}_{al}^+ + \hat{K}_{al}^-)}, \tag{6.47}$$

where

$$\begin{aligned} P &= P_1(i\omega - \gamma ik_c) - P_2(i\omega + \gamma ik_c), \\ \Delta &= \hat{K}_{al}^+(i\omega + \gamma ik_c) + \hat{K}_{al}^-(i\omega - \gamma ik_c), \\ M_7 &= M_5 + 2q_{al}^0(u^{**} - u^*)(u^*S_1 - u^{**}S_2), \end{aligned} \tag{6.48}$$

while the rest of the constants are given by (4.13).

Since the eigenvalues are imaginary, the spatially homogeneous steady states become unstable to *spatiotemporal patterns*, and therefore, the linear operator associated to system (2.1) is given by

$$L(\mathbf{u}) = \begin{pmatrix} \partial_t + \gamma\partial_x + L_1 + M_5q_{al}^0K_{al} * \cdot & -L_2 + M_5q_{al}^0K_{al} * \cdot \\ -L_1 - M_5q_{al}^0K_{al} * \cdot & \partial_t - \gamma\partial x + L_2 - M_5q_{al}^0K_{al} * \cdot \end{pmatrix} \begin{pmatrix} u^+ \\ u^- \end{pmatrix}. \tag{6.49}$$

However, throughout the analysis, we will use L_{ω,k_c} which is obtained by applying the operator L to solutions of the form ($e^{i\omega t+ik_cx}$):

$$L_{\omega,k_c}=\begin{pmatrix} i\omega+\gamma ik_c+L_1-M_5q_{al}^0\hat{K}_{al}^- & -L_2+M_5q_{al}^0\hat{K}_{al}^+ \\ -L_1+M_5q_{al}^0\hat{K}_{al}^- & i\omega-\gamma ik_c+L_2-M_5q_{al}^0\hat{K}_{al}^+ \end{pmatrix}. \tag{6.50}$$

The corresponding adjoint operator $\bar{L}^T_{\omega,k_c}$ is described by

$$\bar{L}^T_{\omega,k_c}=\begin{pmatrix} -i\omega-\gamma ik_c+L_1+M_5q_{al}^0\hat{K}_{al}^+ & -L_1-M_5q_{al}^0\hat{K}_{al}^+ \\ -L_2+M_5q_{al}^0\hat{K}_{al}^- & -i\omega+\gamma ik_c+L_2-M_5q_{al}^0\hat{K}_{al}^- \end{pmatrix}. \tag{6.51}$$

As in Section 6.2, we start collecting the terms with equal powers of ϵ. At $O(\epsilon)$ we have

$$\mathbf{u_1}=\alpha\mathbf{v}e^{i\omega t+ik_cx}+c.c., \tag{6.52}$$

where $\alpha=\alpha(T)$, $\mathbf{u_1}=(u_1^+,u_1^-)^T$, and $\mathbf{v}=(v_1,v_2)^T$=$((-i\omega+\gamma ik_c)/(i\omega+\gamma ik_c),1)^T$. At $O(\epsilon^2)$, $\mathbf{E_2}=0$ and

$$\mathbf{N_2}=\begin{pmatrix} (u_1^+P_1+u_1^-P_2)q_{al}^0K_{al}*(u_1^--u_1^+)+(u^*S_1-u^{**}S_2)(q_{al}^0)^2(K_{al}*(u_1^--u_1^+))^2 \\ -(u_1^+P_1+u_1^-P_2)q_{al}^0K_{al}*(u_1^--u_1^+)-(u^*S_1-u^{**}S_2)(q_{al}^0)^2(K_{al}*(u_1^--u_1^+))^2 \end{pmatrix}.$$

After some calculations, we can rewrite the nonlinear terms $\mathbf{N_2}+\mathbf{E_2}$ as

$$\mathbf{N_2}+\mathbf{E_2}=\alpha^2e^{2i\omega t+2ik_cx}\mathbf{Q^{(1)}}+\bar{\alpha}^2e^{-2i\omega t-2ik_cx}\mathbf{Q^{(2)}}+|\alpha|^2\mathbf{Q^{(3)}}. \tag{6.53}$$

Therefore, the solution of the nonlinear problem $L(\mathbf{u_2})=\mathbf{N_2}+\mathbf{E_2}$ can be written as

$$\mathbf{u_2}=\alpha_1\mathbf{v_0}e^{i\omega t+ik_cx}+\alpha^2e^{2i\omega t+2ik_cx}\mathbf{G_0^{(1)}}+\bar{\alpha}^2e^{-2i\omega t-2ik_cx}\mathbf{G_0^{(2)}}+|\alpha|^2\mathbf{G_0^{(3)}}.$$

The constants $\mathbf{G_0^{(j)}}, j=1,2,3$, are calculated by requiring them to verify the following equations:

$$L_{2\omega,2k_c}\mathbf{G_0^{(1)}} = -\mathbf{Q^{(1)}},\ L_{-2\omega,-2k_c}\mathbf{G_0^{(2)}}=-\mathbf{Q^{(2)}},\quad L_{0,0}\mathbf{G_0^{(3)}}=-\mathbf{Q^{(3)}}. \tag{6.54}$$

The equation for $\mathbf{N_2}$+$\mathbf{E_2}$ does not contain terms of the form $e^{\pm i\omega t\pm ik_cx}$, and therefore the Fredholm Alternative is satisfied. However, at $O(\epsilon^3)$ we have to impose the

condition that the solution verifies the Fredholm Alternative. Let us define the solution of the adjoint homogeneous problem to be $\hat{\mathbf{u}}= \beta_1(T)\mathbf{V}e^{i\omega t+ik_c x}+c.c.$. This leads to the amplitude equation,

$$\frac{d\alpha}{dT} = -\nu\alpha Y - \alpha|\alpha|^2 X, \tag{6.55}$$

where

$$Y = \frac{\bar{\mathbf{V}}\cdot\mathbf{R^{(2)}}}{\bar{\mathbf{V}}\cdot\mathbf{R^{(3)}}}, \quad X = \frac{\bar{\mathbf{V}}\cdot\mathbf{R^{(1)}}}{\bar{\mathbf{V}}\cdot\mathbf{R^{(3)}}}. \tag{6.56}$$

The coefficients $\mathbf{R^{(j)}}, j = 1, 2, 3$, that appear in this equation are given by

$$\begin{aligned}
R_1^{(1)} &= v_1, \\
R_2^{(1)} &= v_2, \\
R_1^{(2)} &= (M_5 + 2q_{al}^0(u^{**}-u^*)(u^*S_1 - u^{**}S_2))b_1 + (u^{**}-u^*)e_1 + 2q_{al}^0 e_1 + q_{al}^0 J_{11}b_1 - \\
&\quad q_{al}^0(P_1 - P_2 - 4q_{al}^0(u^*S_1 - u^{**}S_2)b_1), \\
R_2^{(2)} &= -R_1^{(2)}, \\
R_1^{(3)} &= 2(u^*S_1 - u^{**}S_2)(q_{al}^0)^2(b_1 G_0^{(3)} + \bar{b}_1 G_0^{(1)}) + 3(u^*T_1 + u^{**}T_2)(q_{al}^0)^3(b_1)^2\bar{b}_1 + \\
&\quad q_{al}^0(e_1 G_0^{(3)} + \bar{e}_1 G_0^{(1)}) + (q_{al}^0)^2(\bar{f}_1(b_1)^2 + 2f_1 b_1\bar{b}_1) + q_{al}^0(J_1\bar{b}_1 + J_9 b_1), \\
R_2^{(3)} &= -R_1^{(3)}.
\end{aligned} \tag{6.57}$$

We define here

$$\begin{aligned}
b_1 &= \hat{K}_{al}^+ v_2 - \hat{K}_{al}^- v_1, \quad e_1 = P_1 v_1 + P_2 v_2, \quad f_1 = S_1 v_1 - S_2 v_2, \\
J_j &= G_1^{(j)} P_1 + G_2^{(j)} P_2, \quad j = 1..10, \\
G_0^{(1)} &= G_{0_2}^{(1)}\hat{K}_{al}^+(2k_c) - G_{0_1}^{(1)}\hat{K}_{al}^-(2k_c), \quad G_0^{(2)} = G_{0_2}^{(2)}\hat{K}_{al}^-(2k_c) - G_{0_1}^{(2)}\hat{K}_{al}^+(2k_c), \\
G_0^{(3)} &= G_{0_2}^{(3)} - G_{0_1}^{(3)}.
\end{aligned} \tag{6.58}$$

After some lengthy computations, we can verify that

$$Y = \frac{d\sigma(q_{al}^0)}{dq_{al}}, \tag{6.59}$$

with $\frac{d\sigma}{dq_{al}}$ given by equation (6.47). Therefore the linear approximation of this amplitude equation agrees with the linear prediction given by the dispersion relation (equation (6.45)).

Similar to the results presented in Section 6.2, the steady-state solutions for the magnitude of the amplitude equation are given by

$$|\alpha| = 0, \;\; |\alpha| = \sqrt{-\nu\Re(Y)/\Re(X)}. \tag{6.60}$$

The zero state $|\alpha| = 0$ is stable if $\nu\Re(Y) > 0$, and unstable otherwise. The state $|\alpha| = \sqrt{-\nu\Re(Y)/\Re(X)}$ is unstable if $\nu\Re(Y) > 0$, and stable otherwise.

For $q_r = q_a = 0$, $\lambda_1 = 0.2/0.7$, $\lambda_2 = 0.9/0.7$, $\gamma = 0.1$, and $k_c = k_{17} = 10.55$, the two coefficients that appear in equation (6.60) are $\Re(Y) > 0$ and $\Re(X) < 0$. Hence $|\alpha|^2 = -\nu\frac{\Re(Y)}{\Re(X)} > 0$ if $\nu > 0$, which means that solution bifurcates to the right. Moreover, since $\nu\Re(Y) > 0$, the zero-amplitude steady state is stable, whereas the nonzero-amplitude solution is unstable. Figure 6.4 shows this bifurcation. The continuous curve represents the stable solution, whereas the dashed curve represents the unstable solution obtained using weakly nonlinear analysis.

6.5 Numerical results for the imaginary bifurcation

To confirm the validity of these results, we perform numerical simulations. Again, the initial conditions are perturbations of the spatially homogeneous steady states with terms of the form $\hat{A}cos(k_c\pi x)$. Figure 6.4 shows the amplitude of the spatiotemporal solutions as we perturb the magnitude of alignment q_{al}. As before, the spatial homogeneous solution bifurcates subcritically to spatial heterogeneous solutions represented by the traveling trains (seen in Figure 6.1(d)). The solid circles represent the stable numerical solution, while the open circles represent the unstable numerical solution. For $q_{al} \geq q_{al}^0$, the branch described by the open circles represents a threshold: perturbations with amplitude below this curve decay to zero, while perturbations with amplitude on or above this curve grow to the upper branch. Therefore, the numerical results are consistent with the analytical results.

We notice that increasing the magnitude of alignment leads to a slight decrease

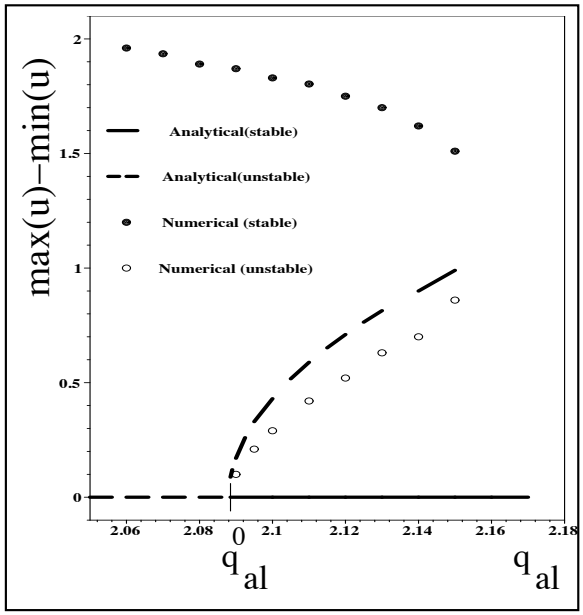

Figure 6.4: Amplitude of the spatially heterogeneous solution as we perturb the magnitude of alignment q_{al}. The solid circles represent the stable numerical solution, while the open circles represent the unstable numerical solution. The continuous curve represents the stable analytical solution, while the dashed curve represents the unstable analytical solution. The critical value of q_{al} is $q_{al}^0 = 2.088$. The other parameters are: $\lambda_1 = 0.2/0.7$, $\lambda_2 = 0.9/0.7$, $\gamma = 0.1$, $q_r = q_a = 0$, $L = 10.12$, $k_c = 10.55$, $y_0 = 2$.

in the amplitude of the solutions. This suggests that moving groups become more elongated, as alignment is increased. This is opposite to the effect observed in the case of stationary groups. There, the alignment makes the group more compact. As before, there is a certain threshold for the total density, corresponding to $|\alpha|^2 = -\nu \frac{\Re(Y)}{\Re(X)}$. Groups with total density greater than this threshold will become more dense and persist for a long time, while groups with the density below this threshold will disperse.

As mentioned in Chapter 4, introducing attractive and repulsive interactions leads to the emergence of the first wave number, k_1, as shown in Figure 4.2 (a). In this case, the result is a traveling train formed only of one group (see Figure 6.1(c)). Figure 6.5 shows the subcritical bifurcation obtained in this case. The stable high-amplitude branch (the solid circles) corresponds to the solution shown in Figure 6.1(c). The effect of alignment on the moving group is similar to the previous case.

6.6 Discussion

In this chapter, we have analyzed two spatial and spatiotemporal patterns displayed by model M1, introduced in Chapter 2. The investigated patterns are stationary pulses and traveling trains. We have performed a weakly nonlinear analysis to study the amplitudes of these two patterns. The stationary pulses arise through a real bifurcation from the spatially homogeneous steady state (u_3^*, u_3^*). The traveling trains arise through an imaginary bifurcation from a different steady state, namely (u_1^*, u_5^*). In both cases, the bifurcations are subcritical. It should be mentioned that while the steady state (u_3^*, u_3^*) is constant, the steady state (u_1^*, u_5^*) depends on the bifurcation parameter.

It is known that for subcritical bifurcations, the unstable branch obtained using a cubic amplitude equation gives only qualitative information about the solution [25]. A more accurate result can be obtained by adding higher-order terms to obtain a quintic amplitude equation. Moreover, far from the bifurcation point, one can only

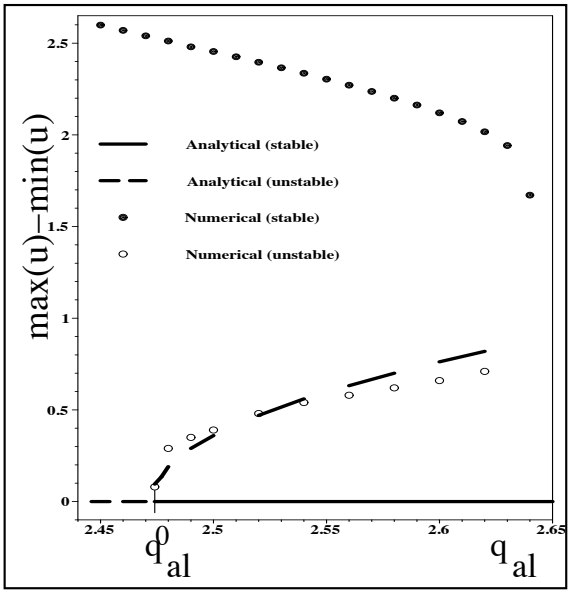

Figure 6.5: The amplitude of the spatially heterogeneous solution as we perturb the magnitude of alignment q_{al}, while taking into consideration the attractive and repulsive interactions. The solid circles represent the stable numerical solution, while the open circles represent the unstable numerical solution. The dashed curves represent the unstable analytical solution. The critical value of q_{al} is $q_{al}^0 = 2.472$. The other parameters are: $\lambda_1 = 0.2$, $\lambda_2 = 0.9$, $\gamma = 0.1$, $q_r = 0.1$, $q_a = 1.0$, $L = 10$, $k_c = 0.628$, $y_0 = 2$.

derive "phase equations" to study the behavior of the solution. However, due to the complexity of our system, as well as the type of questions we are addressing (that is, the effect of the social interactions on the amplitude of spatial and spatiotemporal patterns), it is sufficient to derive a cubic amplitude equation.

We then used the bifurcation diagrams for the amplitude of the solutions to study the effect of social interactions on the structure of the aggregations. As expected, increasing inter-individual attraction leads to more compact stationary groups. This kind of behavior can be observed in schools of fish [18, 116], when a nearby predator leads to increased attraction towards neighbors which causes the group to form very tight stationary aggregations. On the other hand, alignment has dual effects, depending on whether the group is stationary or moving. We have seen that in the case of stationary groups with high individual turning rates, alignment has an aggregative effect, with the groups becoming more dense. However, in case of moving groups, the effect of alignment is opposite: the density decreases as the groups become more elongated. When alignment becomes very large, the groups disintegrate. However, empirical observations of fish schools show that highly polarized groups are tight [98, 131]. Nevertheless, it is clear that moving groups have to be less dense than the stationary compact groups because of the need for manoeuvering.

The subcritical bifurcation suggests that there is a threshold group density, such that groups with densities below this threshold will disperse, while groups with densities above this threshold will become even more dense and persist for a longer time. This transition between the disordered behavior represented here by the homogeneous solution, and the ordered behavior represented by the high-density stationary or moving groups, is particularly important for the area of animal group formation and movement. It is known that some insect species (such as ants [8], or locusts [17]), and fish (such as young Tilapia fish [6]), exhibit transitions between disordered and ordered activity behaviors, and these transitions depend on animal density. For example, Buhl et. al. [17] have shown experimentally and

numerically (using an individual-based model) that as the density of locusts in a group increases, there is a transition from disordered movement to collective motion of aligned groups. Understanding such transitions has potential applications to understanding and controlling the outbreaks of different insect pests, such as locusts.

Here, we have analyzed the patterns displayed by only one of the five sub-models described in Chapter 2. It is possible that other patterns, corresponding to the other four sub-models, arise through supercritical bifurcations (i.e., bifurcation to a small, stable, amplitude solution). However, this aspect has not yet been investigated. Still, we can conclude that the subcritical bifurcations seem to play an important role in the understanding of the effects of biological parameters to the formation and persistence of certain animal groups (such as insects). A supercritical bifurcation would suggest that increasing a certain parameter would lead to the formation of denser, well coordinated groups. This may be the case for some animal groups, but not necessarily for insects like locusts or ants. A subcritical bifurcation, on the other hand, suggests the existence of a density threshold below which well coordinated groups cannot persist. Moreover, this type of bifurcation helps us connect the threshold for the total animal density to different behaviors. More precisely, this threshold depends on different parameter values which characterize different group behaviors.

In the previous five Chapters (2 to 6), we have investigated the case when the individuals move at a constant speed and turn in response to the signals received from their neighbors. In the following chapter, we will focus on a new model which assumes that individuals speed up or slow down in response to their neighbors' behavior. In particular, we will compare the resulting spatial and spatiotemporal patterns obtained with this new model, to the patterns obtained with the model introduced in Chapter 2.

Chapter 7

Possible alternative models with density-dependent speed

7.1 Introduction

Throughout the previous five chapters we assumed that individuals move with a constant speed and turn to approach, to avoid, or to align with their neighbors. This approach is consistent with other Eulerian [59, 71, 99, 100] and Lagrangian models [50, 126] for animal group formation and movement. However, organisms do not always move with a constant speed [58]. They speed up or slow down to catch up with their neighbors, or to avoid collisions. This, in addition to turning in response to their neighbors' behaviors.

In the mathematical literature, there are many examples of local and nonlocal parabolic models for animal movement that consider density-dependent velocities (see for example [67, 77, 80, 122, 123], and the references therein). There are also some local hyperbolic models which assume that individuals speed up or slow down in response to local population density and its gradient [54, 70]. However, there are no one-dimensional continuum models which assume that both the speed and the turning rates have a nonlocal character. This generalization makes perfect sense since if individuals can speed up or slow down as a result of the interactions with neighbors far away (as in [80], for example), they can also turn as a result of these interactions. In the following, we will address this issue by starting with the model

we introduced in Chapter 2, and then incorporating attractive and repulsive interactions into the individuals' speed.

In Section 7.2, we carefully describe this new hyperbolic model with density-dependent speed and turning rates. In particular, we will focus on two cases: (a) the turning rates depend only on alignment interactions, and (b) the turning rates depend on all three social interactions, namely attraction, repulsion, and alignment. In the first case, the speeding behavior is separated from the turning behavior. In the second case, the two behaviors are coupled through the attractive and repulsive interactions. In Section 7.3, we take a formal parabolic limit to investigate the connection between this model and other parabolic models with density-dependent speed that exist in the literature. In this context, we compare the limiting parabolic equations corresponding to cases (a) and (b). In Section 7.4, we perform a linear stability analysis of the model, and further investigate the differences between these two cases in terms of the emerging wave numbers. Then, in Section 7.5, we investigate numerically some of the spatial and spatiotemporal patterns obtained with this new hyperbolic model. We conclude with a discussion in Section 7.6.

7.2 Model derivation

In this section, we derive an alternative model for the situation when the speed depends on attractive and repulsive interactions. For simplicity, we focus here on the particular communication mechanism discussed in Chapter 2, namely model M1. More precisely, we assume that for attractive and repulsive interactions, individuals use information received from all neighbors. For alignment, on the other hand, individuals use only the information received from those neighbors moving towards them.

The general model describing the movement of right-moving (u^+) and left-

moving (u^-) individuals is given by the following equations:

$$\begin{aligned}
\partial_t u^+(x,t) + \partial_x(\Gamma^+[u^+,u^-]u^+(x,t)) &= -\lambda^+[u^+,u^-]u^+(x,t) + \lambda^-[u^+,u^-]u^-(x,t), \\
\partial_t u^-(x,t) - \partial_x(\Gamma^-[u^+,u^-]u^-(x,t)) &= \lambda^+[u^+,u^-]u^+(x,t) - \lambda^-[u^+,u^-]u^-(x,t), \\
u^\pm(x,0) &= u_0^\pm(x), x \in \mathbf{R}. \qquad (7.1)
\end{aligned}$$

where $\Gamma^\pm[u^+,u^-]$ are the density-dependent speeds, and $\lambda^\pm[u^+,u^-]$ are the density-dependent turning rates. The turning rates have already been described in Chapter 2, Section 2.2. Here, we will focus on the speed and consider it to be a positive, bounded, and increasing function of the perceived signals (see Figure 7.1). Such an example is the function $1+\tanh(y^\pm)$, where $y^\pm$ denote the perceived signals (see also the discussion in Section 2.2). In particular, we assume that the speed depends on the communication signals received from neighbors positioned within the attractive and repulsive interaction ranges (that is, $y^\pm = y_a^\pm - y_r^\pm$). For example, in case of attraction, individuals speed up to join a larger group in front of them, or slow down to allow those behind them to catch up. In case of repulsion, individuals slow down to avoid collision with those in front of them, or speed up to avoid collision with those behind them. Throughout this chapter, we will assume that the nonlocal speeds are described by the following terms:

$$\begin{aligned}
\Gamma^+[u^+,u^-] &= \gamma\left(1+\tanh\left(q_a\int_0^\infty K_a(s)\left(u(x+s,t)-u(x-s,t)\right)ds\right.\right. \\
&\qquad \left.\left. -q_r\int_0^\infty K_r(s)\left(u(x+s,t)-u(x-s,t)\right)ds\right)\right), \\
\Gamma^-[u^+,u^-] &= \gamma\left(1+\tanh\left(-q_a\int_0^\infty K_a(s)\left(u(x+s,t)-u(x-s,t)\right)ds\right.\right. \\
&\qquad \left.\left. +q_r\int_0^\infty K_r(s)\left(u(x+s,t)-u(x-s,t)\right)ds\right)\right). \qquad (7.2)
\end{aligned}$$

As in the previous chapters, $u(x \pm s,t) = u^+(x \pm s,t) + u^-(x \pm s,t)$ describes the total density at $(x \pm s,t)$, while q_a and q_r represent the magnitudes of attractive and repulsive interactions. Also, we choose γ to be a constant "base-line" speed. If there is no attraction or repulsion, $\tanh(0) = 0$ and therefore, the individuals move at a constant speed γ (as assumed in Chapter 2). When the attractive or repulsive

interactions play a role, the speed varies between 0 and 2γ. To understand equations (7.2), let us focus for example on the attractive interactions, and assume that the signals received by a right-moving individual (u^+) from neighbors positioned ahead, at $x+s$, are becoming more intense than the signals received from neighbors positioned behind, at $x-s$. This means that the attractive term is positive: $q_a \int_0^\infty K_a(s)(u(x+s,t)-u(x-s,t))ds > 0$. Therefore Γ^+ is increasing, which implies that this right-moving individual will speed up to join the neighbors that are ahead. If, on the other hand, the signals received from behind are more intense than those received from ahead, the integral is negative. Therefore, this individual will slow down to allow those neighbors behind him to catch up. A similar explanation holds for the repulsion term. However, since this term has a negative sign in front of it, the effect is opposite.

Similarly, one can describe the speeding behavior of a left-moving individual (the second equation of (7.2)). To complete the description of equations (7.2), it should be mentioned that the interaction kernels $K_{r,a,al}$ are described by the translated Gaussian kernels (2.9) (see Section 2.2).

In Chapter 2, we assumed that the turning rates $\lambda^{\pm}[u^+, u^-]$ depend an all three social interactions: attraction, repulsion, and alignment. Here, we consider attractive and repulsive speeds, and for the turning rates we investigate the following two cases:

(a) individuals turn only to align with neighbors within the alignment range;

(b) individuals turn to avoid collision with neighbors within the repulsion range, to approach neighbors within the attraction range, or to align with those neighbors within the alignment range.

Since both cases are defined in terms of the same communication mechanism, namely model M1, we will refer to case (a) as model $M1_I$, and to case (b) as model $M1_{II}$. Table 7.1 summarizes all these models.

Note that for model $M1_I$, the speed and the turning rates are independent from each other. The speed acts on the spatial ranges for attractive and repulsive inter-

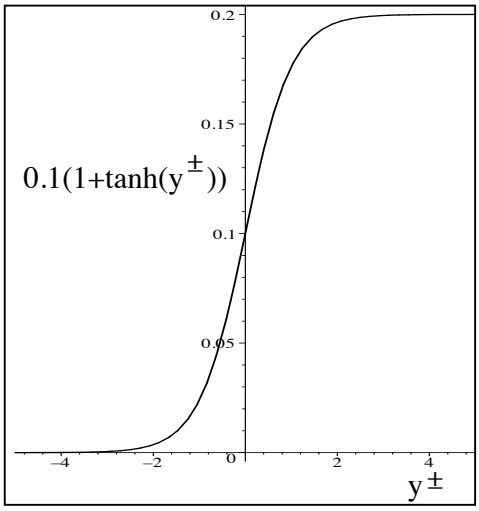

Figure 7.1: The speed function $\Gamma^{\pm}[u^+, u^-] = \gamma(1 + \tanh(y^{\pm}[u^+, u^-]))$ (shown here is $\gamma = 0.1$). As in Chapter 2, $y^{\pm}$ denote the signals received as a result of social interactions: $y^{\pm} = y_a^{\pm} - y_r^{\pm}$ (where $y_a^{\pm}$ and $y_r^{\pm}$ describe the attractive and repulsive interactions, respectively). When there are no attractive and repulsive interactions, $y^{\pm} = 0$ and the speed is constant (γ). When the social interactions play an important role (i.e., $y^{\pm} \neq 0$), the speed varies between 0 and 2γ.

actions, while the turning rates act on the spatial range for alignment interactions. However, for model $M1_{II}$, the speed and the turning rates are not independent anymore. They are connected through the attractive and repulsive interactions. To understand this connection, let us focus on the behavior of a right-moving individual $u^+(x,t)$. In particular, let us assume that we are within the attraction range. If the signals received from neighbors positioned at $x+s$ are more intense than the signals received from neighbors positioned at $x-s$ (that is, $u(x+s,t) - u(x-s,t) > 0$), then the individual located at x will keep moving in the same direction (since λ^+ is decreasing), and will speed up to approach the neighbors at $x+s$ (since Γ^+ is increasing). If, on the other hand, the signals coming from neighbors positioned at $x+s$ are less intense than the signals coming from those positioned at $x-s$ (that is, $u(x+s,t) - u(x-s,t) < 0$), the individual located at x will turn around (since λ^+ is increasing), and will slow down (since Γ^+ is decreasing). Now, the individual

Model	**Speed**	**Turning rates**
M1	$\Gamma = \pm\gamma$ =const.	$\lambda^{\pm} = \lambda^{\pm}\left(y_r^{\pm} - y_a^{\pm} + y_{al}^{\pm}\right)$
$M1_I$	$\Gamma = \Gamma^{\pm}[u^+, u^-]$	$\lambda^{\pm} = \lambda^{\pm}\left(y_{al}^{\pm}\right)$
$M1_{II}$	$\Gamma = \Gamma^{\pm}[u^+, u^-]$	$\lambda^{\pm} = \lambda^{\pm}\left(y_r^{\pm} - y_a^{\pm} + y_{al}^{\pm}\right)$

Table 7.1: A summary of the behaviors that can be influenced by the nonlocal social interactions. The speed Γ also depends on the nonlocal interactions: Γ=$\Gamma^{\pm}[u^+, u^-]$=$\Gamma(\pm y_a^{\pm} \mp y_r^{\pm})$. The terms $y_{r,a,al}^{\pm}$ are described by equations (2.5)-(2.8), when $p_r = p_l$ (see Chapter 2).

will be moving to the left (u^-). Because $u(x+s,t) - u(x-s,t) < 0$, the speed Γ^- is increasing, and the individual will be speeding up to join the neighbors at $x - s$. Therefore, two different processes, namely turning and speeding up/slowing down, determine the behavior of an individual through interactions with its neighbors that are within the attraction range. A similar explanation holds if we focus on the repulsion range.

7.3 Formal parabolic limit

In the following, we take a formal parabolic limit to investigate the connection between the hyperbolic model (7.1) and other parabolic models with density-dependent speed that exist in the literature. To investigate the parabolic limit of this hyperbolic system we assume, as in Chapter 3, that there is no alignment (that is, $q_{al} = 0$). Note that the attractive and repulsive interactions are defined in terms of the total density $u(x,t) = u^+(x,t)+u^-(x,t)$. Therefore the speed, as well as the turning rates, will depend only on this total density. Moreover, since the nonlocal speeds (7.2) are defined in terms of an odd function ($\tanh(y^{\pm}[u]) = \tanh(\pm y^+[u]) = \pm\tanh(y^+[u])$), we can write them as

$$\Gamma^+[u^+, u^-] = \gamma(1 + g[u]), \quad \Gamma^-[u^+, u^-] = \gamma(1 - g[u]), \tag{7.3}$$

where $g[u] = \tanh(y^+[u])$. Recall that the turning rates can be rewritten as $\lambda^{\pm}[u^+, u^-] = \lambda_1 + \lambda_2 f(y^{\pm}[u])$ (see equation 2.2).

Adding and subtracting the first two equations in (7.1), leads to the following system:

$$\begin{aligned} u_t + (\gamma v + \gamma g[u]u)_x &= 0, \qquad (7.4) \\ v_t + (\gamma u + \gamma g[u]v)_x &= \alpha[u]u - \beta[u]v. \qquad (7.5) \end{aligned}$$

Here we define $v = u^+ - u^-$, $\alpha[u] = \lambda^-[u^+, u^-] - \lambda^+[u^+, u^-]$, and $\beta[u] = \lambda^-[u^+, u^-] + \lambda^+[u^+, u^-]$. Note that for model $M1_I$, the turning rates are $\lambda^+ = \lambda^- = const.$ (since $q_{al} = 0$), and therefore $\alpha[0] = 0$. In the following, we will focus on model $M1_{II}$ (that is, $\alpha[u] \neq 0$). If we differentiate the first equation of (7.5) with respect to t, and the second equation with respect to x, we obtain

$$\begin{aligned} u_{tt} + \gamma v_{xt} + \gamma (g[u]u)_{xt} &= 0, \\ v_{tx} + \gamma u_{xx} + \gamma (g[u]v)_{xx} &= (u\alpha[u])_x - v_x \beta[u] - v(\beta[u])_x. \qquad (7.6) \end{aligned}$$

Eliminating v_{tx} from these two equations, assuming that the flow v is zero at the boundaries, and using equation (7.4) to replace v with $v = \int^x (-\frac{1}{\gamma} u_t - (g[u]u)_x) dx$, and v_x with $v_x = -\frac{1}{\gamma} u_t - (g[u]u)_x$, we obtain the following second-order equation:

$$\begin{aligned} u_{tt} \quad + \quad & \gamma \left(g[u]u\right)_{xt} - \gamma^2 u_{xx} + \gamma (g[u])_{xx} \int^x (u_t) dx + \gamma^2 (g[u])_{xx} \int^x ((g[u]u)_x) dx + \\ & \gamma g[u] u_{tx} + \gamma^2 g[u] (g[u]u)_{xx} + 2\gamma (g[u])_x u_t + 2\gamma^2 (g[u])_x (g[u]u)_x + \\ & \gamma (u\alpha[u])_x + \beta[u] u_t + \gamma \beta[u] (g[u]u)_x + (\beta[u])_x \int^x (u_t) dx + \\ & \gamma (\beta[u])_x \int^x (g[u]u)_x) dx = 0 \qquad (7.7) \end{aligned}$$

We observe that when $g[u] = 0$, equation (7.7) reduces to equation (3.24). We now introduce a small dimensionless parameter ϵ, and set

$$\begin{aligned} &(a) \quad \lambda_1 = \frac{\lambda_1^0}{\epsilon^2}, \quad \lambda_2 = \frac{\lambda_2^0}{\epsilon^2}, \\ &(b) \quad \gamma = \frac{\gamma_0}{\epsilon}, \\ &(c) \quad f(y^{\pm}[u]) = \epsilon f^0(y^{\pm}[u]), \text{ and } g[u] = \epsilon g^0[u]. \qquad (7.8) \end{aligned}$$

This means that as $\epsilon \to 0$, (a) the individuals turn very frequently, and (b) move very fast. These two behaviors lead to (c): a reduced sensitivity to the environment. Note that (c) leads to the following scaling of the functionals $\alpha[u]$ and $\beta[u]$:

$$\alpha[u] = \frac{\lambda_2^0 \epsilon \alpha^0[u]}{\epsilon^2} = \frac{\lambda_2^0 \alpha^0[u]}{\epsilon}, \text{ with } \alpha^0[u] = f^0(y^-[u]) - f^0(y^+[u]), \quad (7.9)$$

$$\beta[u] = \frac{2\lambda_1^0 + 2\lambda_2^0 \epsilon \beta^0[u]}{\epsilon^2}, \text{ with } \beta^0[u] = f^0(y^-[u]) + f^0(y^+[u]). \quad (7.10)$$

Moreover, the speed is rescaled to

$$\Gamma^{\pm}[u^+, u^-] = \frac{\gamma_0}{\epsilon} + \gamma_0 g^0[u]. \quad (7.11)$$

Substituting these terms into (7.7), multiplying with ϵ^2, and taking the limit $\epsilon \to 0$, leads to the parabolic equation

$$u_t = D u_{xx} - B(\alpha^0[u]u)_x - \gamma_0 (g^0[u]u)_x, \quad (7.12)$$

where $D = \frac{\gamma_0^2}{2\lambda_1^0}$, and $B = \frac{\gamma_0 \lambda_2^0}{2\lambda_1^0}$. Note that for $q_a \gg q_r$, both $g^0[u]$ and $\alpha^0[u]$ are positive (see Figure 7.2). Similarly, for $q_a \ll q_r$, $g^0[u]$ and $\alpha^0[u]$ are both negative. Therefore, the nonlocal component of the individuals' speed, namely $g[u]$, gives rise to a drift which is added to the drift that results from the difference between the different turning rates: λ^+ and λ^-. This is true only for model $M1_{II}$. For model $M1_I$, $\alpha^0[u] = 0$ and therefore, the drift is caused only by the nonlocal component of the speed:

$$u_t = D u_{xx} - \gamma_0 (g^0[u]u)_x. \quad (7.13)$$

Also, recall that for model M1, the drift was caused only by the difference between the turning rates (see equation (3.30)).

Note that if we use "tanh" function to describe both the turning rates and the speed (see equations (2.4) and (7.2)), then the parabolic equations (3.30), (7.12), and (7.13) are qualitatively similar. It should be emphasized that the functions α and g have similar shapes: they are both bounded and increasing as functions of the perceived signals (see Figure 7.2). Therefore, for large speeds and large turning rates, it does not really matter if the social interactions influence only the turning

rates, only the speed, or both the turning rates and the speed. In all these cases, the behavior of the limiting parabolic equation is qualitatively similar.

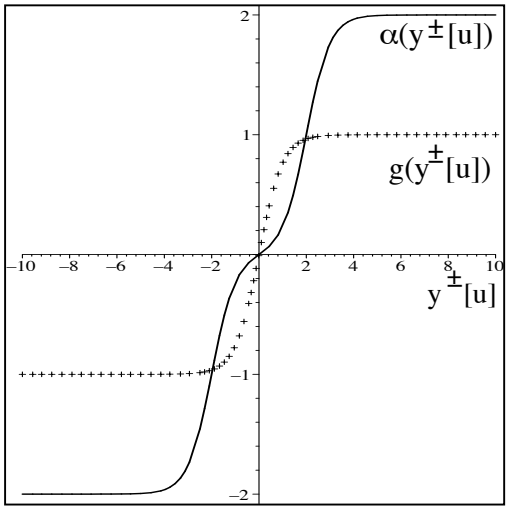

Figure 7.2: The nonlocal components for the speed and the turning rates functions. The continuous curve describes $g[u] = \tanh(y^{\pm}[u^+, u^-]) = \tanh(\pm y^{+}[u^+, u^-])$ (as a function of the perceived signals $y^{\pm}$). The curve formed of crosses describes the difference between the right and left turning $\alpha[u] = f(y^{\mp}[u] - y_0) - f(y^{\pm}[u] - y_0)$. Note that both functions are increasing and bounded.

Recall that in Chapter 3, we discussed conditions for the limiting parabolic equation that lead to moving groups. In particular, we started with a rectangular pulse and investigated the speed of the front and back edges. The results showed that in order to have moving groups, the function describing the nonlocal interactions has to be monotone. Following the same approach as there, it can be shown that equations (7.12) and (7.13) can support moving groups if the speed is a monotone function of the perceived signals.

In the following, we will assume that the diffusion coefficient is small enough, that is $D \approx 0$. This can happen when $\gamma_0 \ll \lambda_1^0$. To ensure that the advection coefficient still plays an important role in the movement (that is, $B \gg 0$), we assume that $\lambda_1^0 \ll \lambda_2^0$. Under these assumptions, (7.12) and (7.13) can be approximated by the

following hyperbolic equations:

$$u_t + (B\alpha^0[u]u + \gamma_0 g^0[u]u)_x = 0, \tag{7.14}$$

$$u_t + \gamma_0 (g^0[u]u)_x = 0. \tag{7.15}$$

We assume that the initial condition for these equations is a rectangular pulse of density A, and investigate the speed at which its edges are traveling. For simplicity, let us focus first on equation (7.15), and assume that its left edge is at $x = 0$. Therefore, $u(x,0) = 0$ for $x < 0$, and $u(x,0) = A$ for $x \geq 0$. Then, the speed of the left edge of the pulse is given by the Rankine-Hugoniot jump condition

$$s = \frac{\gamma_0 (g^0[A]A - g^0[0]0)}{A - 0} = \gamma_0 g^0[A]. \tag{7.16}$$

The nonlinear term $g^0[A]$ is described by

$$g^0[A] = \tanh(A \int_0^\infty K(y-x)dy - A \int_0^\infty K(x-y)dy), \ x \geq 0. \tag{7.17}$$

As before, we denote $K(s) = q_a K_a(s) - q_r K_r(s)$. Similarly, we can assume that its right edge is at $x = 0$, that is, $u(x,0) = A$ for $x \leq 0$, and $u(x,0) = 0$ for $x > 0$. The speed of this discontinuity satisfies the same equation (7.16), with the nonlinear term $g^0[A]$ described by

$$g^0[A] = \tanh(A \int_{-\infty}^0 K(y-x)dy - A \int_{-\infty}^0 K(x-y)dy), \ x \leq 0. \tag{7.18}$$

Note that, if the speeds of the right and left edges of the rectangular pulse have opposite sign, the pulse will contract or expand. If the speeds have similar sign, the pulse will undergo a translation, and hence, the group will move.

In a similar manner, the jump condition for equation (7.14) is given by

$$s = B\alpha^0[A] + \gamma_0 g^0[A]. \tag{7.19}$$

The nonlinear term $g^0[A]$ is described by equations (7.17) or (7.18), whereas $\alpha^0[A]$ is described by

$$\begin{aligned} \alpha^0[A] = & -\tanh(-A \int_0^\infty K(y-x)dy + A \int_0^\infty K(x-y)dy - y_0) + \\ & \tanh(A \int_0^\infty K(y-x)dy - A \int_0^\infty K(x-y)dy - y_0), \ x \geq 0, \end{aligned} \tag{7.20}$$

if the left edge of the pulse is at $x = 0$, or by

$$\begin{aligned}\alpha^0[A] &= -\tanh(-A\int_{-\infty}^{0} K(y-x)dy + A\int_{-\infty}^{0} K(x-y)dy - y_0) + \\ &\quad \tanh(A\int_{-\infty}^{0} K(y-x)dy - A\int_{-\infty}^{0} K(x-y)dy - y_0),\ x \geq 0, \quad (7.21)\end{aligned}$$

if the right edge of the pulse is at $x = 0$.

Comparing the shape of $g^0[u]$ and $\alpha^0[u]$ (Figure 7.2), we observe that the magnitudes of attractive and repulsive interactions (which appear in $K(s)$) lead to qualitatively similar effects on the movement direction of the jump discontinuity (i.e., the sign of the speed is the same). However, the quantitative effect (i.e., the magnitude of the speed) is slightly different because of the different magnitues for $g^0[u]$ and $\alpha^0[u]$.

Returning to the parameter scaling, recall that in Chapter 3, we observed that if we chose a different scaling for the directed and the random turning rates, we obtain an elliptic equation. A similar result is obtained when we consider density dependent speed. More precisely, for $\epsilon \to 0$, the scaling $\lambda_1 = \frac{\lambda_1^0}{\epsilon}$ and $\lambda_2 = \frac{\lambda_2^0}{\epsilon^2}$ leads to exactly the same elliptic equation

$$u_{xx} = \frac{1}{\gamma_0}(u\alpha^0[u])_x. \quad (7.22)$$

We assumed here that individuals turn more often in response to external stimuli (λ_2), than they turn randomly (λ_1). Similarly, we can distinguish between a "base-line" speed γ, and a speed due to social interactions $\bar{\gamma}g[u]$ (as in [42]):

$$\Gamma^{\pm} = \gamma \pm \bar{\gamma}g[u], \quad \text{with } \bar{\gamma} \leq \gamma. \quad (7.23)$$

Assuming that the speed resulting from social interactions ($\bar{\gamma} = \frac{\bar{\gamma}_0}{\epsilon^2}$), increases faster than the "base-line" speed ($\gamma = \frac{\gamma_0}{\epsilon\sqrt{\epsilon}}$), we obtain the following elliptic equation:

$$u_{xx} = \frac{2\lambda_1^0\bar{\gamma}_0}{\gamma_0^2}(g^0[u]u)_x. \quad (7.24)$$

Previous results [53] show that using different time scales, $\theta = t\epsilon$ and $\theta = t\epsilon^2$, leads to elliptic and parabolic equations, respectively. We showed here that using

different scales for the directed and the random turning rates, or the directed and the "base-line" speed, leads to a similar case of parabolic versus elliptic equations.

7.4 Linear stability analysis

In this section, we begin exploring the effects of the social interactions on the emergence of the group patterns. For models $M1_I$ and $M1_{II}$, the spatially homogeneous steady states $(u^+, u^-) = (u^*, u^{**})$ satisfy the same steady-state equation as model M1 (see equations (4.1)-(4.2)). As shown in Figure 4.1, there are two critical values for alignment, namely Q^* and Q^{**}, which determine the number of possible steady states. More precisely, depending on the magnitude of the alignment (q_{al}), the spatially homogeneous steady states can be one of the following pairs: (u_1^*, u_5^*), (u_2^*, u_4^*), (u_3^*, u_3^*), (u_4^*, u_2^*), and (u_5^*, u_1^*). Perturbations of these steady states with terms of the form $e^{\sigma t + ikx}$ lead to the following dispersion relations corresponding to models $M1_I$ and $M1_{II}$, respectively:

$$\begin{aligned}\sigma^2_{M1_I} \quad + \quad & \sigma_{M1_I}\left(L_1 + L_2 + \gamma ik\hat{K}A - M_5 q_{al}(\hat{K}^-_{al} + \hat{K}^+_{al})\right) + \gamma^2 k^2 - \\ & \gamma^2 k^2 \hat{K}(u^{**} - u^*) + \gamma ik(L_2 - L_1) + \gamma ikM_5 q_{al}(\hat{K}^-_{al} - \hat{K}^+_{al}) + \\ & \gamma ik\hat{K}A(L_1 + L_2) - \gamma ikM_5 A q_{al}\hat{K}(\hat{K}^+_{al} + \hat{K}^-_{al}), \end{aligned} \tag{7.25}$$

$$\begin{aligned}\sigma^2_{M1_{II}} \quad + \quad & \sigma_{M1_{II}}\left(L_1 + L_2 + \gamma ik\hat{K}A - M_5 q_{al}(\hat{K}^-_{al} + \hat{K}^+_{al})\right) + \gamma^2 k^2 - \\ & \gamma^2 k^2 b\hat{K}(u^{**} - u^*) + \gamma ik(L_2 - L_1) + \gamma ikM_5 q_{al}(\hat{K}^-_{al} - \hat{K}^+_{al}) + \\ & \gamma ik\hat{K}A(L_1 + L_2) - \gamma ikM_5 A q_{al}\hat{K}(\hat{K}^+_{al} + \hat{K}^-_{al}) + \\ & 2\gamma ikM_5\hat{K}. \end{aligned} \tag{7.26}$$

Note that the only difference between equations (7.25) and (7.26) is the extra term $2\gamma ikM_5\hat{K}$ (i.e., the last term in equation (7.26)). We will investigate shortly the effect of this term on the emergence of unstable modes. Here $\hat{K} = q_a\hat{K}_a - q_r\hat{K}_r$, where $\hat{K}_j, j = r, a$ are the Fourier transforms of the interaction kernels (2.9). The rest of the constants are given by equations (4.12)-(4.13)). Recall that the constant

y_0 has been introduced in Chapter 2 to ensure that for $q_a = q_r = q_{al} = 0$, the turning rates are mainly random.

Figure 7.3 shows examples of the dispersion relation for models $M1_I$ and $M1_{II}$, when we perturb the spatially homogeneous steady state $(u^*, u^{**}) = (u_3^*, u_3^*)$. When we perturb any of the other four steady states u_1^*, u_2^*, u_4^*, or u_5^*, the graphs of the dispersion relations look similar to the ones described in Chapter 4, Figure 4.2. For this reason, we will not discuss them here. In Figure 7.3, the continuous curve represents the real part of the dispersion relations (7.25) and (7.26), while the dashed curve represents the imaginary part. Cases (a)-(d) correspond to model $M1_I$, while cases (a')-(d') correspond to model $M1_{II}$. Cases (a) and (d) show the dispersion relation when attraction (q_a) is large. In this case, the critical wave number is $k = k_1$. Cases (b) and (c) show the dispersion relation when repulsion (q_r) is large. The critical wave number that emerges is $k = k_j$, for some $j \gg 1$ (shown is $k = k_{14}$ and $k = k_{31}$). In particular, case (c) corresponds to the situation when repulsion is larger than attraction, while the turning rates are relatively small. Recall that in Chapter 4, we have seen that when the speed is constant, spatial perturbations of the steady state u_3^* lead only to real bifurcations (as in Figure 7.3 (a), (b), (a') and (b')). However, for the density-dependent speed, perturbations of u_3^* can lead also to imaginary bifurcations, as shown in Figure 7.3 (c), (d), (c') and (d'). Therefore, depending on the parameter values, it is possible to have Hopf bifurcations (that is, $Re(\sigma(k_c)) = 0, Im(\sigma(k_c)) \neq 0$).

Comparing the graphs of these two dispersion relations for different parameter values (that is, cases (a)-(d) versus cases (a')-(d')), we conclude that the extra term which appears in equation (7.26) (and does not appear in equation (7.25)), does not have a considerable influence on the emerging wave number k, or on the amplitude of the leading eigenmode. Therefore, the linear behavior of the system (7.1) is not influenced significantly by the presence of attractive and repulsive interactions in the turning rates. In Section 7.5, we will analyze numerically the effect of these social interactions on the nonlinear behavior of the system.

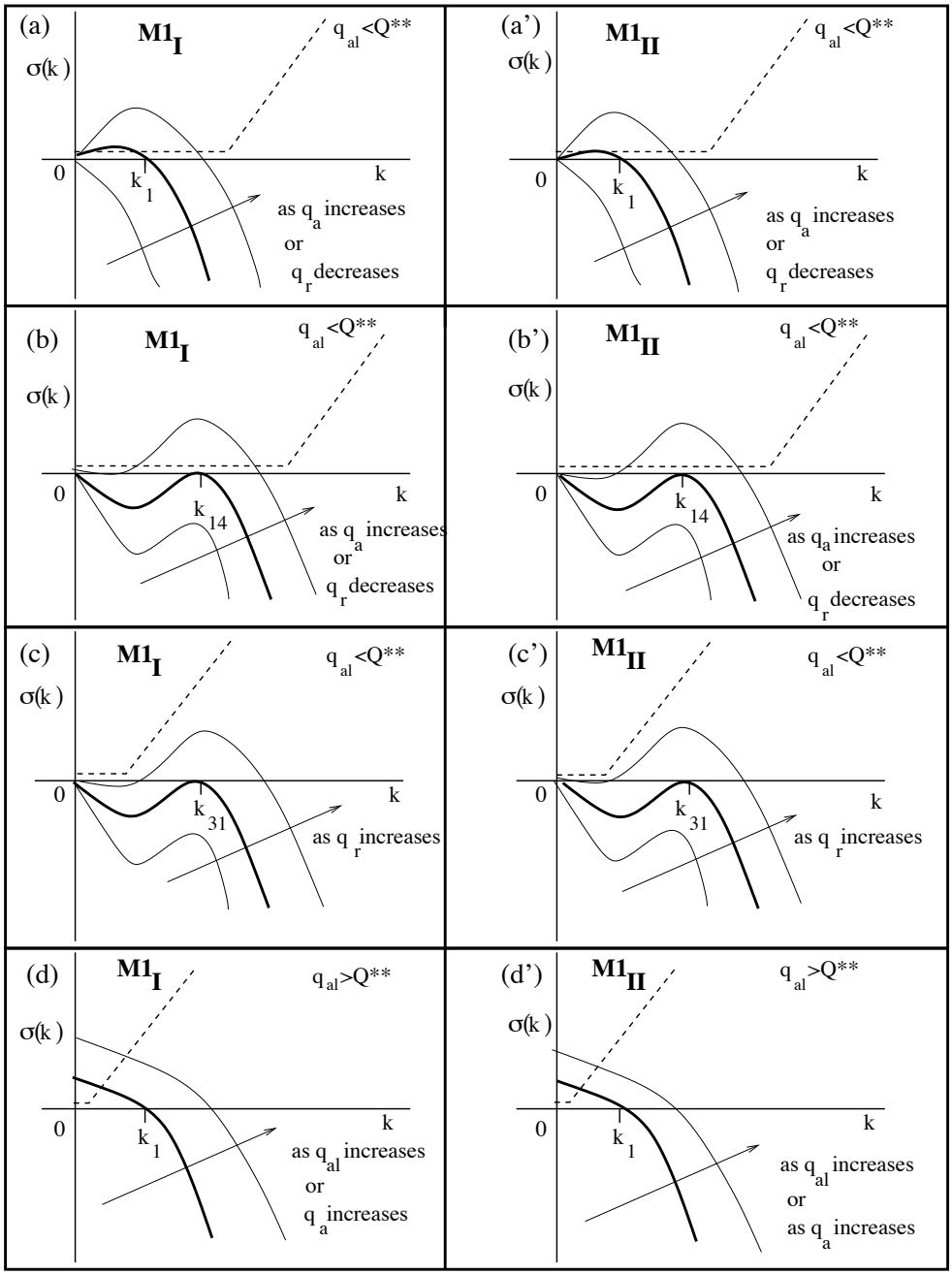

Figure 7.3: Examples of dispersion relations $\sigma(k)$ for system 7.1, when we perturb the steady state $(u^*, u^{**}) = (u_3^*, u_3^*)$. Cases (a)-(d) correspond to model $M1_I$, while cases (a')-(d') correspond to model $M1_{II}$. The solid curve represents $Re(\sigma(k))$, while the dashed curve represents $Im(\sigma(k))$. For cases (a), (b), (a') and (b'), the imaginary part of the dispersion relation is zero at the critical wave number, whereas for cases (c), (c'), (d), and (d') it is always nonzero. The parameters are as follows (for both $M1_I$ and $M1_{II}$): (a) $q_r = 0.1$, $q_a = 0.2$, $q_{al} = 0$, $\lambda_1 = 0.4$, $\lambda_2 = 1.8$; (b) $q_r = 0.05$, $q_a = 0.05$, $q_{al} = 2.0$, $\lambda_1 = 2.0$, $\lambda_2 = 9.0$; (c) $q_r = 0.1$, $q_a = 0.05$, $q_{al} = 0.0$, $\lambda_1 = 0.25$, $\lambda_2 = 1.125$; (d) $q_r = 0.05$, $q_a = 0.2$, $q_{al} = 3.5$, $\lambda_1 = 0.4$, $\lambda_2 = 1.8$.;

If we focus on the effect of the social interactions on the bifurcation of solutions from the spatially homogeneous steady state (u_3^*, u_3^*), we observe that when $Im(\sigma(k)) = 0$, increasing repulsion suppresses the emergence of heterogeneous patterns (see Figure 7.3 (a) and (b)). This effect is similar to the one observed for constant speed (see Chapter 4, for the discussion about model M1). However, when $Im(\sigma) \neq 0$, increasing repulsion leads to the emergence of modes with very large wave numbers (see Figure 7.3 (c)). Therefore, large repulsion causes individuals to speed up and/or slow down, which in turn leads to a large number of small groups. Large attraction leads to either a small number of large groups (as in Figure 7.3 (a)), or to a very large number of small groups (as in Figure 7.3 (b)).

7.5 Numerical results

In the following, we will investigate numerically some of the spatial and spatiotemporal patterns displayed by the hyperbolic model (7.1). We recall that the semi-linear system (2.1) could not exhibit shocks when the initial data was continuous. For this reason, the numerical methods used in Chapters 5 and 6 were appropriate. System (7.1), on the other hand, can exhibit shocks for continuous initial conditions. Moreover, the nonlinear flux terms can cause numerical instabilities. This requires the use of high-resolution numerical schemes. In particular, to obtain a stable, second order accurate method, we will use a time-splitting approach which deals with the advection term and the source term separately (see for example, [63],[66]). More precisely, for the source term we will use a fourth order Runge-Kutta method. For the advection term we will use a second order, non-oscillatory, central difference scheme introduced by Nessyahu and Tadmor [86]. The advantage of this numerical scheme is that, unlike the Godunov-type methods, it is not necessary to solve Riemann problems, which can be a very expensive task.

In Section 7.5.1, we describe in detail the numerical method we use to discretize system (7.1). In Section 7.5.2, we investigate some of the patterns displayed by this

hyperbolic model. In particular, we use these numerical results to understand the effect of attractive and repulsive speeds on the resulting group structures. Also, we will investigate the effect of attractive and repulsive turning rates on the nonlinear behavior of system (7.1). For this, recall that in Section 7.4 we showed that the linear behavior of models $M1_I$ and $M1_{\mathbf{II}}$ is qualitatively similar. In Section 7.5.2 we will investigate if a similar result holds when we consider the effect of nonlinear terms.

7.5.1 Numerical method

To discretize model (7.1), we use a time-splitting approach. More precisely, let us rewrite system (7.1) as

$$\mathbf{u}_t + (F(\mathbf{u}))_x = s(\mathbf{u}), \tag{7.27}$$

where we define $\mathbf{u} = (u^+, u^-)^T$, the flux term $F(\mathbf{u})$=$(F_1(\mathbf{u}), F_2(\mathbf{u}))$=$(\Gamma^+[u^+, u^-]u^+$, $-\Gamma^-[u^+, u^-]u^-)$, and the source term $s(\mathbf{u})$=$(-u^+\lambda^+[u^+, u^-]+u^-\lambda^-[u^+, u^-], u^+\lambda^+[u^+, u^-]-$ $u^-\lambda^-[u^+, u^-])^T$. To compute the solution of system (7.1), we deal with the source term and the advection term separately. First, we focus on the source term, and solve the following ordinary differential equation:

$$\mathbf{u}_t = s(\mathbf{u}). \tag{7.28}$$

Let $S_{x,t}$ be the solution operator of this equation. Hence, the solution of this problem can be written as $\bar{\mathbf{u}}(x,t) = S_{x,t}\bar{\mathbf{u}}(x,0)$. We then use this solution as the initial condition for the advection term

$$\mathbf{u}_t = (F(\mathbf{u}))_x. \tag{7.29}$$

Similarly, let $A_{x,t}$ be the solution operator of this advection equation. Therefore, the final solution of the hyperbolic system (7.27) can be written as

$$\mathbf{u}(x,t) = A_{x,t}S_{x,t}\mathbf{u}(x,0). \tag{7.30}$$

To use this approach in a numerical method, we replace the solution operators $S_{x,t}$ and $A_{x,t}$ with the numerical schemes $\bar{S}_{x,k}$ and $\bar{A}_{x,k}$ which solve equations (7.28) and

(7.29) over time steps of length $\Delta t = k$ [66]. Therefore, the numerical solution of (7.1) at the next time step ($\mathbf{U}^{n+1}$) is given by

$$\mathbf{U}^{n+1} = \bar{A}_{x,k}\bar{S}_{x,k}U^n. \tag{7.31}$$

To implement this method, we discretize the space-time plane choosing a space step $\Delta x = h$, and a time step $\Delta t = k$. Also, we define the discrete mesh points $(x_j, t_n) = (jh, nk)$, with $j = 0..N-1$ (where $N-1 = L/h$ is the number of mesh points), and $n \in \mathbf{N}$. To solve equation (7.28), we use a classical fourth order Runge-Kutta method. As mentioned in Chapter 5, the nonlocal terms are first approximated with finite integrals on $[0, L]$, and then these integrals are calculated using Simpson's method. Moreover, as in Chapter 5, the numerical solutions of equation (7.28), $u1_j^n$ and $u2_j^n$, are seen as approximations of $u^+(x,t)$ and $u^-(x,t)$ over the cells $[x_{j-1/2}, x_{j+1/2}]$ (see equations (5.2)).

To solve the advection equation, we use a high-resolution method introduced by Nessyahu and Tadmor (the NT scheme) [86]. This scheme is based on a staggered form of a Lax-Friedrichs scheme. Therefore, in this case the solutions are seen as approximations over the cells $[x_j, x_{j+1}]$:

$$u1_{j+1/2}^n = \frac{1}{h}\int_{x_j}^{x_{j+1}} u^+(x,t_n)dx, \quad u2_{j+1/2}^n = \frac{1}{h}\int_{x_j}^{x_{j+1}} u^-(x,t_n)dx. \tag{7.32}$$

Let us define the vector $v_j^n = (u1_j^n, u2_j^n)$. The numerical scheme is described by the following equation:

$$\begin{aligned} v_j^{n+1/2} &= v_j^n - \frac{k}{2}(F_j^n)', \\ v_{j+1/2}^{n+1} &= \frac{1}{2}(v_j^n + v_{j+1}^n) + \frac{h}{8}\left((v_j^n)' - (v_{j+1}^n)'\right) - \frac{k}{h}\left(F(v_{j+1}^{n+1/2}) - F(v_j^{n+1/2})\right). \end{aligned} \tag{7.33}$$

Here $(F_j^n)' = \left((F1_j^n)', (F2_j^n)'\right)^T$ approximates the derivative of the flux $(F(\mathbf{u}))_x$=$((F_1(\mathbf{u}))_x$, $(F_1(\mathbf{u}))_x)$, while $(v_j^n)'$=$\left((u1_j^n)', (u2_j^n)'\right)^T$ approximates the slopes $\mathbf{u}_x$=$(u_x^+, u_x^-)^T$. To calculate these derivatives, we use the so-called min-mod limiter:

$$\begin{aligned} (v_j^n)' &= \text{minmod}(\frac{v_j^n - v_{j-1}^n}{h}, \frac{v_{j+1}^n - v_j^n}{h}), \\ (F_j^n)' &= \text{minmod}(\frac{F_j^n - F_{j-1}^n}{h}, \frac{F_{j+1}^n - F_j^n}{h}), \end{aligned} \tag{7.34}$$

where

$$\text{minmod}(a,b) = \frac{1}{2}\left(\text{sgn}(a) + \text{sgn}(b)\right)\min(|a|,|b|). \tag{7.35}$$

Componentwise, equations (7.34) can be written as

$$\begin{aligned}
(u1_j^n)' &= \text{minmod}(\frac{u1_j^n - u1_{j-1}^n}{h}, \frac{u1_{j+1}^n - u1_j^n}{h}),\\
(u2_j^n)' &= \text{minmod}(\frac{u2_j^n - u2_{j-1}^n}{h}, \frac{u2_{j+1}^n - u2_j^n}{h}),
\end{aligned} \tag{7.36}$$

and

$$\begin{aligned}
(F1_j^n)' &= \text{minmod}(\frac{F1_j^n - F1_{j-1}^n}{h}, \frac{F1_{j+1}^n - F1_j^n}{h}),\\
(F2_j^n)' &= \text{minmod}(\frac{F2_j^n - F2_{j-1}^n}{h}, \frac{F2_{j+1}^n - F2_j^n}{h}).
\end{aligned} \tag{7.37}$$

Alternatively, we can use the more accurate UNO (Uniformly Non-Oscillatory) limiter [86]:

$$\begin{aligned}
(v_j^n)' &= \text{minmod}\left(\frac{v_j^n - v_{j-1}^n}{h} + \frac{1}{2h}\text{minmod}(v_j - 2v_{j-1} + v_{j-2}, v_{j+1} - 2v_j + v_{j-1})\right.,\\
&\qquad \left.\frac{v_{j+1}^n - v_j^n}{h} - \frac{1}{2h}\text{minmod}(v_{j+1} - 2v_j + v_{j-1}, v_{j+2} - 2v_{j+1} + v_j)\right),\\
(F_j^n)' &= \text{minmod}\left(\frac{F_j^n - F_{j-1}^n}{h} + \frac{1}{2h}\text{minmod}(F_j - 2F_{j-1} + F_{j-2}, F_{j+1} - 2F_j + F_{j-1})\right.,\\
&\qquad \left.\frac{F_{j+1}^n - F_j^n}{h} - \frac{1}{2h}\text{minmod}(F_{j+1} - 2F_j + F_{j-1}, F_{j+2} - 2F_{j+1} + F_j)\right).
\end{aligned} \tag{7.38}$$

Recall that the Runge-Kutta scheme used to discretize equation (7.28), computes the solution at (x_j, t_n), $j = 0..N-1$. Since the numerical scheme (7.33) computes the solution at an intermediate point $(x_{j+1/2}, t_n)$, we have to apply it twice to obtain the value of the solution at (x_j, t_n).

To complete the description of the numerical scheme, we have to specify the boundary conditions. In particular, we will use periodic boundary conditions to be able to compare the patterns obtained when the speed is density-dependent, with the patterns obtained in Chapter 5, when the speed was constant. Note that because of the staggered NT scheme (7.33), we have to pay attention to the implementation of these boundary conditions. In particular, after applying the scheme twice, we obtain the solution at points (x_{j+1}, t_n), $j = 0..N-1$. To make sure that the boundary

conditions are applied at the end points of the interval $[0, L]$ (that is, at (x_0, t_n) and (x_{N-1}, t_n)), we have to translate the solution one space-step back. This way, the solution will be calculated at (x_j, t_n), $j = 0..N-1$, and we can implement the periodic boundary conditions.

Throughout the simulations we will use the space step $h = 0.01$, and the time step $k = 0.018$. Note that this time step is enough to ensure that there is no numerical instability. Moreover, in this section we will focus only on the spatially homogeneous steady state (u_3^*, u_3^*), and choose the initial conditions to be random perturbations of this state. The following parameters will be fixed during the simulations: the domain length ($L = 10$), the length of the interaction ranges for the repulsion ($s_r = 0.25$), alignment ($s_{al} = 0.5$), and attraction terms ($s_a = 1.0$), the width of the interaction kernels $m_j = s_j/8$ ($j = r, al, a$), and the constant component of the speed ($\gamma = 0.1$).

At the beginning of this section, we mentioned that we first solve the source equation (7.28), and then use the solution to solve the advection equation (7.29). However, it should be specified that it does not matter which of the two equations is solved first. We have performed simulations where we first solved the advection equation, and then solved the source equation. The results were qualitatively similar. Also, qualitatively similar results were obtained when using either the min-mod limiter (7.34), or the UNO limiter (7.38).

7.5.2 Spatial and spatiotemporal patterns

Before starting the investigation of the spatial and spatiotemporal patterns displayed by system (7.1), we should stress that the parameter space for this system is very large, and a thorough analysis of all possible patterns is not a trivial task. However, our purpose here is not to identify all these patterns, but to investigate the effect of density-dependent speed on the resulting group patterns. Also, we are interested in the behavior of the groups when considering turning rates that depend only on the alignment interactions, versus turning rates that depend on all three

social interactions. For this reason, we will investigate only the following arbitrary parameter subspaces: (1) $q_{al} = 0$, $q_r = 0.1$, and $q_a \in [0.1, 0.9]$; (2) $q_{al} = 2$, $q_r = 0.1$, and $q_a \in [0.1, 0.9]$; (3) $q_{al} = 0$, $q_r \in [0.1, 0.7]$, and $q_a = 0.1$; (4) $q_{al} = 3.5$, $q_r = 0.05$, and $q_a \in [0.1, 0.7]$. Note that for cases (1)-(3), the alignment parameter is such that $q_{al} < Q^{**}$. This corresponds to the dispersion relations shown in Figure 7.3 (a)-(c) and (a')-(c'). In case (4), the alignment parameter satisfies $q_{al} > Q^{**}$. This corresponds to the dispersion relation shown in Figure 7.3 (d)-(d').

Figures 7.4 and 7.5 describe some of the patterns displayed by system (7.1). It should be specified that all these patterns can be obtained with either model $M1_I$ or model $M1_{II}$. Moreover, the parameter ranges for which these patterns are obtained, are quite similar.

Figure 7.4 (a) shows the patterns displayed by system (7.1) for large values of attraction, and in the absence of alignment. In this case, the groups are stationary, with individuals evenly spread over the entire group. As we further increase the attraction, the speeding-up/slowing-down behavior leads to the formation of a large number of small, high-density groups. The pattern is shown in Figure 7.4 (b). This pattern is also specific to the case when repulsion is much larger than attraction. Note that both patterns are similar to patterns obtained for constant speed (see Figures 5.5(1), and (2)).

For small to intermediate values of attraction, the speeding-up/slowing-down behavior leads to the formation of very high density subgroups. These subgroups can form larger stationary groups (as shown in Figure 7.4 (c)), or can form traveling groups that split and merge again (as shown in Figure 7.4 (d)). Note that this splitting and merging behavior is consistent with the results of some Lagrangian models that consider density-dependent speed and direction changes [42].

In Section 7.4 we observed that for large repulsion, it is possible to obtain moving groups, at least for small time and infinitesimal perturbations (see Figure 7.3 (c)). Figures 7.4 (e) and (f) show two patterns that are obtained when the dispersion relation is similar to the one shown in Figure 7.3 (c). Case (e) describes an irregular

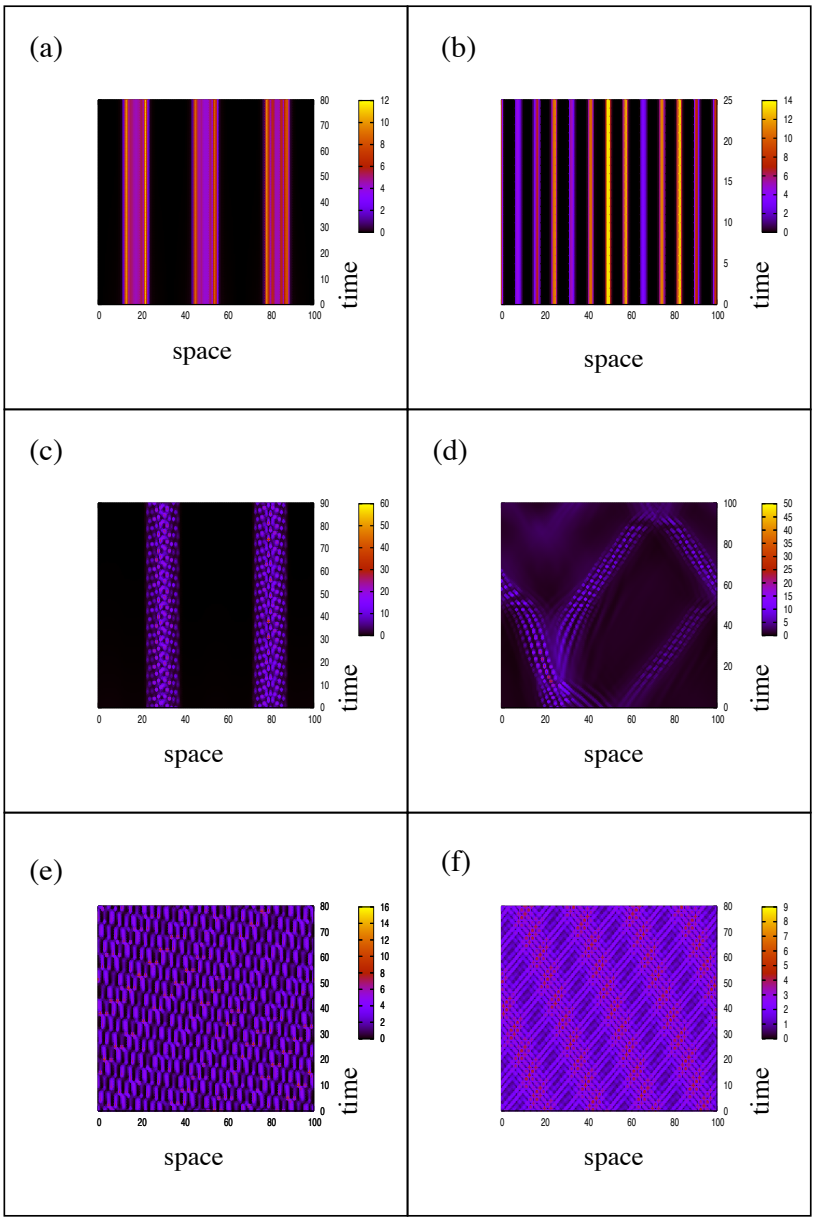

Figure 7.4: Examples of patterns displayed by system (7.1). The parameters are: (a) $q_r = 0.1$, $q_a = 0.5$, $q_{al} = 0$; (b) $q_r = 0.1$, $q_a = 0.7$, $q_{al} = 2$; (c) $q_r = 0.1$, $q_a = 0.3$, $q_{al} = 2$; (d) $q_r = 0.05$, $q_a = 0.2$, $q_{al} = 3.5$; (e) $q_r = 0.5$, $q_a = 0.1$, $q_{al} = 0$; (f) $q_r = 0.1$, $q_a = 0.1$, $q_{al} = 0$. The turning rates are $\lambda_1 = 0.2$ and $\lambda_2 = 0.9$. The simulations are run for time up to $t = 150$. The plots show the last 25 to 100 time steps.

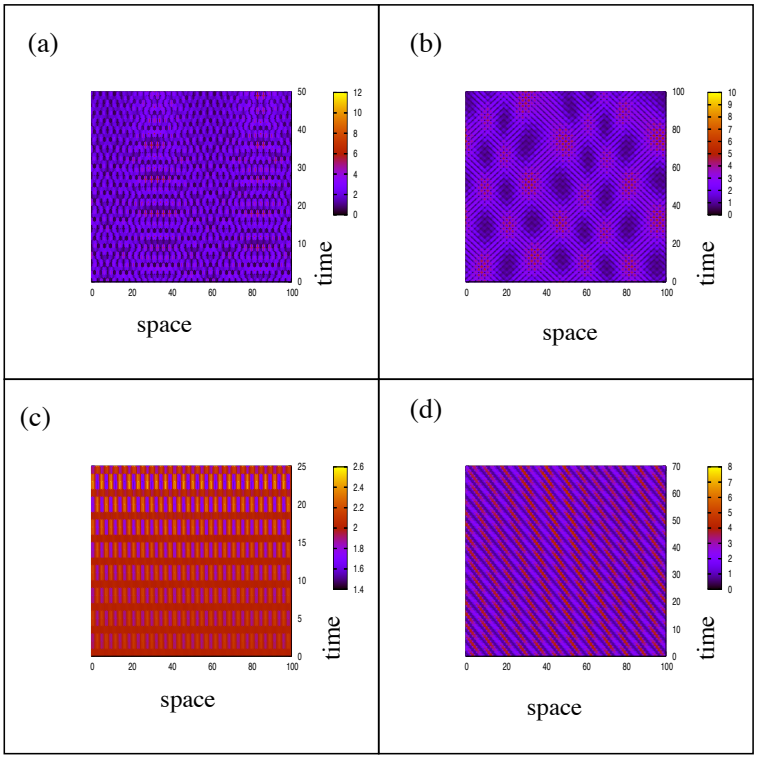

Figure 7.5: Examples of transient patterns displayed by system (7.1). The parameters are: (a) $q_r = 0.1$, $q_a = 0.3$, $q_{al} = 0$, $\lambda_1 = 0.2$, $\lambda_2 = 0.9$;(time $t < 50$) (b) $q_r = 0.1$, $q_a = 0.2$, $q_{al} = 0$, $\lambda_1 = 0.2$, $\lambda_2 = 0.9$;(time $t < 100$) (c) $q_r = 0.05$, $q_a = 0.2$, $q_{al} = 3.5$, $\lambda_1 = 0.4$, $\lambda_2 = 1.8$, $M1_I, u_3^*$;time $t \leq 60$; (d) $q_r = 0.05$, $q_a = 0.2$, $q_{al} = 3.5$, $\lambda_1 = 0.4$, $\lambda_2 = 1.8$; time $62 \leq t \leq 80$. The plots show the last 35-70 time steps.

pattern obtained when repulsion is larger than attraction. Note that if the repulsion is much larger than attraction, then the final pattern is described by Figure 7.4(b). Case (f) describes a periodic pattern obtained when attraction and repulsion have similar magnitudes. This pattern arises when very high density left-moving and right-moving subgroups pass through each other.

Note that the patterns described in Figure 7.4 do not change their structure at least up to time $t = 200$. It is possible that for very large time they will evolve into different patterns. However, this aspect was not investigated here.

Moreover, studying the evolution of solutions up to time $t = 200$, we observed that system (7.1) displays also transient patterns. Four of these are shown in Figure

7.5. For example, the initial pattern obtained when attraction is larger than repulsion, is similar to the one shown in Figure 7.5(a). For larger time, this pattern evolves into the pattern shown in Figure 7.4(c). Figure 7.5(b) shows left-moving and right-moving high-density subgroups of individuals that pass through each other. Note that compared to the pattern displayed in Figure 7.5(f), which shows more individuals moving in one direction than in the other, here there is approximately the same number of individuals moving left or right. Because of this, even if the groups move, the pattern as a whole is stationary. Recall that similar behavior was obtained for the communication mechanism M5, when we assumed constant speed. However, in that case the groups were larger, with individuals uniformly spread over the entire group. As time increases (in particular for $t > 100$), pattern (b) evolves into the pattern shown in Figure 7.4(c). Figure 7.5(c) shows a type of pattern obtained for initial time, when alignment is very large. As time progresses, this pattern evolves into the traveling train shown in Figure 7.5(d). Note that compared to the traveling train discussed in Chapter 5 (Figure 5.5(6)), which was periodic only in space, here the pattern is periodic in both time and space. For very large time, this pattern evolves into the splitting and merging behavior shown in Figure 7.4(d).

7.6 Discussion

In this chapter, we introduced a new model which assumes that both the speed and the turning rates depend on the social interactions. To simplify the analysis, we focused only on the reception mechanisms introduced in Chapter 2, Section 2.2 (model M1). Since individuals can respond to signals received from neighbors within the attraction and repulsion ranges by changing direction, as well as speeding up or slowing down, we focused on two cases. More specifically, model $M1_I$ assumes that the speed depends on the attractive and repulsive interactions, while the turning rates depend only on the alignment interactions. Model $M1_{II}$ assumes that both the speed and the turning rates depend on the attractive and repulsive interactions.

In addition, the turning depends also on the alignment interactions.

Throughout this chapter, we compared these two models using analytical and numerical results. In particular, formal parabolic limit suggests that for large speed and large turning rates, there are no significant differences between the models with density-dependent speeds or density-dependent turning rates. The limiting parabolic equations are qualitatively similar. Moreover, when the speed is density-dependent, turning in response to attractive and repulsive interactions, or turning randomly, has similar effects.

Linear stability analysis of model (7.1) shows that for small time and infinitesimal perturbations, the effect of turning in response only to alignment interactions versus turning in response to all three social interactions, is insignificant. This suggests that the speed is more sensitive to these interactions than are the turning rates. Therefore, the behavior is mainly influenced by the speed, unless both the attraction and alignment are very large. This result is also supported by the numerical simulations. The patterns discussed in Section 7.5 were obtained for both models $M1_I$ and $M1_{II}$.

Comparing the patterns obtained for density-dependent speed, with the patterns obtained for constant speed (see Chapter 5), we note that the attractive and repulsive speed leads to groups formed of very high density subgroups. In particular, if alignment is strong (i.e., $q_{al} > Q^{**}$), then variations in the speed can cause these groups to split and merge again. It should be mentioned that this behavior can also be obtained for $q_{al} < Q^{**}$, when we perturb the spatially homogeneous steady state (u_1^*, u_5^*). Note that this steady state implicitly assumes a certain degree of group polarization. A similar splitting/merging behavior was previously obtained with a Lagrangian model that incorporates density-dependent speed and density-dependent turning rates [42]. However, the Eulerian models existent in the literature focus only on pattern coarsening (see for example [35, 123]). This can explain the merging of animal groups, but not the splitting. We show here that nonlocal attractive and repulsive speeds, combined with nonlocal turning rates, can explain both behaviors.

Numerical results also show that in case of density-dependent speed, it is possible to obtain moving groups even in the absence of alignment. This behavior could not be observed for constant speed. Moreover, these moving groups become stationary if attraction is very large.

In Chapter 5, we observed that the rippling behavior was possible only when considering a particular communication mechanism (M5). We should stress that the assumptions made for this communication mechanism were consistent with the assumptions of other models existent in the literature (see [59, 71] and the discussion in Chapter 8). The numerical results presented in this chapter show that it is possible to obtain a similar rippling behavior if we assume that individuals respond to their neighbors by changing their movement direction, as well as speeding up or slowing down. These results suggest that taking into consideration different communication mechanisms, as well as density-dependent speed and turning rates, can give an explanation for the multitude of spatial and spatiotemporal patterns observed in nature. However we still do not have a clear answer regarding which patterns are generated by density-dependent speed alone, by density-dependent turning rates alone, and which are generated by a combination of speed and turning rates. This requires a thorough analysis of the parameter space, which is beyond the scope of this research. Nevertheless, this is the first continuum model with density-dependent speed that displays such a wide variety of patterns. Also, it is the first continuum model which discusses the spliting/merging behavior of animal groups, and not just the coarsening of the patterns.

Chapter 8

Discussion

In this thesis we developed a general framework for modeling animal group formation and movement based on how animals receive information from their conspecifics and the amount of information received. This framework presents a straightforward way to incorporate different social interactions, and communication mechanisms.

Starting with the same modeling procedure as Pfistner [99] (that is, a hyperbolic model with nonlocal turning rates), we considered three social interactions that affect the turning behavior of an individual: attraction towards individuals that are far away, repulsion from those that are nearby, and alignment with those neighbors that are at intermediate distances. Moreover, to account for the different ways animals receive information about their neighbors' position and direction of movement, we incorporated different communication mechanisms (sub-models M1-M5). Note that the mechanisms presented in this thesis are not the only possible ones. Starting with different assumptions about the communication signals, one can derive a multitude of new mechanisms. Therefore, this modeling framework can be tailored to specific animal species that use particular signal reception mechanisms.

Using this framework, we demonstrated the importance of adapting speed and direction of movement, to the emergence of different types of group behaviors and the corresponding group structures that can be found in nature. Moreover, we showed that this framework can explain the different patterns obtained by *all* other parabolic and hyperbolic models for group formation, that exist in the mathematical literature.

Therefore, the model introduced in this thesis presents a unitary approach for animal group formation and movement: all these different patterns can be understood as being caused by different communication mechanisms. In support of this idea, we mention the parabolic [59, 60] and hyperbolic models [71] that investigate the rippling behavior in Myxobacteria colonies. Note that all these models consider interactions of individuals with neighbors moving in opposite direction. This is consistent with the reception mechanism we considered in sub-model M5. Moreover, all these models show rippling patterns similar to the one presented in Figure 5.5. Also, we should mention that for the hyperbolic models, it does not matter the shape of the turning rate functions (compare [71] and [30]). The only important thing seems to be the movement direction of the neighbors. This result allows us to postulate that other group patterns (if not all) might be the result of different mechanisms involved in signal reception.

In addition to this, we should stress that our modeling framework can be used to obtain a variety of new and interesting spatial and spatiotemporal group patterns. Some of these patterns (such as the splitting-merging behavior) were previously obtained only with Lagrangian models. However, the majority of the patterns described here are novel.

Moreover, the modeling procedure introduced in this thesis suggests that the use of different communication signals can play an important role in the fluid patterns observed in some animal groups. In particular, the switch between different communication signals, sometimes as a result of environmental factors, can lead to the transitions between different patterns observed in animal groups.

In the following two sections we will summarize the results presented in this thesis. In Sections 8.1 we will focus on the mathematical results, while in Section 8.2 we will summarize the biological results. In particular, we will draw a parallel between our results and some empirical observations. In Section 8.3, we will present some open problems and discuss future work.

8.1 Discussion of mathematical results

In this thesis we derived a new semi-linear hyperbolic model with nonlocal turning rates. First, we focused on the case when the speeds are constant. In an attempt to bridge the gap between the Lagrangian and Eulerian approaches, we showed how can we derive this model using a correlated random walk approach.

In regard to this hyperbolic model, we first showed the existence of solutions on infinite as well as finite domains with periodic boundary conditions. Note that in the mathematical literature there are existence results for local hyperbolic models. However, our nonlocal model requires a more careful discussion of the turning rates. Then, we have taken a formal parabolic limit to reduce this hyperbolic model to a well known parabolic model for animal group formation. The results showed that for large speeds and large turning rates, two biological approaches namely attractive and repulsive turning rates, and attractive and repulsive speeds, lead to similar results.

The complexity of this new model can be easily seen in the multitude of the spatial and spatiotemporal patterns displayed by it. Previous parabolic and hyperbolic models for animal group formation and movement usually displayed 1-2 patterns. Only two of the two-dimensional parabolic models displayed 4 different patterns (see [15, 77]). However, our nonlocal hyperbolic model (with its five sub-models) can display at least 13 different patterns. Moreover, these results are obtained with a one-dimensional model. To understand some of these patterns, we used bifurcation and perturbation theory. In particular, the nonlinear behavior of the system was investigated near bifurcation points using weakly nonlinear analysis. The analysis shows the existence of subcritical bifurcations to large amplitude heterogeneous patterns.

To understand the effect of the variations in the animals' speed due to attractive and repulsive interactions, we then introduced a new quasi-linear hyperbolic model. A formal parabolic limit shows that for large speeds and turning rates, the results

are similar to those obtained for constant speed. More precisely, when the speeds and large turning rates are very large, it does not really matter if the attractive and repulsive interactions influence the speed, the turning rates, or both. In all cases the results are qualitatively similar. In terms of spatial and spatiotemporal patterns, this quasi-linear model is even more complex than the previous model with constant speed. More precisely, numerical investigations of only one of the communication mechanisms described in Chapter 2 (i.e., the mechanism corresponding to model M1) showed at least 10 different patterns.

In summary, these results show that analytical methods such as bifurcation and perturbation analysis, or weakly-nonlinear analysis, can be used to investigate different biological questions regarding the structure of animal aggregations.

8.2 Parallel between analytical and empirical results

In this section, we discuss how the complex patterns that emerge in the hyperbolic model introduced in this thesis, relate to the empirical observations. In particular, the emphasis will be on the biological mechanisms that can explain the different group structures observed in animal aggregations.

We begin the discussion on the mechanisms that cause different group structures, by analyzing the shape of the aggregations. In Chapter 5, we saw that groups are well defined, that is, the density outside the group is essentially zero. Moreover, our results show an increased density at the leading edge of the moving groups, due to leading individuals turning around to return to the group under the influence of attraction forces. These results seem to agree with empirical studies [19, 125]. Uvarov [125], observes that "a noticeable feature of a band marching in frontal formation is the greater density of hoppers at its leading edge", a possible explanation for this being that "the leading hoppers may hesitate because there are no other hoppers in their anterior field of vision and they may even return to the front after jumping beyond it; the hoppers behind are, therefore likely to catch up with the

moving front causing a concentration" (vol. II, pp. 164).

Focusing now on the types of spatial patterns displayed by our model, we observe that traveling pulses and stationary pulses correspond to moving (e.g., traveling schools of fish, flocks of birds) and stationary (e.g., resting) groups of animals. Breathers might be associated to the anti-predatory behavior observed in some schools of fish [36] or flocks of birds [72], when the groups expand and then contract. Uvarov [125] offers an illustrating example of oscillations (i.e., traveling trains) exhibited by animal groups. Commenting on the inter-individual interactions of locust hoppers, Uvarov describes how "a jump by a disturbed hopper leads to an outburst by others; this spreads through the group or band, and eventually subsides in a way reminiscent of ripples on the surface of water caused by a pebble"(vol. II, pp. 165). Other examples of oscillations can be observed in some bird flocks [16] or fish schools [105]. Moreover, at the beginning of this chapter we mentioned the rippling behavior observed in Myxobacteria colonies. Note that this behavior is a transient behavior during the aggregation process that leads to the formation of fruiting bodies. Our numerical results show similar transient rippling behavior that leads to stationary groups.

Zigzag movement is seen in flocks of birds [16, 26, 56] that rapidly change direction, making sharp turns of 180^0 [26]. Potts [104] observed that birds do not turn simultaneously, but the maneuver is initiated by birds banking towards the flock, and not by those that turn away from the flock. The movement then propagates like a wave throughout the flock. On the other hand, Davis [26] suggested that some birds may signal their intention to change direction, and when a certain number of birds make the same decision, the entire flock turns.

The empirical results also differentiate between two types of group structure during the turning behavior. Studying the turning behavior in Rock Dove flocks, Pomeroy and Heppner [103] noticed that the flock became more compact just before turning, and then it expanded. They also pointed out that this type of turning is different from what is observed in fish, where groups are usually compact, and they

expand as they make a turn. Moreover, the authors suggested that this difference may be explained by the inter-individual distances that are smaller in fish schools, compared to those in bird flocks. Partridge et. al. [98] discussed the relationship between the inter-individual distance in fish schools, and the fish body structure which causes the maneuverability of individuals. They noticed that the fish that are more maneuverable (such as cod and saithe) have smaller inter-individual distances, whereas a "stiff-bodied" fish (such as herring) has larger inter-individual distances.

As we have seen in Chapter 5, our mathematical model shows the same two types of group structure during the turning behavior. The mechanisms that determine these types of group structure are the different individual turning rates exhibited by animals. Consequently, the model suggests that it might be possible to explain the two types of group structure in terms of individual turning behavior. However, these results show that there is need for a more in-depth analysis that correlates the compactness of the observed aggregations with the individual turning rates.

Another pattern that can be connected to the observed group behaviors is the splitting and merging of the groups. In particular, numerical simulations show that the splitting and emerging pattern can be obtained just by assuming that individuals turn around, speed up or slow down in response to the behavior of close or distant neighbors. These splitting and merging behaviors are usually discussed in the presence of predators (see [56, 72, 90, 126]) However, there are examples of animal groups that split and merge again even in the absence of predators [36]. We show here that this behavior can be explained through a combination of density-dependent speeds and turning rates.Indirectly, the speed can be related to the anti-predatory behavior.

The results presented in this section were all obtained using numerical methods. However, analytical results too can provide valuable biological information. For example, the subcritical bifurcation obtained through weakly nonlinear analysis suggests that there is a threshold group density. Groups with densities below this threshold will disperse, while groups with densities above this threshold will

become even more dense and persist for a longer time. This transition between the disordered behavior and the ordered behavior represented by the high-density stationary or moving groups, is important for the understanding of the formation and movement of animal groups. For example, Buhl et. al. [17] have shown experimentally and numerically that as the density of locusts in a group increases, there is a transition from disordered movement to collective motion of aligned groups. Understanding such transitions has potential applications to understanding and controlling the outbreaks of different insect pests, such as locusts.

While the biological patterns we described here are complex two- and three-dimensional phenomena, the simulation results show that our one-dimensional model nonetheless captures essential features of these patterns. This one-dimensional model can approximate the behavior of animal groups in higher dimensions if they move in a domain which is much longer than wide.

Because of the complexity of the animal aggregations, it has been difficult to quantify the different types of groups and animal movements. One step forward was made in [17], where the results of an individual based model were compared with laboratory experiments. The results we presented in this thesis invite further observations and experimental investigations involving the manipulation of communication in animal groups.

8.3 Future work

The hyperbolic model we introduced in this thesis is extremely rich. To investigate it, we used numerical and analytical results such as bifurcation theory and perturbation theory. However, there are so many more problems regarding this new model that are worth investigating. In the following we present some of these issues.

- In Chapter 2, we derived the nonlocal hyperbolic model from a correlated random walk. It would be interesting to investigate if the results obtained with the random walk model match the patterns displayed by the continuum

model (2.1).

- In Chapter 4, we have seen that if the domain L is sufficiently large, u_2^* and u_4^* are always unstable. Moreover, the numerics show that perturbations of the steady states u_2^* and u_4^* go to the same attractor as the perturbations of u_1^*, u_3^*, and u_5^*. Therefore, to better understand this hyperbolic system, it would be helpful to find this attractor, at least for some particular parameter spaces. Such existence results were obtained for local hyperbolic systems [52]. For example, following similar steps as in [12], Hillen [52] constructed a Liapunov function via a variational approach, and use it to find the global attractor of a reaction random walk system. However, the application of this method to our system is greatly complicated by the nonlocal terms. Moreover, the attractor will depend on all model parameters.

- The spatial and spatiotemporal patterns displayed by this hyperbolic model are very rich and, most of them, novel. Therefore, it will be interesting to derive analytical techniques to investigate these patterns (for example, the feathers, the breathers, or the zigzag patterns). However, the nonlocal terms complicate the analysis. It should be mentioned that even the classical patterns, such as traveling pulses, are difficult to investigate because of these nonlocal terms. For example, a traveling pulse ansatz (i.e., $u^{\pm}(z) = U^{\pm}(x - ct)$, $U^{\pm}(\pm\infty) = 0$) transforms the hyperbolic system (2.1) into a integro-differential equation with respect to the variable z:

$$u(z)_z = C_1(c)u(z) + C_2(c)u(z)(C_3(c)f(y^+[u(z)]) - f(y^-[u(z)])), \qquad (8.1)$$

  where C_1, C_2, and C_3 are constants that depend on the speed c, and $y^{\pm}[u(z)]$ are the nonlocal terms described in Chapter 2. The difficulty of solving this equation resides in the fact that the derivative, as well as the nonlocal terms, are taken with respect to the same variable z.

- In terms of pattern formation, it would be interesting to compare the pat-

terns displayed by the limiting parabolic equation (3.30), with the patterns displayed by the hyperbolic system (2.1). In particular, it will be interesting to investigate the effect of different communication mechanisms on the parabolic equation (3.30).

- From a biological point of view, it would be helpful to extend the model to two spatial dimensions. This way, we can compare the theoretical results with empirical results. The local interactions will be described by a double integral: over space, and over a turning angle. However, this makes more difficult to discriminate between different communication mechanisms.

Bibliography

[1] M. Adioui, J. P. Treuil, and O. Arino. Alignment in a fish school: a mixed lagrangian-eulerian approach. *Ecol. Moldel.*, 167:19–32, 2003.

[2] A. C. Alberts. Constraints on the design of chemical communication systems in terrestrial vertebrates. *The American Naturalist*, 139:S62–S89, 1992.

[3] W. Alt. Degenerate diffusion equations with drigt functionals modeling aggregation. *Nonlinear Analysis*, 9:811–836, 1985.

[4] C. Anderson, G Theraulaz, and J.-L. Deneubourg. Self-assemblages in insect societies. *Insectes Soc.*, 49:99–110, 2002.

[5] I. Aoki. A simulation study on the schooling mechanism in fish. *Bull. Japan Soc. Sci. Fish*, 48:1081–1088, 1982.

[6] Ch. Becco, N. Vanderwalle, J. Delcourt, and P. Poncin. Experimental evidence of a structural and dynamical transition in fish school. *Physica A*, 367:487–493, 2006.

[7] J. A. Beecham and K. D. Farnsworth. Animal group forces resulting from predator avoidance and competition minimization. *J. Theor. Biol.*, 198:533–548, 1999.

[8] M. Beekman, D. J. T. Sumpter, and F. L. W. Ratnieks. Phase transitions between disordered and ordered foraging in pharaoh's ants. *Proc. Natl. Acad. Sci.*, 98(17):9703–9706, 2001.

[9] M. Bekele and G. Ananthakrishna. High-order amplitude equations for steps on the creep curve. *Phys. Rev. E*, 56(6):6917–6928, 1997.

[10] M. Bodnar and J. J. L. Velasquez. Derivation of macroscopic equations for individual cell-based models: a formal approach. *Math. Meth. Appl. Sci.*, 28:1757–1779, 2005.

[11] U. Börner, A. Deutsch, and M. Bär. A generalized discrete model linking rippling pattern formation and individual cell reversal statistics in colonies of myxobacteria. *Phys. Biol.*, 3:138–146, 2006.

[12] R. K. Brayton and W. L. Miranker. A stability theory for nonlinear mixed initial boundary value problem. *Arch. Rat. Mech. Anal.*, 17:358–376, 1964.

[13] C. M. Breder. Equations descriptive of fish schools and other animal aggregations. *Ecology*, 35:361–370, 1954.

[14] A. Bressan. *Hyperbolic systems of conservation laws. The one-dimensional Cauchy problem*. Oxford University Press, 2000.

[15] P. C. Bressloff. Euclidean shift-twist symmetry in population models of self-aligning objects. *SIAM J. Appl. Math.*, 64:1668–1690, 2004.

[16] J. B. Buchanan, C. T. Schick, L. A. Brennan, and S. G. Herman. Merlin predation on wintering dunlins: Hunting success and dunlin escape tactics. *Wilson Bull.*, 100:108–118, 1988.

[17] J. Buhl, D. J. T. Sumpter, I. D. Couzin, J. J. Hale, E. Despland, E. R. Miller, and S. J. Simpson. From disorder to order in marching locusts. *Science*, 312:1402–1406, 2006.

[18] H. R. Bullis. Observations on the feeding behavior of white-tip sharks on schooling fishes. *Ecology*, 42:194–195, 1961.

[19] D. Bumann and J. Krause. Front individuals lead in shoals of three-spined sticklebacks (*Gasterosteus aculeatus*) and juvenile roach (*Rutilus rutilus*). *Behaviour*, 125:189–198, 1993.

[20] M. Burger, V. Capasso, and D. Morale. On an aggregation model with long and short range interactions. *Nonlinear Analysis: Real World Applications*, 8:939–958, 2007.

[21] D. Chowdhury, K. Nishinary, and A. Schadschneider. Self-organized patterns and traffic flowin colonies of organisms: from bacteria and social insects to vertebrates. *Phase Transitions*, 77(5):601–624, 2004.

[22] L. Conradt and T. J. Roper. Consensus decision making in animals. *TRENDS Ecol. Evol.*, 20(8):449–456, 2005.

[23] I. D. Couzin and J. Krause. Self-organization and collective behavior of vertebrates. *Adv. Study Behav.*, 32:1–67, 2003.

[24] I. D. Couzin, J. Krause, R. James, G.D. Ruxton, and N. R. Franks. Collective memory and spatial sorting in animal groups. *J. Theor. Biol.*, 218:1–11, 2002.

[25] M. C. Cross and P. C. Hohenberg. Pattern formation outside equilibrium. *Rev. Mod. Phys.*, 65(3):851–1112, 1993.

[26] M. Davis. The coordinated aerobatics of dunlin flocks. *Anim. Behav.*, 28:668–673, 1980.

[27] L. Edelstein-Keshet, J. Watmough, and D. Grünbaum. Do travelling band solutions describe cohesive swarms? an investigation for migratory locusts. *J. Math. Biol.*, 36(6):515–549, 1998.

[28] L. Edelstein-Keshet, J. Watmough, and D. Grunbaum. Do travelling band solutions describe cohesive swarms? an investigations for migratory locusts. *J. Math. Biol.*, 36:515–549, 1998.

[29] R. Eftimie, G. de Vries, and M. A. Lewis. Complex spatial group patterns result from different animal communication mechanisms. *Proc. Natl. Acad. Sci.*, 104(17):6974–6979, 2007.

[30] R. Eftimie, G. de Vries, M. A. Lewis, and F. Lutscher. Modeling group formation and activity patterns in self-organizing collectives of individuals. *Bull. Math. Biol.*, 69(5):1537–1566, 2007.

[31] J. A. Endler. Signals, signal conditions, and the direction of evolution. *Am. Nat.*, 139:S125–S153, 1992.

[32] J. A. Endler. Some general comments on the evolution of animal communication systems. *Phil. Trans. R. Soc. Lond. B*, 340:215–225, 1993.

[33] J. A. Endler and A. L. Basolo. Sensory ecology, receiver biases and sexual selection. *TREE*, 13(10):415–420, 1998.

[34] E. Fernández-Juricic, J. T. Erichsen, and A. Kacelnik. Visual perception and social foraging in birds. *TRENDS Ecol. Evol.*, 19(1):25–31, 2004.

[35] G. Flierl, D. Grünbaum, S. Levin, and D. Olson. From individuals to aggregations: the interplay between behavior and physics. *J. Theor. Biol.*, 196:397–454, 1999.

[36] P. Freon, F. Gerlotto, and M. Soria. Changes in school structure according to external stimuli: description and influence on acoustic assessment. *Fisheries Research*, 15:45–46, 1992.

[37] V. Gazi and K. M. Passino. Stability analysis of swarms. In *Proc. American Control Conf.*, pages 8–10, Anchorage,AK, 2002.

[38] S. Goldstein. On diffusion by discontinuous movements and the telegraph equation. *Quart. J. Mech. Appl.Math.*, 4:129–156, 1951.

[39] D. Grünbaum. Translating stochastic density dependent individual behaviours with sensory constraints to an eulerian model of animal swarming. *J. Math. Biol.*, 33:139–161, 1994.

[40] D. Grünbaum. Schooling as a strategy for taxis in a noisy environment. *Evol. Ecol.*, 12:503–522, 1998.

[41] D. Grünbaum and A. Okubo. Modelling social animal aggregations. In S. A. Levin, editor, *Frontiers in mathematical biology, Lecture notes in biomathematics 100*, pages 296–325. Springer-Verlag, Berlin Heidelberg, 1994.

[42] S. Gueron, S. A. Levin, and D. I. Rubenstein. The dynamics of herds: from individuals to aggregations. *J. Theor. Biol.*, 182:85–98, 1996.

[43] K. Hadeler. Reaction telegraph equations and random walk systems. In S. Verduyn Lunel S. van Strien, editor, *Stochastic and spatial structures of dynamical systems*, pages 133–161. Royal Acad. of the Nederlands. North Holland,Amsterdam, 1996.

[44] K. Hadeler. *Mathematics inspired by biology. Lecture Notes in Mathematics*, chapter Reaction transport systems in biological modelling, pages 95–150. Springer Verlag, 1999.

[45] W. D. Hamilton. Geometry for the selfish herd. *J. Theor. Biol.*, 31:295–311, 1971.

[46] D. Helbing and P. Molnar. Social force model for pedestrian dynamics. *Phys. Rev. E*, 51(5):4282–4286, 1995.

[47] D. Helbing and M. Treiber. Numerical simulations of macroscopic traffic equations. *Comput. Sci. Eng.*, 1(5):89–98, 1999.

[48] G.S. Helfman. Fish behaviour by day, night and twilight. In T.J. Pitcher, editor, *Behaviour of teleost fishes*, pages 479–512. Chapman & Hall, 1993.

[49] C. K. Hemelrijk and H. Hildenbrandt. Self-organized shape and frontal density of fish schools. *Ethology*, 114:245–254, 2008.

[50] C. K. Hemelrijk and H. Kunz. Density distribution and size sorting in fish schools: an individual-based model. *Behav. Ecol.*, 16(1):178–187, 2004.

[51] E. Hensor, I. D. Couzin, R. James, and J. Krause. Modelling density-dependent fish shoal distributions in the laboratory. *Oikos*, 110:344–352, 2005.

[52] T. Hillen. Qualitative analysis of hyperbolic random walk systems. Technical report, SFB 382, Report No. 43, 1996.

[53] T. Hillen and H. G. Othmer. The diffusion limit of transport equations derived from velocity jump process. *SIAM J.Appl.Math.*, 61:751–775, 2000.

[54] T. Hillen, C. Rhode, and F. Lutscher. Existence of weak solutions for a hyperbolic model for chemosensitive movement. *J. Math. Anal. Appl.*, 260:173–199, 2001.

[55] T. Hillen and A. Stevens. Hyperbolic models for chemotaxis in 1-D. *Nonlinear Analysis: Real World Applications*, 1:409–433, 2000.

[56] D. A. Humphries and P. M. Driver. Protean defence by prey animals. *Oecologia(Berl.)*, 5:285–302, 1970.

[57] J. R. Hunter. Communication of velocity changes in jack mackerel (*Trachurus Symmetricus*) schools. *Anim. Behav.*, 17:507–514, 1969.

[58] A. Huth and C. Wissel. The simulation of fish schools in comparison with experimental data. *Ecol. Model.*, 75/76:135–145, 1994.

[59] O. Igoshin, A. Mogilner, R. Welch, D. Kaiser, and G. Oster. Pattern formation and traveling waves in myxobacteria: Theory and modeling. *Proc. Natl. Acad. Sci. USA*, 98:14913–14918, 2001.

[60] O. A. Igoshin, R. Welch, D. Kaiser, and G. Oster. Waves and aggregation patterns in myxobacteria. *Proc. Natl. Acad. Sci. USA*, 101:4256–4261, 2004.

[61] Y. Inada. Steering mechanisms of fish schools. *Complexity International*, 8:1–9, 2001.

[62] M. Kac. A stochastic model related to the telegrapher's equation. *Rocky Mountain J. Math.*, 4:497–509, 1974.

[63] K. H. Karlsen, K. Brusdal, H.K. Dahle, S. Evje, and K.-A. Lie. The corrected operator splitting approach applied to a nonlinear advection-diffusion problem. *Comput. Methods Appl. Mech. Eng.*, 167:239, 1998.

[64] H. Kunz and C. K. Hemelrijk. Artificial fish schools: collective effects of school size, body size, and body form. *Artificial Life*, 9:237–253, 2003.

[65] C. Kuttler. *Freie Randwertprobleme für eindimensionale Transportgleichungen*. PhD thesis, University of Tübingen, 2000.

[66] R. LeVeque. *Numerical Methods for Conservation Laws*. Birkhäuser, Basel, 1992.

[67] M. A. Lewis. Spatial coupling of plant and herbivore dynamics: The contribution of herbivore dispersal to transient and persistent "waves" of damage. *Theor. Popul. Biol.*, 45:277–312, 1994.

[68] M. A. Lewis and J. D. Murray. Analysis of dynamic and stationary pattern formation in the cell cortex. *J. Math. Biol.*, 31:25–71, 1992.

[69] F. Lutscher. Modeling alignment and movement of animals and cells. *J. Math. Biol.*, 45:234–260, 2002.

[70] F. Lutscher. A model for speed adaptation of individuals and existence of weak solutions. *Euro. Jnl. of Applied Mathematics*, 14:291–311, 2003.

[71] F. Lutscher and A. Stevens. Emerging patterns in a hyperbolic model for locally interacting cell systems. *J. Nonlinear Sci.*, 12:619–640, 2002.

[72] P. F. Major and L. M. Dill. The three-dimensional structure of airborne bird flocks. *Behav. Ecol. Sociobiol.*, 4:111–122, 1978.

[73] P. Marler. Animal communication signals. *Science*, 157:769–774, 1967.

[74] B. J. Matkowski. Nonlinear dynamic stability. *S.I.A.M. J. Appl.Math.*, 18:872–883, 1970.

[75] M. Mimura and M. Yamaguti. Pattern formation in interacting and diffusing systems in population biology. *Advances in Biophysics*, 15:19–65, 1982.

[76] A. Mogilner and L. Edelstein-Keshet. Selecting a common direction. i. how orientational order can arise from simple contact responses between interacting cells. *J. Math. Biol.*, 33:619–660, 1995.

[77] A. Mogilner and L. Edelstein-Keshet. Spatio-angular order in populations of self-aligning objects: formation of oriented patches. *Physica D*, 89:346–367, 1996.

[78] A. Mogilner and L. Edelstein-Keshet. Spatio-temporal order in populations of self-aligning objects: formation of oriented patches. *Physica D*, 89:346–367, 1996.

[79] A. Mogilner and L. Edelstein-Keshet. A non-local model for a swarm. *J. Math. Biol.*, 38:534–570, 1999.

[80] A. Mogilner and L. Edelstein-Keshet. A non-local model for a swarm. *J. Math. Biol.*, 38:534–570, 1999.

[81] A. Mogilner, L. Edelstein-Keshet, L. Bent, and A. Spiros. Mutual interactions, potentials, and individual distance in a social aggregation. *J. Math. Biol.*, 47:353–389, 2003.

[82] A. Mogilner, L. Edelstein-Keshet, and G. B. Ermentrout. Selecting a common direction. ii. peak-like solutions representing total alignment of cell clusters. *J. Math. Biol.*, 34:811–842, 1996.

[83] D. Morale, V. Capasso, and K. Oelschläger. An interacting particle system modeling aggregation behavior: from individuals to populations. *J. Math. Biol.*, 50:49–66, 2005.

[84] J. D. Murray. *Asymptotic Analysis*. Springer-Verlag, 1984.

[85] J. D. Murray. *Mathematical Biology*. Springer, 1989.

[86] H. Nessyahu and E. Tadmor. Non-oscillatory central differencing for hyperbolic conservation laws. *J. comput. phys.*, 87:408–463, 1990.

[87] A. C. Newell, T. Passot, and J. Lega. Order parameter equations for patterns. *Annu. Rev. Fluid. Mech.*, 25:399–453, 1993.

[88] G. A. Ngwa and P. K. Maini. Spatio-temporal patterns in a mechanical model for mesenchimal morphogenesis. *J. Math. Biol.*, 33:489–520, 1995.

[89] H. S. Niwa. Self-organizing dynamical model of fish schooling. *J. Theor. Biol.*, 171:123–136, 1994.

[90] L. Nottestad and B. E. Axelsen. Herring schooling manoeuvres in response to killer whale attacks. *Can. J. Zool.*, 77:1540–1546, 1999.

[91] A. Okubo. *Diffusion and Ecological Problems, Mathematical Models*. Springer Verlag,NY, 1980.

[92] A. Okubo. Dynamical aspects of animal grouping: swarms, school, flocks and herds. In M. Kotani, editor, *Adv. Biophys.*, volume 22, pages 1–94, 1986.

[93] J. K. Parrish. Using behavior and ecology to exploit schooling fishes. *Environ. Biol. Fish.*, 55:157–181, 1999.

[94] J. K. Parrish and L. E. Keshet. Complexity, pattern, and evolutionary trade-offs in animal aggregation. *Science*, 284:99–101, 1999.

[95] J. K. Parrish and S. V. Viscido. Traffic rules of fish schools: a review of agent-based approaches. In C. K. Hemelrijk, editor, *Self-organisation and evolution of social systems*. Cambridge University Press, 2005.

[96] J. K. Parrish, S. V. Viscido, and D. Grunbaum. Self-organized fish schools: An examination of emergent properties. *Bioll. Bull.*, 202:296–305, 2002.

[97] S. R. Partan and P. Marler. Issues in the classification of multimodal communication signals. *Am. Nat.*, 166:231–245, 2005.

[98] B. L. Partridge, T. Pitcher, J. M. Cullen, and J. Wilson. The three-dimensional structure of fish schools. *Behav. Ecol. Sociobiol.*, 6:277–288, 1980.

[99] B. Pfistner. A one dimensional model for the swarming behavior of Myxobakteria. In W. Alt and G. Hoffmann, editors, *Biological Motion, Lecture Notes on Biomathematics, 89*, pages 556–563. Springer, 1990.

[100] B. Pfistner. Simulation of the dynamics of myxobacteria swarms based on a one-dimensional interaction model. *J. Biol. Systems*, 3:579–588, 1995.

[101] B. Pfistner and W. Alt. A two dimensional random walk model for swarming behavior. In W. Alt and G. Hoffmann, editors, *Biological Motion, Lecture Notes on Biomathematics, 89*, pages 564–565. Springer, 1990.

[102] T. J. Pitcher, A. E. Magurran, and I. J. Winfield. Fish in larger shoals fing food faster. *Behav. Ecol. Sociobiol.*, 10:149–151, 1982.

[103] H. Pomeroy and F. Heppner. Structure of turning in airborne rock dove (*Columba Livia*) flocks. *The Auk*, 109:256–267, 1992.

[104] W. K. Potts. The chorus-line hypothesis of manoeuvre coordination in avian flocks. *Nature*, 309:344–345, 1984.

[105] D. V. Radakov. *Schooling in the ecology of fish*. John Willey & Sons Inc, New York, 1973.

[106] R. Redheffer. *Differential equations. Theory and applications*. Jones & Bartlett Publishers, 1991.

[107] H. Reuter and B. Breckling. Self organization of fish schools: an object-oriented model. *Ecol. Model.*, 75/76:147–159, 1994.

[108] C. W. Reynolds. Flocks, herds and schools: A distributed behavioral model. *Computer Graphics*, 21:25–34, 1987.

[109] T. Robbins. Seed dispersal and biological invasion: A mathematical analysis. PhD thesis, University of Utah, 2003.

[110] J. C. Robinson. *Infinite-Dimensional Dynamical Systems*. Cambridge University Press, 2001.

[111] J. G. Robinson. *Primate communication*, chapter Vocal systems regulating within-group spacing, pages 94–116. Cambridge University Press, 1982.

[112] A. Schadschneider. Traffic flow: a statistical point of view. *Physica A*, 313:153–187, 2002.

[113] K. Schmidt-Nielsen. *Animal Physiolog: Adaptation and Environment*. Cambridge University Press, 1990.

[114] S. J. Simpson, A. R. McCaffery, and B. F. Hägele. A behavioural analysis of phase change in the desert locust. *Biol. Rev.*, 74:461–480, 1999.

[115] S. J. Simpson, G. A. Sword, P. D. Lorch, and I. D. Couzin. Cannibal crickets on a forced march for protein and salt. *Proc. Natl. Acad. Sci. USA*, 103:4152–4156, 2006.

[116] S. Springer. Some observations of the behavior of schools of fishes in the gulf of mexico and adjacent waters. *Ecology*, 38:166–171, 1966.

[117] L. E. Stephenson and D. J. Wollkind. Weakly nonlinear stability analyses of one-dimensional turing pattern formation in activator-inhibitor/immobilizer model systems. *J. Math. Biology*, 33:771–815, 1995.

[118] J. Strickwerda. *Finite difference schemes and partial differential equations*. Chapman & Hall, New York, 1989.

[119] J. T. Stuart. On the nonlinear mechanism of wave disturbances in stable and unstable parallel flows. part i. *J. Fluid Mech.*, 9:353–370, 1960.

[120] D. J. T. Sumpter. The principles of collective animal behaviour. *Phil. Trans. R. Soc. B*, 361:5–22, 2006.

[121] G. Theraulaz, J. Gautrais, S. Camazine, and J.-L. Deneubourg. The formation of spatial patterns in social insects: from simple behaviors to complex structures. *Phil. Trans. R. Soc. Lond.*, 361:1263–1282, 2003.

[122] C. M. Topaz and A. L. Bertozzi. Swarming patterns in a two-dimensional kinematic model for biological groups. *SIAM J. Appl. Math.*, 65:152–174, 2004.

[123] C. M. Topaz, A. L. Bertozzi, and M. A. Lewis. A nonlocal continuum model for biological aggregation. *Bull. Math. Bio.*, 68:1601–1623, 2006.

[124] Turchin. *Quantitative analysis of movement: measuring and modeling population redistribution in animals and plants*. Sinauer Associates, Inc. Publishers, 1998.

[125] B. Uvarov. *Grasshoppers and locusts*. Centre for Overseas Pest Research, London, 1966.

[126] R. Vabø and L. Nøttestad. An individual based model of fish school reactions: predicting antipredator behaviour as observed in nature. *Fish. Oceanogr.*, 6:155–171, 1997.

[127] J. C. van Olst and J. R. Hunter. Some aspectsof the organization of fish schools. *J. Fish. Res.*, 27:1125–1238, 1970.

[128] T. Vicsek, A. Czirók, E. Ben-Jacob, I. Cohen, and O. Shochet. Novel type of phase transition in a system of self-driven particles. *Phys. Rev. Lett.*, 75(6):1226–1229, 1995.

[129] T. Vicsek, A. Czirok, I. J. Farkas, and D. Helbing. Application of statistical mechanics to collective motion in biology. *Physica A*, 274:182–189, 1999.

[130] S. V. Viscido. The case for the selfish herd hypothesis. *Comments on theoretical biology*, 8:665–684, 2003.

[131] S. V. Viscido, J. K. Parish, and D. Grunbaum. Individual behavior and emergent properties of fish schools. *Mar. Ecol. Prog. Ser.*, 273:239–249, 2004.

[132] S. V. Viscido, J. K. Parrish, and D. Grünbaum. The effect of population size and number of influential neighbors on the emergent properties of fish schools. *Ecol. Model.*, 183:347–363, 2005.

[133] K. Warburton and J. Lazarus. Tendency-distance models of social cohesion in animal groups. *J. Theor. Biol.*, 150:473–488, 1991.

[134] S. R. Witkin. The importance of directional sound radiation in avian vocalization. *The Condor*, 79:490–493, 1977.

[135] E. Zauderer. *Partial differential equations of applied mathematics*. John Wiley and Sons Ltd., 1990.